MINERALOGY AND PROVENANCE OF THE TiO_2 – ILMENITE HEAVY MINERAL SAND DEPOSIT OF NATAKA

By

Sílvio José Elias

Dissertation submitted for the degree of Master of Science in Geology

Department of Geological Science

University of Cape Town

South Africa

2016

Supervised by Prof. Chris Harris

PLAGIARISM DECLARATION

I, **Sílvio José Elias**, know and understand the meaning of plagiarism and declare that all of the work in the dissertation is my own, and was never in an extent submitted for acquisition of any academic degree. Other workers contributions were properly cited and listed in under references.

Signature: _____

Date: _____

ACKNOWLEDGEMENTS

I am grateful to Prof. Chris Harris by his supportive character in my academic and social life. His humbly constructive criticism and tireless language correction have improved previous version of this dissertation, and are also acknowledged.

Kenmare Resources plc., Kenmare Moma Mining (Mauritus) Limited and JBSF whom allowed me to embark on this journey and funded the studies are kindly appreciated.

Mr Sonsiama Kargbo is specially thanked by appointing me to this program, and his persistent counseling and career couching. Mr Paul Leandri is acknowledged for helping define the project and Mr Benjamim Chachuaio for his prompt administrative response. Extensive gratitude is addressed to all my colleagues of the Geological Service Section whom gave their best to cover the gap, when I was attending this program.

Dr. Dirk Frei is kindly acknowledged by conducting geochronology analyses; Dr. Megan Becker and Gaynor Yorath are thanked by their support with QEMSCAN analysis and encouragement.

Warm gratitude is also addressed to Noxolo Zwane, Sherisha Roopnarain by helping me find my way in Cape Town and in academia.

TABLE OF CONTENTS

ABSTRACT

The Nataka heavy mineral sand deposit occurs along the northeast Mozambique coastline. It comprises a regional Pleistocene elliptical structure extending from Somalia, passing through Kenya, Tanzania, Madagascar and Mozambique, to Richards Bay in South Africa.

The deposit consists of fine- to medium- grained, unconsolidated red sediments, hosting heavy minerals. The deposit mineral assemblage is made up of non-valuable phases comprising mostly magnetite, hematite, chromite, monazite, and the valuable phases dominated by ilmenite (50.91 wt. %), with additional zircon and rutile (9.96 and 3.52 wt. % respectively). The total heavy minerals comprise about 5% volume, of which 2 % are valuable heavy minerals making up about 445 Mt (million tonnes) probable resources. This study focuses on the mineralogical characterization of ilmenite from the Nataka deposit, alongside with sediment provenance.

Mineralogical and chemical characterisation of ilmenite undertaken on 32 samples from 16 selected drill holes using a combination of QEMSCAN and EPMA revealed that the ilmenite has undergone different stages of alteration, at distinct environment conditions, yielding products spanning from hydrated ilmenite to leucoxene. The alteration dominantly involved groundwater, which was oxidizing and acidic, hence the predominance of ilmenite-pseudorutile alteration. Long exposure to direct sunshine has been hypothesized as a different process that might have favoured the direct alteration of ilmenite to leucoxene and of pseudorutile to leucoxene, on a smaller scale. The major impurities in the ilmenite are Al and Si, which are enriched in the advanced ilmenite alteration products (leucoxene), where they fill pores and cracks. Chromium impurities occur as discrete grains of chrome spinel.

The compositional variety of magnetite, Cr-spinel, tourmaline, zircon and rutile indicate major contribution from granitoid terranes, subjected to granulite metamorphic facies (750 to 1000 ^{0}C), and minor contribution from mafic plutonic intrusions. The granitoid field as a sediment source area if analysed in conjunction with zircon ages (1100 – 900 Ma, 900 – 700 Ma, and 650 – 500 Ma), and zircon $\delta^{18}O$ (7.07 ‰) is consistent with preferential sourcing from the proximal Mesoproterozoic Nampula Complex, with some contribution from igneous plutonic rocks from Xixano, Lalamo and Montepuez Complexes.

LIST OF FIGURES

LIST OF TABLES

LIST OF APPENDIXES

ABREVIATIONS, ACRONYMOUS AND UNITS

Listed	Meaning
amsl	Above mean sea level
ca.	Circa
CDNC	Cabo Delgado Nappe Complex
EAAO	East Africa Antarctica Orogeny
EDS	Energy dispersive spectrometry
FEG	Field emission gun
LST	Lithium heteropolytungstates
PMA	Particle mineralogical analysis
SMSW	Standard mean sea water
THM	Total heavy minerals
EMP	Electron microprobe
EMPA	Electron microprobe analyser
LA-ICP-MS	Laser ablation inductively coupled mass spectrometry
LA-SF-ICP-MS	Laser ablation sector field inductively coupled mass spectrometry
QEMSCAN	Quantitative evaluation of minerals by scanning electron microscopy
SIMS	Secondary ion mass spectrometry
SHRIMP	Sensitive high mass resolution ion microprobe
XRD	X - ray diffraction
XRF	X - ray fluorescence
µm	Micron
‰	Per mil
Å	Angstrom
kV	Kilo-Volts
mA	Mil-Amperes
nA	Nano-Amperes
ppm	Parts per million
RPM	Revolutions per minute
wt. %	Weight percent

CHAPTER 1. INTRODUCTION

Beach placers are worldwide found in sandy coastlines, formed as a result of protracted reworking by waves, of rich heavy mineral loads discharged to the beach by rivers, favoured by sea level fluctuations. During the reworking process a lag of heavy minerals is amassed due to selective transport governed by grain size and density (see Table 1 for specific gravity of common heavy minerals), as well as entrainment by large quartz and feldspars grains, that are major constituents of sediment loads, during dragging transport. Komar and Wang (1984), in their study of beaches in Oregon observed that the entrainment is effective due to the fine-grained nature of the heavy minerals enabling those grains to "hide" in between small interstices.

Essential, Beach placer deposits comprise valuable heavy minerals (VHM) concentrations of ilmenite ($FeTiO_3$), however some rutile (TiO_2), zircon ($ZrSiO_4$) and monazite ($(Ce,La,Y,Th)PO_4$) are likely to occur as accessory minerals. Other less valuable minerals such as garnet, kyanite, epidote, staurolite are common additional phases present.

In Mozambique, placer deposits occur all along the coastline making up the stratigraphic sequence of the Mozambique Basin and the Rovuma Basin (Salman & Abdula, 1995) at the south and north of the country, respectively.

The study area (Nataka) is part of the Rovuma Basin and represents one of several valuable heavy minerals accumulations, building up the regional Moma Deposit, within the Nampula Province, northeast part of the country. The Nataka deposit is under mining concession on behalf of Kenmare Resource plc. This deposit and others in the Nampula Province have been discovered over several years of geological exploration campaigns on a board scale within the country in the early 1990's, few years after the company was founded.

The natural abundance of ilmenite, high demand in TiO_2 and depletion of rutile deposits have turned ilmenite into an important raw material. However, the ilmenite market value as feed stock is determined by its TiO_2 content, which increases with alteration. During the ilmenite alteration deleterious elements such as V, Cr, Al, Si, P also increase, therefore a detailed mineralogy study is necessary.

Table 1. Specific gravities for the common heavy minerals. Left side showing valuable minerals and right less valuable minerals. Modified from Nesse (2000), and Hurlbut and Sharp (1998).

Mineral	Composition	Specific Gravity
Anatase	TiO_2	3.90
Chromite	$FeCr_2O_4$	4.60
Corundum	Al_2O_3	4.02
Ilmenite	$FeTiO_3$	3.6-4.79
Magnetite	Fe_3O_4	4.9-5.18
Monazite	$(Ce,La,Y,Th)PO_4$	4.60-5.40
Rutile	TiO_2	4.18-4.25
Spinel	$MgAl_2O_4$	3.50-4.10
Zircon	$ZrSiO_4$	4.68

Mineral	Composition	Specific Gravity
Apatite	$Ca_5(PO_4)_3(F,CL,OH)$	3.15-3.20
Augite	$(Ca,Na)(Mg,Fe,Al)(Si,Al)_2O_6$	3.20-3.40
Epidote	$Ca_2(Al,Fe)Al_2O(sio_4)(Si_2O_7)OH$	3.35-3.45
Hornblende	$(Ca,Na)_{2-3}(Mg,Fe,Al)_5Si_6(Si,Al)_2O_{22}(OH)_2$	3.00-3.40
Enstatite	$(Mg,Fe)SiO_3$	3.40-3.50
Kyanite	Al_2SiO_5	3.55-3.66
Sillimanite	Al_2SiO_5	3.23
Sphene	$CaTiO(SiO_4)$	3.4-3.55
Garnet	$(Mg,Fe, Mn, Ca)_3(Al, Fe, Cr)_2(SiO_4)_3$	3.10-4.37
Staurolite	$Fe_2Al_9O_6(sio_4)_4(O,OH)_2$	3.65-3.75

1.1. LOCATION

The Nataka deposit is located at the north of Mozambique coastline, in the Nampula Province, about 230 km from Nampula city and 2000 km from Maputo the capital city of the country (Fig.1).

The deposit is about 5 km from the Kenmare Moma mine, in a rural area, and surrounded by small villages; Topuito being the most important, as the one hosting actual mine infrastructures. The access can be made by an unsealed road connecting Nampula city, via Nametil or by air using the Kenmare airstrip.

The study area is part of a regional geomorphic dune structure, consisting of: 1) Frontal dunes; 2) Coastal and Estuarine; 3) Lowlands; and 4) High Dunes.

The Nataka area comprises two types of geomorphological features namely: the High Dune, which is a dune range with an average elevation of 100 m above mean sea level (amsl) (Lynn & Goldup, 2000:36); and the Coastal and Estuarine, making the border flood plains surrounding the whole structure (Fig. 2).

The area is under the influence of a tropical climate, with two dominant seasons, clearly differentiated by the rainfall and temperatures. The annual mean temperature is 25.5 ^{o}C and the annual rainfall is 1400 mm/yr (Coastal and Environmental Services, 2000).

The higher temperatures and high volume of precipitation occur during the rainy season that covers the period from December to April, while the dry season extends from May to November.

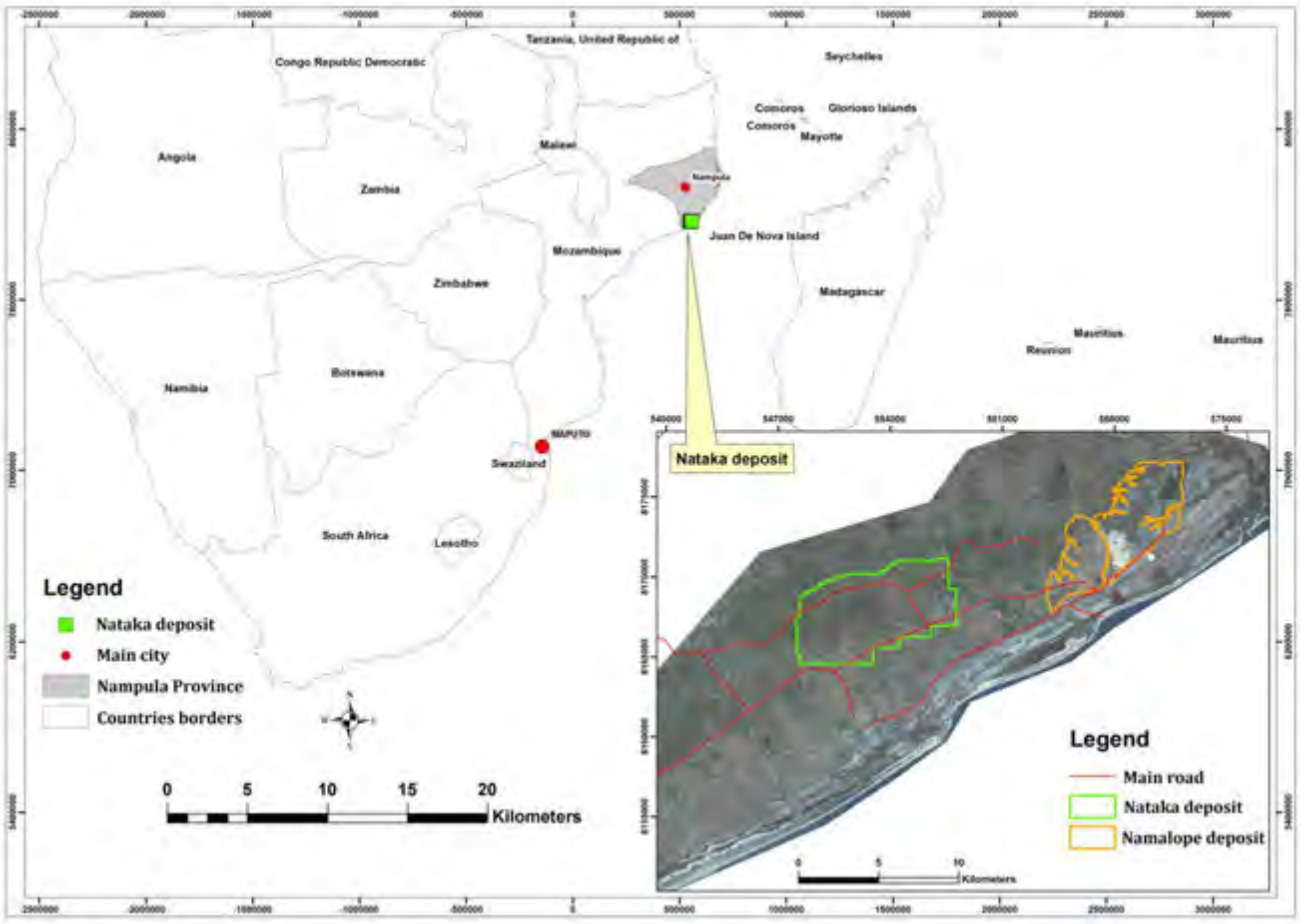

Figure 1. Map showing Nataka deposit location at the top left side of the image, and an aerial-photograph of Nataka and surrounding areas at the bottom right edge.

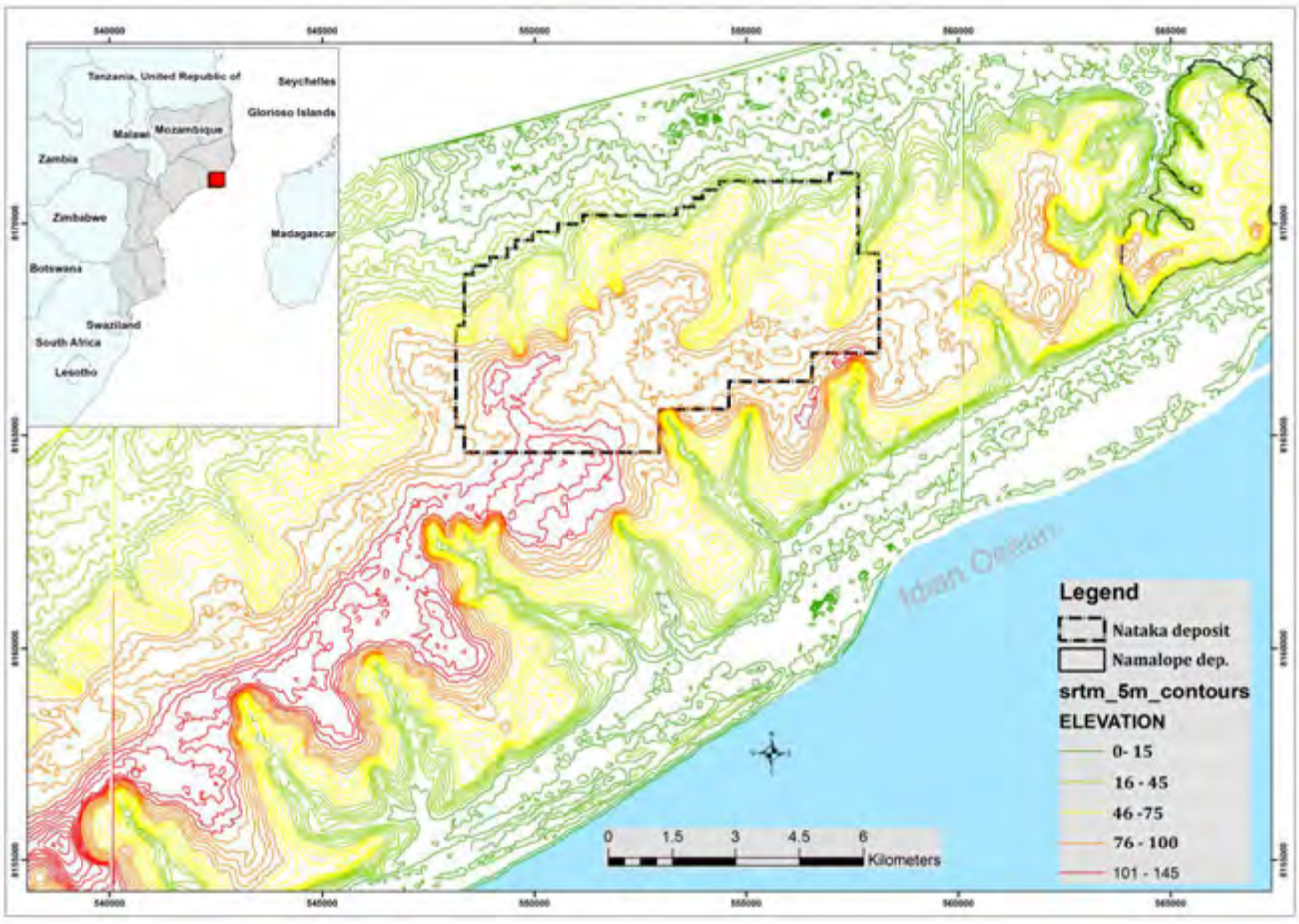

Figure 2. Topographic map of Nataka area. Evident NE-SW trend of the dune geomorphologic structure, surrounded by low elevation areas forming the flood plains. The Nataka deposit is located on the high area.

1.2. PREVIOUS STUDIES

Ilmenite alteration studies have drown attentions of many workers since the discovery by Palmer (1909) of a mineral with a chemical composition close to $Fe^{3+}_2Ti^{4+}_3O_9$, which he called arizonite. In the late 1950's, Bailey et al. (1956) identified 3 stages of ilmenite alteration, ascribed to the devolpment of patchy ilmenite, amorphous iron-titanium oxide, and leucoxene, respectively. The amorphous iron-titanium oxide was further investigated, and Temple (1966) and Teufer and Temple (1966) found out that it was a mineral with disordered hexagonal structure, with a theoretical composition $Fe_2O_3*3TiO_2$, for which they proposed the name 'pseudorutile' (Teufer & Temple, 1966). Later, Grey and Reid (1975) investigated the structure of pseudorutile and its role to the alteration of ilmenite in nature, and proposed two stage model mechanisms for ilmenite

alteration. In the first stage ilmenite is altered to pseudorutile via electrochemical corrosion, taking place below the water table. Progressive alteration of pseudorutile takes place near surface, above the water table, where organic and carbonic acids catalyse titanite and ferric iron dissolution, with titanite precipitating as microgranular rutile or anatase (leucoxene). In addition, a single step alteration of ilmenite into leucoxene was suggested, as a result of prolonged exposure to sun or bushfires (Frost et al., 1986), and interaction of fresh ilmenite with acidic solutions (Hugo & Cornell, 1991).

Actually, the 3 stage model mechanism of ilmenite alteration is however questionable, as it cannot explain the formation of all minerals that result from ilmenite alteration (e.g. hydrated ilmenite), and Hugo and Cornell (1991) proposed a multi-stage mechanism, which also include hydrothermal alteration in the source. In agreement with a multi-stage mechanism, Babu et al. (1994) proposed the Fe^{2+} removal prior to oxidadtion to Fe^{3+}, the latter taking place in situ in the deposit.

The incompleteness of the 3 stage model mechanism (Grey & Reid, 1975) become more pronounced with the validation of hydroxilian pseudorutile (Grey & Li, 2003), as this cannot explain its formation from ilmenite alteration.

In the light of the model proposed by Grey and Reid (1975), much research on ilmenite mineralogy was conducted, and found out that ilmenite alteration progresses from altered ilmenite through leucoxene, and Al_2O_3 and SiO_2 impurities increase with progressive alteration, being more enriched in leucoxene (e.g. Frost et al., 1983; Nair et al., 2006, 2009; Pownceby et al., 2008).

In conjunction with ilmenite mineralogy studies, sediment provenance approaches have also been conducted, however these are few in frenquency. In the west coast of southern Africa is noteworthy the study of Philander and Rozendaal (2015a,b) in the Namakwa heavy sand deposit (300 km north of Cape Town, South Africa). These authors found out that the deposit comprises mostly fresh ilmenite, zircon, and some leucoxene. Other less valuable minerals (garnet, monazite and kyanite) plus small amounts of rutile are likely to occur. The heavy minerals were sourced from medium- to high grade metamorphic terrane [Zr-in rutile geothermometry between 500 ^{0}C

and 950 ^{0}C (Philander & Rozendaal, 2015a)], with the major contribution from the Namaqua Metamorphic Complex (Philander & Rozendaal, 2015b).

In the east coast, among other studies, an example of provenance research was conducted based on monazite chemistry of heavy mineral sands from Egypt, which envisaged pegmatites and granites of the Eastern Desert to be the most likely source, together with heavy mineral assemblages from the Ethiopian and central African terranes (Dawood & El-Naby, 2007).

Recently the World Bank and Nordic Fund supported an extensive cartography program at 1: 250 000 scale throughout Mozambique, undertaken by diverse working groups, such as GTK Consortium, and the Council for Geoscience, to mention some. The study area falls in the area mapped by The Council for Geoscience (2007), however unfortunately the mineralogy of the heavy minerals was not described in detail.

Cílek and Duda (1989) presented the first summary work on industrial minerals of the country, and classified the Ti deposits in two categories: 1) Primary – related to Precambrian rocks, being the gabbro-anorthosite intrusions of the Tete Suite, pyroxenites and alkaline rocks in the Ulongue area (Tete Province) and in the Mazua (Nampula Province) the most important; 2) Secondary – this includes all the placer deposits located along the Mozambican coastline.

In their work, Cílek and Duda (1989), state that deep ilmenite alteration (leucoxenization) is typical all along the several deposits and unaltered grains seldom occur, however the assays show that the TiO_2 range between 46 to 51 weight percentage (wt. %) at the deposits falling at the south part of the country, and from 52 to 55 wt. % at the north (Zambézia and Nampula Provinces), which means slight alteration.

A recent compilation made by Lächelt (2004) also agrees with the findings of Cílek and Duda (1989), and the deposits found at the north are described as being of good quality, given their low impurity levels ($Cr_2O_3 \sim 0.1$ wt. % and $V_2O_5 \sim 0.5$ wt. %) and slightly high TiO_2 (average 55 wt. %). At the south the only deposit of good quality is the relatively new discovered accumulation of Chibuto – Gaza Province (south). Concerning the primary categorization, Lachelt (2004) includes the Lupata occurrence amongst the most important deposits due to its high TiO_2 content of about 60 wt. %.

As in the case of the mineralogy, the provenance of the sediments has only been hypothesized based on the occurrence of heavy minerals (ilmenite, rutile, zircon, and others) in Precambrian rocks making up the Mozambican crystalline basement. Lächelt (2004) tentatively suggested that there was little contribution from the South Africa and Zimbabwe Cratons, as well as from Karoo-age deposits.

Despite the occurrence of numerous heavy mineral sand deposits along the country, nothing has been published on the detailed mineralogy and provenance, beside the early and restricted study undertaken by Bailey et al. (1956) on some beach sand samples collected at the former Vila Luísa (actual Marracuene village), about 35 km from Maputo city.

1.3. AIM AND OBJECTIVES

Despite the advances made in the past, especially on identifying pseudorutile, no comprehensive study was made of the whole range of diagenitic alteration products, and hydrothermal and supergene alteration phases commonly found in heavy minerals, as their diffraction patterns overlap in powder X-ray analysis [e.g. (Grey & Reid, 1975), (Wort & Jones, 1980), and (Nair et al., 2006)], and because of the poorly defined crystalline structure of the alteration products. This factor has hampered accurate determination of heavy mineral assemblages, which is one of the challenges in the heavy mineral industry (Jones, 2009).

However, the combination of the newly developed automated electron diffraction spectrometry techniques (QEMSCAN) with powder X-ray and electron microprobe (EMP) analysis, the mineralogy of heavy minerals concentrates can be rapidly determined.

In the heavy mineral industry, a detailed characterization of ilmenite alteration products is invaluable for the upgrading of ilmenite concentrates to TiO_2-rich products, and also to explain better the occurrence and enrichment in impurities such as Al and Si. This research project was undertaken to determine the bulk mineralogy of the Nataka deposit, characterize the ilmenite, and tentatively explain alteration mechanisms. A provenance approach and generic comparison with other deposits will also be addressed where relevant.

To achieve the aim of this study, a combination of four core techniques, QEMSCAN, XRD, EMPA and LA-ICP-MS, will be used and the following objectives highlighted:

i. Determine the bulk mineralogy and estimate the modal abundance;

ii. Study the mineral petrography and diagenetic alteration of ilmenite in respect of the Ti deportment;

iii. Assess the variation in the level of impurities with increasing alteration;

iv. Characterize the chemistry of ilmenite minerals of the Nataka deposit;

v. Examine the correlation between bulk and granular/particle chemistry;

vi. Determine and use the geothermometry for provenance approach;

vii. Correlate U-Pb ages of zircon to trace the prospective sediments source.

CHAPTER 2. GEOLOGICAL SETTINGS

2.1. REGIONAL GEOLOGY

The Mozambican geology is related to the African plate geotectonic evolution, comprising Archaean cratons and Proterozoic mobile belts, overlain by undeformed sediments and igneous rocks of Neo-Proterozoic, Late-Carboniferous to Early-Jurassic and Cretaceous-Quaternary ages (GTK Consortium, 2006a).

The southern Africa region consists of the Kalahari Craton (Kaapvaal and Zimbabwe), Tanzania and Congo cratons, interconnected by mobile belts (Zambezi, Damara, and Mozambique) formed during orogenic episodes.

In Mozambique, the occurrence of Archaean rocks is related to the Zimbabwe Craton extension to the eastern side of the international border (Lächelt, 2004). The rocks were grouped by GTK Consortium (2006a) into: (1) Mudzi metamorphic Complex, comprising generally metamorphosed TTG (Tonalite, Trondjemite, and Granodiorite); (2) Munhinga and Manica Groups, made up of ultramafic and mafic metavolcanic rocks (talc-chlorite schist, chlorite-amphibolite schist, komatiite), and conglomerate. The Archaean rocks are stratigraphically overlain by metasedments assigned to the Umkondo, Gairezi/Fronteira and Rushinga Groups in the central part of the country, and Ponta Messuli (migmatitic paragneisses, augen gneisses and amphibolites) in the NE part, close to Mozambique/Malawi Lake. The Ponta Messuli Complex is assumed to be part of the Ubedian-Usagaran Belt (Norconsult Consortium, 2007; Bingen et al., 2009; Viola et al., 2008)

Northward the Zimbabwe-Mozambique border, in the Mozambican province of Tete, the rocks have Mesoproterozoic Irumide/Grenville ages (GTK Consortium, 2006d; Kröner et al., 2001), and comprises predominantly metasediments (e.g. Zambue Supergroup, Fíngoè Supergroup), basic and intermediate granulitic rocks (Chidzolomondo Group), granite intrusive suites (e.g. Chiuta Serra, Rio Capoche, Cassacatiza, Serra Davura, Rio Tsafuro), and mafic to ultramafic suites (e.g. Tete, Chipera, Chiticula).

Mesoproterozoic rocks occurrence in the NE part of Mozambique is also noteworthy, and are assembled in Nampula, Marrupa, and Unango major Complexes (Fig. 4). The origin of the Nampula

Complex is still a matter of discussion, being so far associated to the H.U. Sverdrupfjella and Kirwanveggen subprovinces of the Maud Province, east Antarctica (e.g. Groenewald et al., 1991; Bingen et al., 2009; Grantham et al., 2011).

The NE part of Mozambique underwent multiple tectonic deformation process (e.g. Ueda et al., 2012; Meert, 2003; Meert and van der Voo, 1997; Meert et al., 1995; Viola et al., 2008) during the East Africa Orogen – EAO (Stern, 1994).

The EAO features have been recognized on other areas out of Africa, in South America denominated Brasiliano (Meert & van der Voo, 1997), and in Australia-Antarctica (Jacobs et al., 2008), thus the broad term East Africa Antarctica Orogen – EAAO (Kröner, 1977; Jacobs et al., 2008) is used in this study. Therefore the EAAO is defined as a tectonic event characterized by polycyclic deformation, due to the collision of many blocks of East and West Gondwana, preceded by the closure of the Mozambican Ocean (Viola et al., 2008), and resulted in a linear feature stretching from Egypt-Arabia to Dronning Maud Land in Antarctica, passing through Eastern Africa, including Madagascar (Jacobs et al., 2008) (Fig.3).

Meert and van der Voo (1997) subdivided the EAAO in three stages; the first resulted from the collision of India, Madagascar and Sri Lanka with East Africa (Meert, 2003; Meert & van der Voo, 1997) between 800 and 650 Ma and formed the Zambezi and Mozambique Belts, of which the latter will deserve detailed description further in. The second and the third overlap between 600 and 530 Ma; they were characterized by the amalgamation of the South America nuclei and Africa (Brasiliano Orogeny) and the collision between Australia and Antarctica with the rest of Gondwana (Kuunga Orogeny), respectively. Similar approaches with slight age differences were presented by Bingen et al. (2009) and Ueda et al. (2012) whom identified three deformation events in the Lúrio Belt with ages of *ca*. 1050 Ma, 550 Ma, and 500 Ma, respectively.

The EAAO ceased with the assembly of Gondwana and posterior collapse. During its Supercontinent stage (300 and 157 Ma) the development of rift-type sedimentary basins took place; thereafter a period of sea-floor spreading in the Western Somalia, and Mozambique basins (Salman and Abdula, 1995; Scotese et al., 1998) aged between 153.2 Ma and 154.2 Ma (Mahanjane,

2012), then a stabilization period followed notwithstanding the continuous development of marginal basins.

From 35 Ma up to present (Salman & Abdula, 1995), Neo rifting is taking place and the East Africa Rift System (EARS) is the most impressive on the coastal side of the Indian Ocean. The rift system in Africa is associated to alkaline and carbonatites rocks grouped in the Chilwa Alkaline Province (GTK Consortium, 2006d), and forming coeval carbonatite intrusions in Mozambique (Monte Salambidua, Monte Muande, Monte Fema).

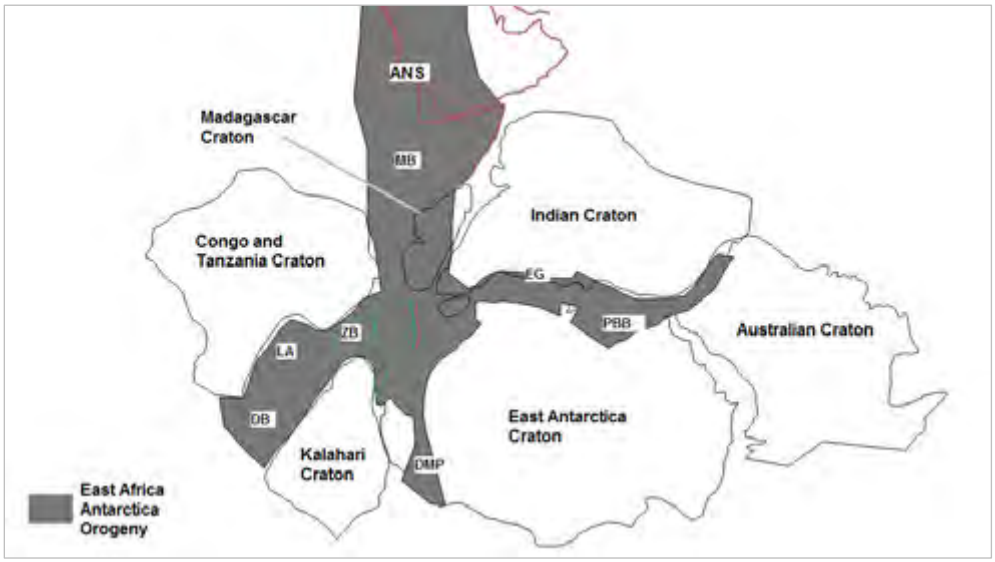

Figure 3. Gondwana reconstruction adapted from Norconsult Consortium (2007), with the location of main African Cratons and Mobile Belts as follow: DB – Damara Belt, DMP – Dronning Maud Province, EG – Eastern Ghats, LA – Lufilian Arc, MB – Mozambique Belt, PBB – Prydz Bay Belt, ZB – Zambeze Belt. The green line shows roughly the center and north of Mozambique and the red brown line the actual continent boundary. (See Meert (2003) for more details).

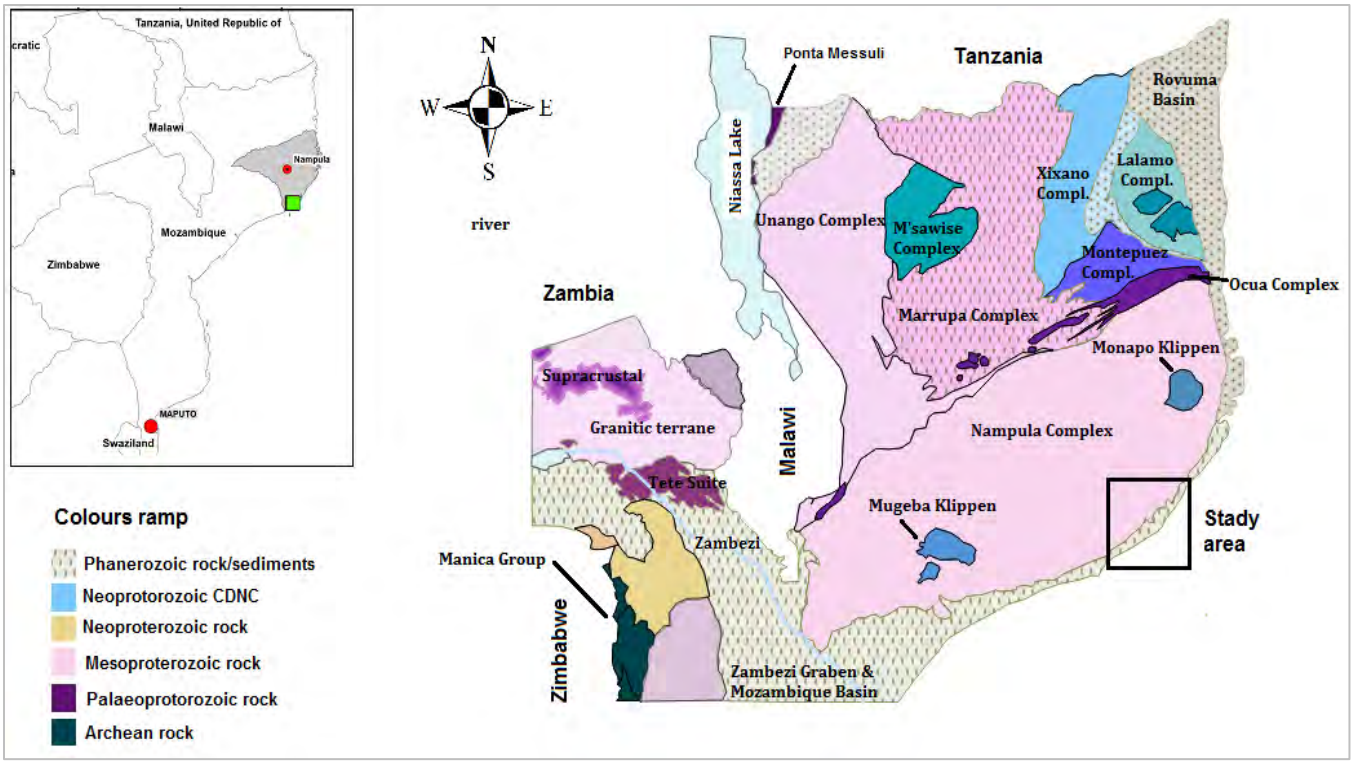

Figure 4. Geological sketch illustrating major stratigraphic units. Each colour stands for a certain geologic period/epoch. Adapted from GTK Consortium (2006) and Viola et al. (2008).

2.1.1. THE MOZAMBIQUE BELT

The Mozambique Belt is a N-S trending feature evolved during the EAAO, characterized by polycyclic reworking of presumable Grenville (Bingen et al., 2009; Macey et al., 2010) lithotectonic units. In the Mozambique area it abuts at the NE with the Phanerozoic Rovuma Basin, Mozambique Basin at the E, S and SSW, and with Irumide trend rocks in the Tete province (GTK Consortium, 2006d); its continuation to other localities is well documented in various workers researches [e.g. In Tanzania by Maboko (2000); in Antarctica by Shackleton (1996), Jacobs et al (1998) and Grantham et al. (2013)].

A recent integrated geological survey program funded by the World Bank and the Nordic Development Fund, documented in several unpublished reports (e.g. GTK Consortium, 2006a, d; Norconsult Consortium, 2007.) and several detailed papers published after the general

unpublished works [e.g. Ueda et al. (2012), Macey et al. (2010), Viola et al. (2008)] discuss the assembly of the NE Mozambique Belt rocks in four major domains, arranged from oldest to youngest as follow: (1) The Paleoproterozoic Ponta Messuli Complex, (2) the Mesoproterozoic Nampula, Unango and Marrupa Complexes, (3) the Neoproterozoic Xixano, Lalamo, M'Sawise and Muaquia, together with the Mugeba and Monapo klippen, grouped by Viola et al. (2008) as "Cabo Delgado Nappe Complex – CDNC"; and (4) the Late-Neoproterozoic Ocua and Montepuez Complexes (see Fig. 4 for the location).

In this thesis, summary descriptions of each domain are presented to make the baseline for sediments provenance approach, as one of the aim of the study, thus the reader is suggested to see Norconsult Consortium (2007), Macey et al. (2007) and other references herein for full lithological characterization.

Ponta Messuli Complex

The Ponta Messuli Complex is exposed NE of the Niassa/Malawi Lake (Fig. 4), consists of migmatitic paragneisses, augen gneisses, talc schist and amphibolites (Viola et al., 2008). The Complex has crystallization age between 2199±21 and 2074±6 Ma and was intruded by the Geci granite (1056±11 Ma) prior to be overlain by the Txitonga Group, made up by meta-sandstones, and schist around 850 – 635 Ma (Bingen et al., 2009).

Nampula, Unango and Marrupa Complexes

The oldest part of the Nampula Complex developed between 1148±2 and 1028±7 Ma (Bingen et al., 2009), and comprises ortho and paragneisses intruded by many granitoid rocks. During the EAAO these were metamorphosed, with the local cover of Ediacaran-Cambrian metasedimentary rocks (Bingen et al., 2009) of the Mecuburi and Alto Benfica Groups. The granitoid rocks are assigned to five groups (Macey et al., 2007): the ***Mocuba Suite*** aged between 1127and 1117 Ma (Macey et al., 2007; Norconsult Consortium, 2007) and with 535±28 Ma migmatization age (Norconsult Consortium, 2007); the ***Rapale Gneisse*** with U-Pb SHRIMP ages at about 1095±19 and 1091±4 Ma; the ***Mamala quartzo-feldspathic gneiss*** dated in 1092±13 Ma; the ***Molócuè Group*** made up of mafic and ultramafic gneisses associated with amphibolites and disperse paragneisses. These rocks yield crystallization ages of 1090±22 and 1090±13 Ma and a ca. 510 Ma

metamorphic age (Macey et al., 2010); the ***Culiculi Suite*** with granitoid orthogneisses crystallization age around 1077±26 Ma and metamorphic ages between 505±10 to 514±37 Ma (Macey et al., 2010).

The Unango and Marrupa Complexes are roughly contemporaneous and share the continental arc setting origin around 1063±13 and 946±11 Ma (Bingen et al., 2009), although the Unango Complex being slightly older. The Unango Complex comprises orthogneisses, including charnockitic gneiss and granitic to granodioritic gneisses. The rocks underwent high-grade metamorphism between 569±9 to 527±8 Ma (Bingen et al., 2009) and were intruded by alkaline rock of the Niassa and Malema Suites with ages bracketed between 519±6 and 507±7 Ma (Norconsult Consortium, 2007).

The Marrupa Complex consists of felsic gneisses associated with magmatic and metasedimentary rocks. Neoproterozoic overprint was observed in many rocks and supported by ages ranging from Stenian-Tonian, Cryogenian and Ediacaran to Cambrian (Bingen et al., 2009).

Cabo Delgado Napple Complex (CDNC)

This domain was proposed by Viola et al. (2008), comprises the Xixano, Lalamo, M'Sawise, and Muaquia Complexes, including the far south located Muageba and Monapo klippen (Fig 4). Their origin and tectonic evolvement is still contentious. Although several workers have conceived the proposed assembly and linking it with the East Antarctica (e.g. Jacobs et al., 2008; Viola et al., 2008; Grantham et al., 2011), Melezhik et al. (2008) presented evidence that contradict such a common genesis, using isotope chemostratigraphy of the marbles outcropping the Complexes.

The CDNC lithology varies within the domain, however is broadly made up of granitic, tonalitic, gabbroic, amphibolite gneisses, paragneisses, metavolcanic and mafic granulites (Viola et al., 2008). Marble layers and graphite schist outcrop essentially in the Xixano and Lalamo Complexes. Indicative ages of the marbles range between 800 – 740 Ma in the Xixano Complex (Melezhik et al., 2008) and the peack metamorphic ages are ca. 635 Ma (Grantham et al., 2011) and 591± 4 Ma (Macey et al., 2007) in the Monapo and Mugeba klippens respectively.

Ocua and Montepuez Complexes

The Ocua Complex makes up the Lúrio Belt and bounds the Nampula Complex at the north and the CDNC, together with the Unango and Marrupa Complex at the south. Its belt-like structure is more evident at the eastern part and becomes more diffuse at the western (Viola et al., 2008).

The belt-like structure associated with intense deformation of the Ocua Complex is consistent with it being the N-S suture zone of East and West Gondwana and this has been suggested in many reconstruction models [e.g. Sacchi et al. (2000)]; however recent structural and geological works question such hypothesis and position the prospective suture in Antarctica, concealed by enormous ice mass [e.g. Shackleton (1996); Viola et al. (2008); Bingen et al. (2009)].

The Ocua Complex is a tectonic mélange evolved in multiple deformation and intrusions (Ueda et al. 2012). It comprises mafic to felsic granulites, banded and mylonitic leucogneisses, granite gneisses, amphibolite, metadiorite, syenite, marble and ultramafic rocks (Norconsult Consortium, 2007). The age range follows the evolution history and exhibits variegated periods. The magmatic age is bracketed between 978±34 and 768±19 Ma, and the amphibolite to granulite metamorphic-facies took place around 606±4 and 540±7 Ma (Norconsult Consortium, 2007; Ueda et al., 2012).

The Montepuez Complex is made up by quartzites, meta-arkose, marble, quartz- feldspartic gneiss, biotitic-gneiss (Norconsult Consortium, 2007). The age of clastic sediments deposition lays at 942±14 Ma, and for the marble between 800 – 600 Ma and 740 – 670 Ma for the West and East layers, respectively (Melezhik et al., 2008).

2.2. LOCAL GEOLOGY

The study area is a strand dune characterized by marine geodynamic features and dominated by Cenozoic Formations, Fe-Al oxyhydroxides, colluvial evolvement and soils, alluvial deposits and shoreline sediments, associated with basaltic and andesitic lavas of the final Gondwana assemblage period. On the edge of the far north hinterland, dispersed inselberg intrusions of the Nampula Complex are the pronounced high points (Fig. 5).

The Red Dune forms the most prominent Cenozoic feature laying from Ponta Selela (Sangage) to Baía de Mocambo (Macey et al., 2007), locally veneered by unconsolidated grayish fine sand. The Red Dune makes up a regional beach ridge ["Beach-ridges are progradational landforms occurring in the foreshore and considered the product of wave and wind deposition occurring at the upper limit of wave run up" - Taylor and Stone (1996)] that extends from Somalia through Kenya, Tanzania and Mozambique, to Richards Bay in South Africa. Its origin is associated with a regional period of erosion (Greig, 2001) and sea-level fluctuation during Pleistocene and Holocene (Ramsay, 1996; Ramsay & Cooper, 2002).

In the Mozambican district of Moma, the Red Dune extends over 50 km southwest of Namalope deposit (current mine location) and contains high levels of total heavy minerals (THM). The Nataka deposit (study area) is one of such a high concentration of THM, estimated at 141 Mt (Rothnie, 2011). Thereafter the Red Dune is referred as the Topuito Formation, and together with other relevant lithostratigraphic units are described below based on textbooks and/or field observations.

Angoche Group

This extends from Moma to Angoche and along the Congolone – Sangage Peninsula (Macey et al., 2007), and defines the main lithology of the low relief zones. Outcrops are scarce with some exposed due to steep-side pervasive erosion of the Red Dune structure or along the rivers.

The Group consists of basalts and andesites, with calc-alkaline character. The geochemical signature of these rocks is different from the flood bi-modal lavas of the Karoo period. The rocks have 174± 14 Rb/Sr age, and zircon SHRIMP U-Pb ages bracketed between 494 and 716 Ma (Macey et al., 2007).

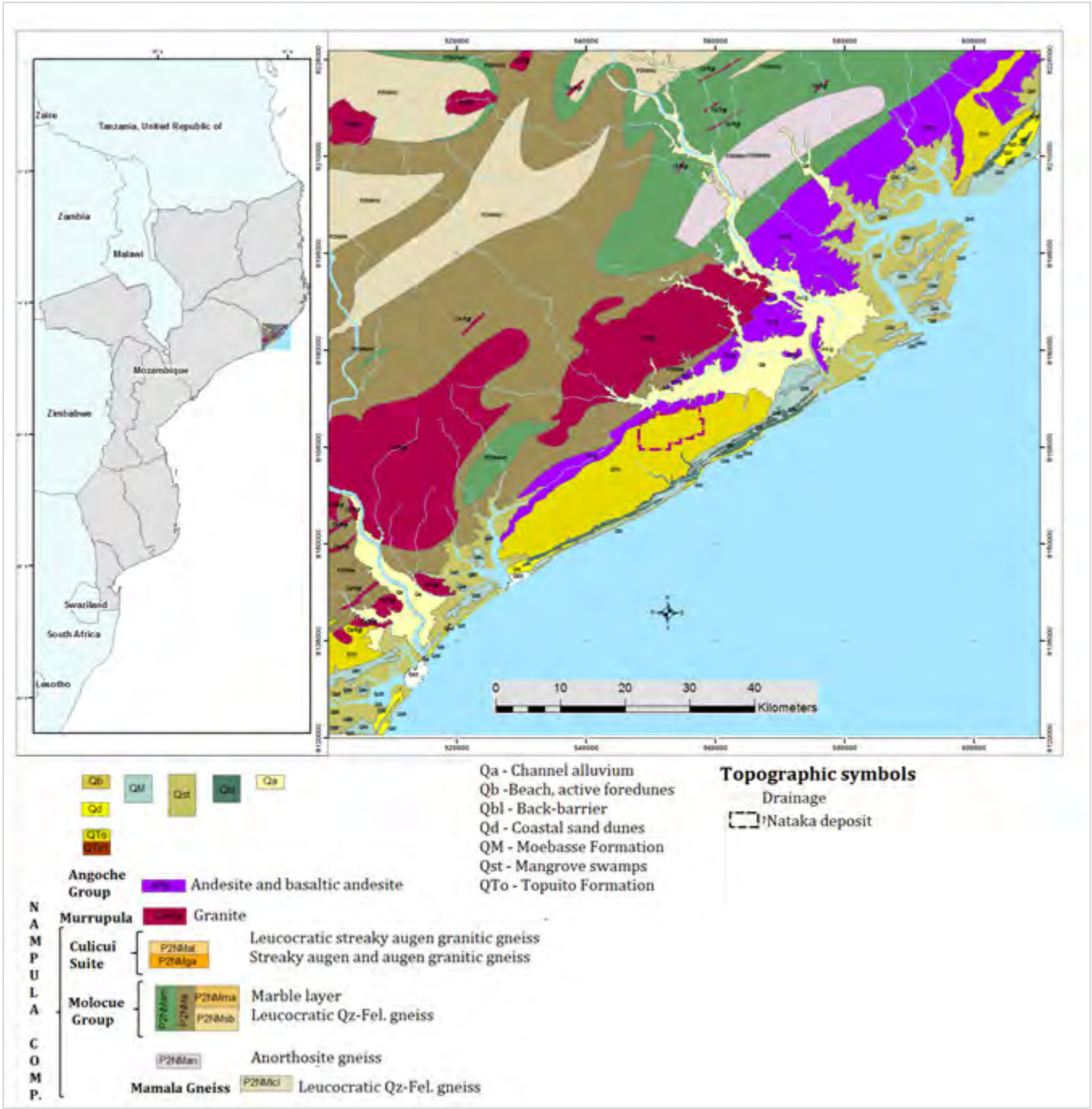

Figure 5. Geological map of the study area and surroundings. Modified after Ingram (2005), Sheet 1639-40 Angoche.

Topuito Formation

This formation makes up a sub-parallel coastal dune structure of 10 km wide, roughly 50 km long, which rises to more than 100 m amsl. It consists broadly of sandy clay overlain by red sands (Macey et al., 2007), locally covered by Holocene sediments (Topuito and Tibani areas) of the Moebase Formation. Ferricrete and calcrete crop out more often close to river streams, form circular mount-like structures, and consist of poorly sorted detrital quartz, feldspar and lithic fragments cemented by Fe-Al-oxyhydroxides (Macey et al., 2007).

Grain size, THM contents and colours vary within the Formation, hence subdivision into units was adopted. Summary descriptions follow below, and a schematic vertical section presented in Figure 6.

- **Unit 1**

This comprises clean yellowish, well sorted fine to medium grain sand, assigned to the Moebase Formation that locally overlain the red sands. The overall thickness is about 12 m, however at some points can be of approximately 25 m. The sand is almost free of clay (~5 %) and has THM ranging between 3 to 6 %.

- **Unit 2**

It is the top of the Topuito Formation, and consists of slightly silty sand to silt, light orange to red brown very fine, fine and medium moderately well sorted sand. Clay content increases with depth, but commonly ranges from 6 % to 12 %, with THM grade average of 3 %. Irregular occurrence of thin layers intercalation with high THM grade (> 6 %) or higher clay contents are localy observed.

- **Unit 3**

This unit is very silty with minor plastic clay, red brown to red, fine to medium well sorted sand. Clay content is between 15 – 25 % and THM around 2-4 %.

- **Unit 4**

This consists of very silty or clayey, poorly sorted fine to coarse sand. It is generally reddish brown to pink in colour, however mottling to gray or dark red is also observed. The clay content is generally greater than 25 % and locally close to 100 % (plastic clay).

Moebase Formation

This formation resulted from reworking and deposition of Pleistocene sediments during the early Holocene, and occupies the coastal strip from Quelimane to Quinga (Macey et al., 2007). In some areas (Namalope) its deposition further landward is related to river channel infill. Its well-studied portion is at the side of the Topuito Formation and comprises six units, of which Units 81 and 82 are clay lenses below Unit 6 or Unit 7 respectively (Fig. 6).

- **Unit 5**

This comprises clean white to light gray, medium to coarse grain sand. Generally it has negligible clay and total heavy minerals (THM) contents.

- **Unit 6**

It is made up by clean, grayish to white, fine to medium grain sand. Spot variations to pale brown, medium to coarse sand are locally noted. The average thickness is about 6-9 m and the clay content not greater than 12 %, with THM mode of 3-6 %. This unit overlays the Unit 7, however locally a clay lens (Unit 81) marks the discontinuity between them.

- **Unit 7**

This unit consist of clean white to yellowish, poorly sorted silty to very fine, with coarse to gravel sand. The clay content is greater than 15 % and the THM close to 1 %. It shows a localized discontinuity with Unit 9, which is delimited by a plastic gray or dark red clay lens, the Unit 82.

- **Unit 9**

This comprises clean white to grayish poorly sorted sand. It may also contain clean gritty and pebbly intervals, very fine white micaceous sand, angular feldspars and quartz grit, limonite, amphiboles, epidote, rare pyrite, and abundant non-valuable heavy minerals (Rothnie, 2011).

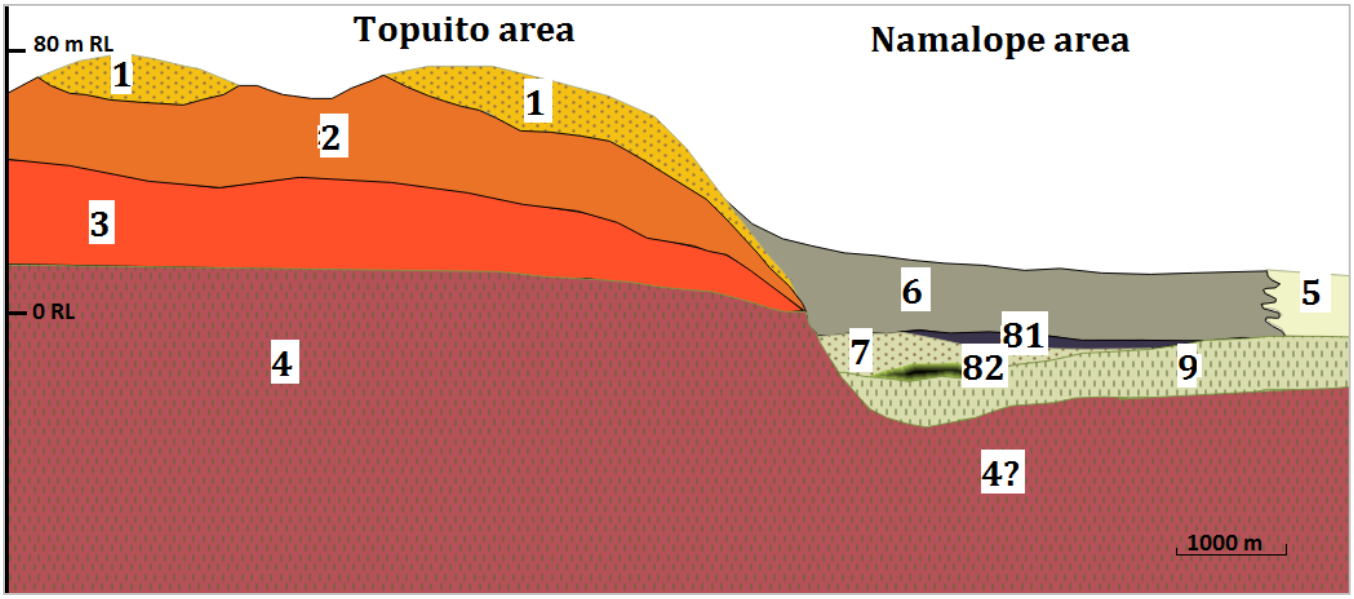

Figure 6. Schematic cross section of the Topuito and Moebase Formations around the well-studied Topuito and Namalope area. Modified after Greig (2001). The numbers in white boxes stand for geological units. 1- Yellowish, well sorted fine- to medium grain sand, THM generally greater than 6 %. 2 – Light orange to red brown silty sand to silt, average THM not greater than 3 %. 3 – Red brown to ton-red silty with minor plastic clay. 4 - Red to pink silty to clayey unit. 5 – White to light gray, medium to coarse grain sand. 6 - Grayish to white, fine to medium grain sand, low clay contents and THM between 3 and 6 %. 7 – White to yellowish poorly sorted sand, locally coarse to gravel grain- size. 9 - White to grayish poorly sorted micaceous sand; locally contain clean gritty and pebbly intervals. 81 and 82 – generally gray plastic clay.

CHAPTER 3. APPROACH AND METHODOLOGY

To achieve the outlined aims and objectives, a combination of diverse analytical techniques was crucial; thus electron microscopy scanning (QEMSCAN), X-ray fluorescence, X-ray diffraction, and electron microprobe were performed. Detailed descriptions for each are presented below.

3.1. SAMPLING AND SAMPLES PROCESSING

The sampling process was performed in Reverse Air Circulation drill holes spaced on a 400 x 200 m grid. The drilling stage was undertaken during the exploratory program by Kenmare Resources Plc from 2008 to 2012. Drill hole locations were planned by a mean of *Arcgis* (geographic information system software), and supported by *Easimine* (computer system for processing and displaying mining and exploration data) for depth determination.

Due to expense, confidentiality and time-related limitations, the 16 drill holes (12 to 75 m deep) selected for this research do not cover the 400 x 200 m typical spacing, however they tend to transversely cover the whole deposit specially the eastern side as the one with better mineable conditions (Fig. 7). A total of 32 samples, predominantly 1 m length (about 12 kg) were collected from the base and top of each selected drill hole (Appendix A), aiming to assess the level of ilmenite alteration with depth.

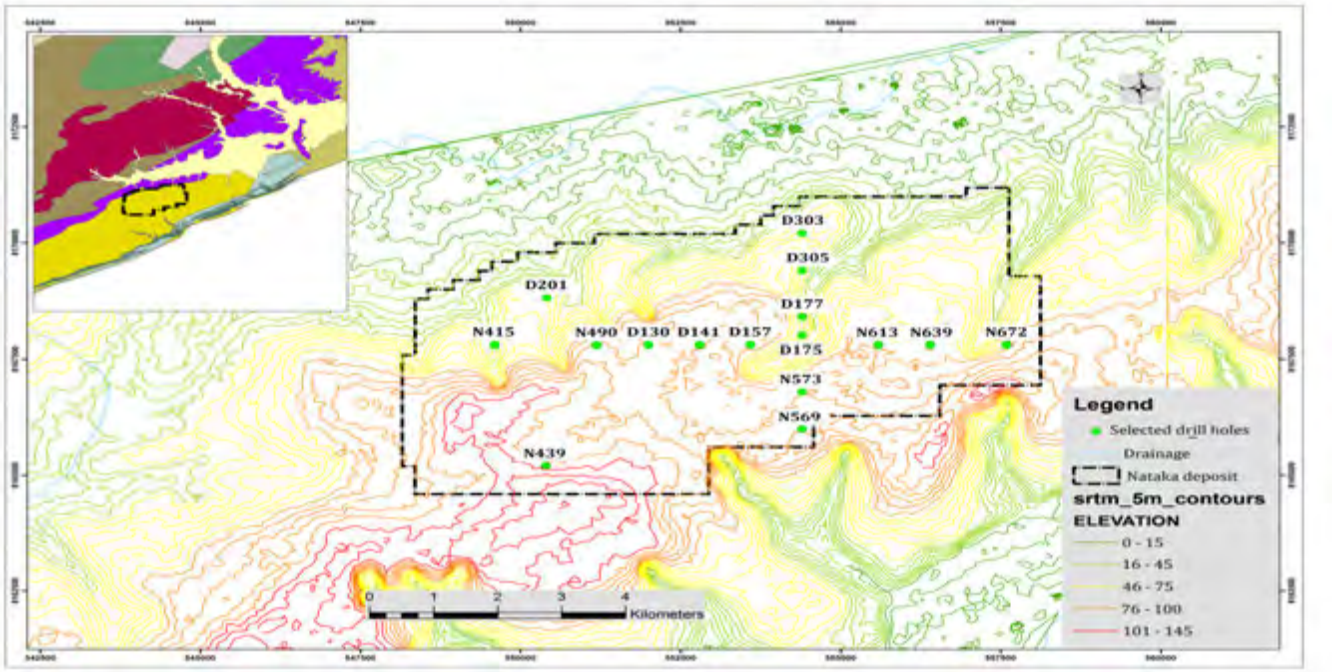

Figure 7. Map showing location of sampled holes within the Nataka Deposit.

Each sample was allowed to drain by exposing during 2 days under the sunshine, followed by oven drying at 110 ^{o}C (±5 ^{o}C). Thereafter, the sample was manually crushed to disaggregate the "lumps", and passed through a 2 mm sieve to remove roots and coarse material prior to quartering into about 500 g in the rotary splitter, and finally drawn to about 100 g in the riffle splitter.

The 100 (±5) grams obtained on previous steps, were screened using a stack wet sieve of 1 mm and 0.045 mm (45 micron) to draw out the finer material (*clay*) and separate the coarse (*Oversize*) from the fine-medium – *Withinsize* (in between 0.045 and 1 mm).

Both the *Oversize* and *Withinsize* were oven dried at 110 ^{o}C (±5 ^{o}C) and weighed for *Oversize* abundance and *Clay* content determination (Formula 1 and 2). The *Withinsize* were then put into 500 ml separating funnels containing 150 ml of 2.85 g/ml heavy density liquid of lithium heteropolytungstate (commercially named LST), which is less dangerous to work with than traditional heavy liquids such as the toxic tetrabromoethane and bromoform (LST heavy liquid, 2003.; "Technical and other…", n.d.). The floating material separated by this method was discarded and the material denser than the liquid was collected onto a filter paper and washed with dionised water before oven drying (Fig. 8).

The process above described was repeated 5 times on each sample to allow enough material to be obtained to carry on with all planned analysis.

$$\%Oversize = \frac{[Oversize\ weight]}{[Initial\ sample\ weight]} * 100 \quad [1]$$

$$\%Clay = \frac{[Initial\ sample\ weight] - [(Oversize\ weight) + (Withinsize\ weight)}{[Initial\ sample\ weight]} * 100 \quad [2]$$

In order to simplify the grain picking stage undertaken during preparation of mounts for Electron Microprobe analysis, the bulk THM of each sample was magnetically separated into two fractions, using a Reading Roll Magnetic Separator. The magnetic intensity was initially set to 2.2 Amps and 150 RPM (Revolutions per Minute). To effectively clean the non-magnetic fraction from magnetic gangue, the fraction was repeatedly passed through the separator and the intensity increased to 3.6 Amps. The material obtained after the first magnetic cylinder roll was termed *Mid* (short form of middle magnetic) and later added to the magnetic fraction.

Overall, the non-magnetic fraction of the samples under consideration ranged between 5 and 15 %, and in order for enough material to be available for XRF analysis, some samples have been combined as will be explained below.

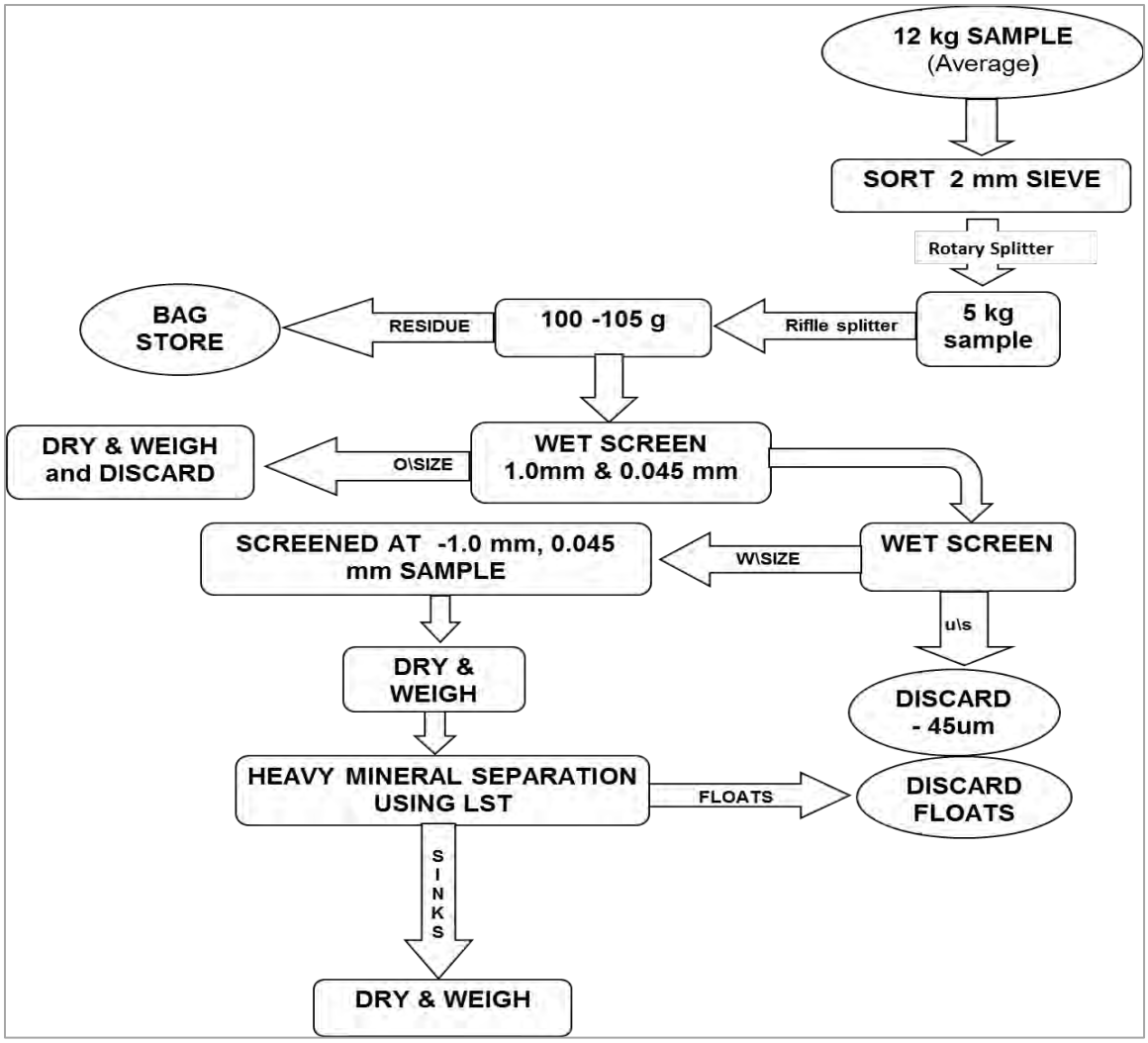

Figure 8. Simplified samples processing flowchart.

3.2. ANALYTICAL TECHNIQUES

- **X-ray fluorescence**

The sample preparation and the XRF analysis were undertaken in the Kenmare Moma laboratory facilities and at the University of Cape Town, following the steps described below.

At the Kenmare Moma laboratory, analysis by XRF covered major and minor elements, so about 10 g of sample was obtained by adding together different drill holes with similar geological features (THM, Clay and Oversize), to achieve the minimum mass required for this analysis, specifically for

the non-magnetic fraction (see Apendix B). The heavy mineral fractions, magnetic and non-magnetic, were carefully milled using swing discs to 75 μm grain size, prior to mixture with borate and fusion in platinum-gold crucible at about 950 – 1050 ^{o}C. Loss on ignition (LOI) values was obtained by weighing the crucible before and after heating.

Single samples were analysed at the University of Cape Town by XRF, and this was undertaken only for major elements because trace elements require 6g. Provisions to mensure zirconium (Zr) were made and are clearly explained in the table (Appendix B). The H_2O and LOI were obtained by weighing the sample powder after heating at 110 ^{o}C and post ignition at 800 ^{o}C.

- **X-Ray Diffraction**

Powder X-ray diffraction spectrometry was performed in the Department of Geology, University of Cape Town, using a Philips X-ray diffractometer panalytical PW3830 set at 40 kV and 25 mA. A total of 22 samples (16 of magnetic fraction and 6 bulk) have been studied. The samples were carefully milled in an agate mortar before mounting in a plastic cavity plate sample holder, and flattened using a glass plate to avoid preferential grain orientation (e.g. Jenkins et al, 1995; Zussman, 1967).

- **Quantitative evaluation of mineral by scanning microscopy (QEMSCAN®)**

Automated mineralogy techniques have been extensively applied in the mining industry for plant optimization, and the QEM*SEM being the most popular. Recently, many authors have demonstrated the efficiency of automated mineralogy in the research field with focus to QEMSCAN (e.g. Andersen et al., 2009; Rollinson et al., 2011; Goodall & Scales, 2007; Ayling et al., 2012).

The **QEMSCAN**® was developed in Australia and built on the basic functionalities of the QEM*SEM (Quantitative Evaluation of Minerals by scanning electron microscope). Operative and measurement modes are clearly detailed by Gottlieb et al. (2000), Pirrie et al. (2009) among others.

For this research, electron scanning was carried out at the Centre of Mineral Research, Faculty of Engeineering, University of Cape Town, using a QEMSCAN FEI 650F, equipped with two Bruker XFlash 6130 detectors, and operational conditions set to 25 kV, 10 nA beam current, and field

emission gun (FEG) steps of 5 microns. Each determination was based on 1000 X-ray counts. Equipment calibration was done using Au, Cu and SiO_2 standards. Assays were compared with analytical XRF results for data validation, good correlation was observed, and maximum variance (about 10 %) is found for Fe and Ti. Data exploration was achieved using a computer with iDiscover v. 5.3 software package. This technique was performed over 32 grain mounts (corresponding to all the samples selected), for modal analysis approach, and morphology and textures studies of the grains by mean of particle mineralogical analysis (PMA). Sample preparation steps are briefly presented in Figure 9.

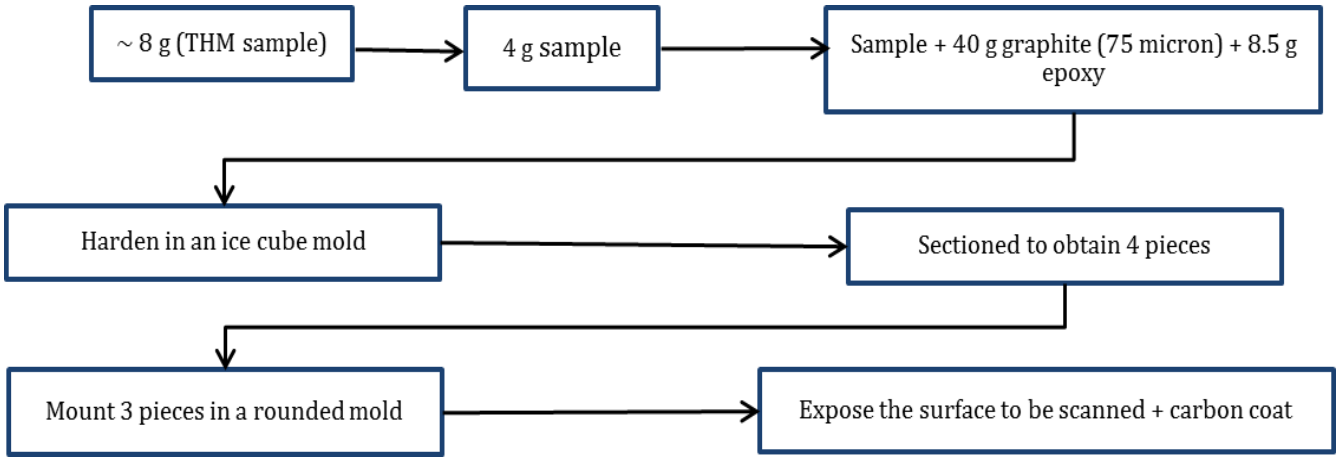

Figure 9. Summarized steps for samples preparation to be analysed by the QEMSCAN.

- **Electron microprobe analyser (EMPA) for mineral composition**

Electron microprobe analyses were applied for spot characterization of Ti-oxide minerals mounted on 6 rounded epoxy resin blocks. The analyses were performed at the University of Cape Town, Department of Geological Science, using a JEOL JXA 8100 microanalyser; with a focused beam, set to 15 kV accelerating voltage, 20 nA of beam current, at a counting time of 5 s and 10 s on each background and peak, respectively. Instrument calibration was done using natural standards of ilemite for Fe and Ti, chromite for Cr, rhodocrosite for Mn, and spinel for Mg.

- **LA-ICP-MS for U-Pb dating**

Three distinct zircon fractions were selected under a binocular reflected light microscopy from a bulk sample of zircon concentrate, based on their colours and morphology. For each zircon

fraction, about 100 zircon grains were mounted in epoxy round blocks, ground to expose grain surfaces, and then U and Pb concentrations and Th/U measured.

The analysis were performed at the ICP-MS & XRF Laboratory, University of Stellenbosch, and comprised image acquisition using a Zeiss Merlin FE SEM (Field Emission Gun-Scanning Electron Microscope), equipped with a cathodoluminescence detector and SmartSEM software for data explorer, 20 kV accelerated voltage and beam current of 11nA; and measurements taken with a Thermo Element 2 high resolution laser ablation sector field inductively coupled plasma mass spectrometry (LA-SF-ICP-MS) connected to a Resolution M-50-SE Excimer laser [for detailed instrumentation and data acquisition see Frei & Gerdes (2009)].

Instrument calibration was done using the standard zircon GJ-1 (e.g. Jackson et al., 2004) prior to analyses and rerun after every 10 consecutive analyses of unknown zircons.

Data reduction was done using an in-house Excel spreadsheet, and presented in combined probability and binary frequency diagrams (Sircombe, 2000). All U-Pb data were prior filtered to 90 – 110 % concordance, 2σ error, and only $^{206}Pb/^{238}U < 1000$ Ma and $^{207}Pb/^{206}Pb > 1000$ Ma reported, due to their good precision (e.g. Gehrel et al., 2009; Xia et al., 2004; Ireland et al., 1998)

- **Laser Fluorination for O-isotopes**

Oxygen isotopes analyses were performed on three morphologically different zircon fractions (brown prismatic, transparent prismatic and transparent rounded), hand-picked under a binocular reflected light microscopy from a bulk zircon concentrate, using the facilities at the Department of Geological Science, University of Cape Town. The analytical procedure followed the laser fluorination method described by Harris and Vogeli (2010). Between 2 and 3 mg of each sample was reacted with approximately 10 kPa BrF_5. Thereafter, the purified O_2 collected onto a 5 Å molecular sieve contained in glass storage bottle (Harris & Vogeli, 2010). The yield of O_2 gas obtained was consistent with complete reaction of each sample.

The $^{18}O/^{16}O$ ratio was measured off-line using a Finnegan DeltaXP mass spectrometer, in dual inlet mode (Harris & Vogeli, 2010). The results were reported using delta notation in per mil ($\delta‰$), calculated relative to Standard Mean Ocean Water (SMOW) following equation: $\delta^{18}O$ =

($R_{sample}/R_{santard}$ -1)*1000, where R = $^{18}O/^{16}O$ and SMOW the standard. The measured value of the Mon Grt (Monastery garnet) standard analysed with each batch of samples was used to convert the raw data to the SMOW scale assuming a Mon Grt $\delta^{18}O$ value of 5.38 ‰. Mon Grt was run in duplicate with the zircon samples. The long-term average difference between duplicate $\delta^{18}O$ values of Mon Grt is 0.12 ‰ (n = 185). This corresponds to a 2σ error of 0.15 ‰.

CHAPTER 4. RESULTS AND DISCUSSION

4.1. MINERALOGY

4.1.1. BULK MINERALOGY AND MODAL ABUNDANCE

Combined automated energy dispersive spectrometry (EDS) by mean of QEMSCAN and diffraction spectroscopy (XRD) were used to determine the mineral assemblage of the deposit. The XRD was employed to assess the magnetic and bulk fraction, aiming to identify different phases. Many diagenetic alteration phases of ilmenite were found [e.g. Altered ilmenite, pseudorutile ($Fe^{3+}{}_2Ti^{4+}{}_3O_9$)] and may be hydrothermal [pseudobrookite ($Fe^{3+}{}_2Ti)O_5$], as will be discussed further in. These minerals are associated with hematite, staurolite, anatase, rutile, quartz, clay minerals (kaolinite and muscovite), zircon and kyanite (Fig. 10 and Appendix C).

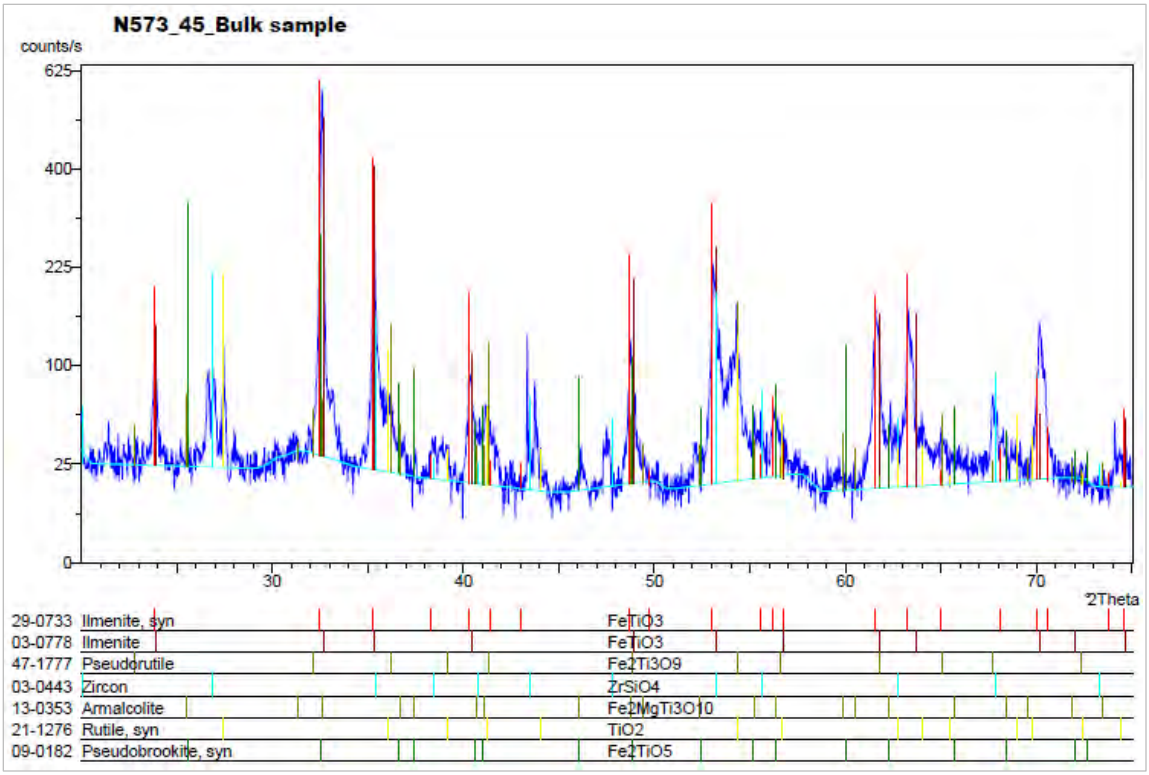

Figure 10. Bulk sample diffraction pattern. The red lines stand for ilmenite, either unaltered (syn) or altered. Sub-horizontal cyan line represents the background.

The quantitative evaluation by electron scanning microscopy emphasizes the predominance of ilmenite (altered or non-altered), at about 50 % (Fig. 11), co-existing with rutile (primary and secondary), Ti-magnetite, zircon, chrome-spinels, monazite, staurolite, kyanite/andalusite, tourmalines and other minerals in few concentrations, grouped under **Others** (epidote, enstatite, pyrite, apatite, among others). No pronounced vertical neither horizontal trend was observed on the bulk mineralogy of the deposit, as pictured by saw-fashion pattern on Figure 12, however, bottom samples are mostly enriched in pseudorutile and leucoxene, and no clear pattern for ilmenite-hematite.

Low temperatures TiO_2 polymorphs (anatase and brookite) were scarcely identified by XRD spectroscopy, therefore an alternative identification method, based on Nb, Cr, Sn, Fe, V, and Zr concentrations (ppm) in TiO_2 minerals (see Triebold et al., 2011) was used. For 119 analysis obtained by mean of QEMSCAN, the method gave 53.78 %, 40.34 % and 5.88 % likely rutile, anatase and brookite, respectively.

Detrital minerals in the deposit vary in size from 45 μm <Θ<100 μm to <500 μm, with some dominantly aluminosilicates (tourmaline and staurolite) falling over that range. The grains are predominantly sub-rounded to well-rounded, it is, between aspect ratio 0.8-1.0 and roundness 0.6-1.0 (Fig. 13) [for further explanation on quantitative description of grain morphology see e.g. Bagheri et al. (2015), Ahmed (2010), Little et al. (2015)].

The oxyhydroxides make up the amorphous coating material and consist essential of goethite and limonite (Fig. 14a).

Quartz, rutile and tourmalines often form aggregates cimented by clay minerals (kaolinite, muscovite, montmorillonite). This mélange generally forms haloes on altered grains, more commonly on ilmenite, and fill shrink cracks and pores created by leaching of Fe during alteration (Fig. 14b).

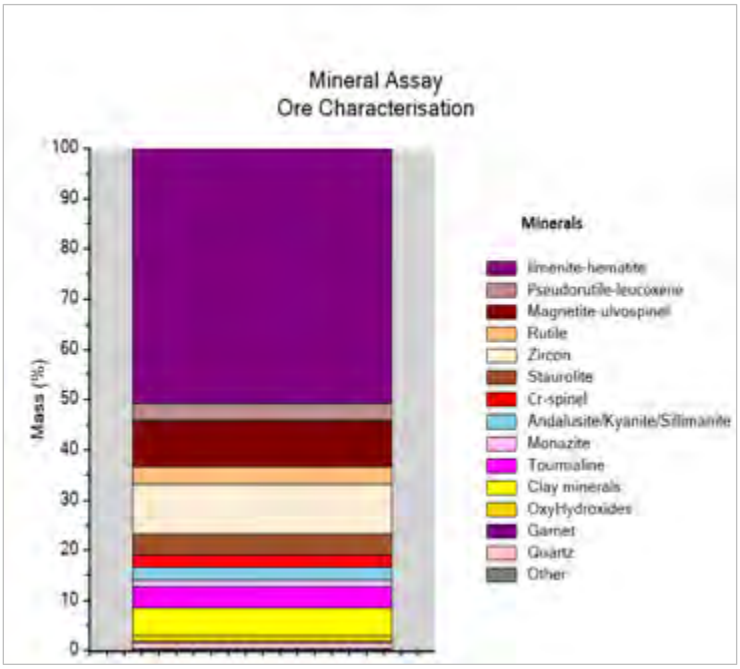

Minerals	Mass (%)
Ilmenite-hematite	50.91
Pseudorutile-leucoxene	3.32
Magnetite-ulvospinel	9.17
Rutile	3.52
Zircon	9.96
Staurolite	4.23
Cr-spinel	2.43
Andalusite/Kyanite/Sillimanite	2.56
Monazite	1.14
Tourmaline	4.26
Clay minerals	5.55
OxyHydroxides	1.15
Garnet	0.15
Quartz	1.37
Other	0.28

Figure 111. Modal abundance of Nataka heavy mineral deposit determined by QEMSCAN. Pictorial by column chart at the left side and tabled in the right. Both show clear predominance of ilmenite. N = 32 samples (~ 95 % THM), SDV = 0.018.

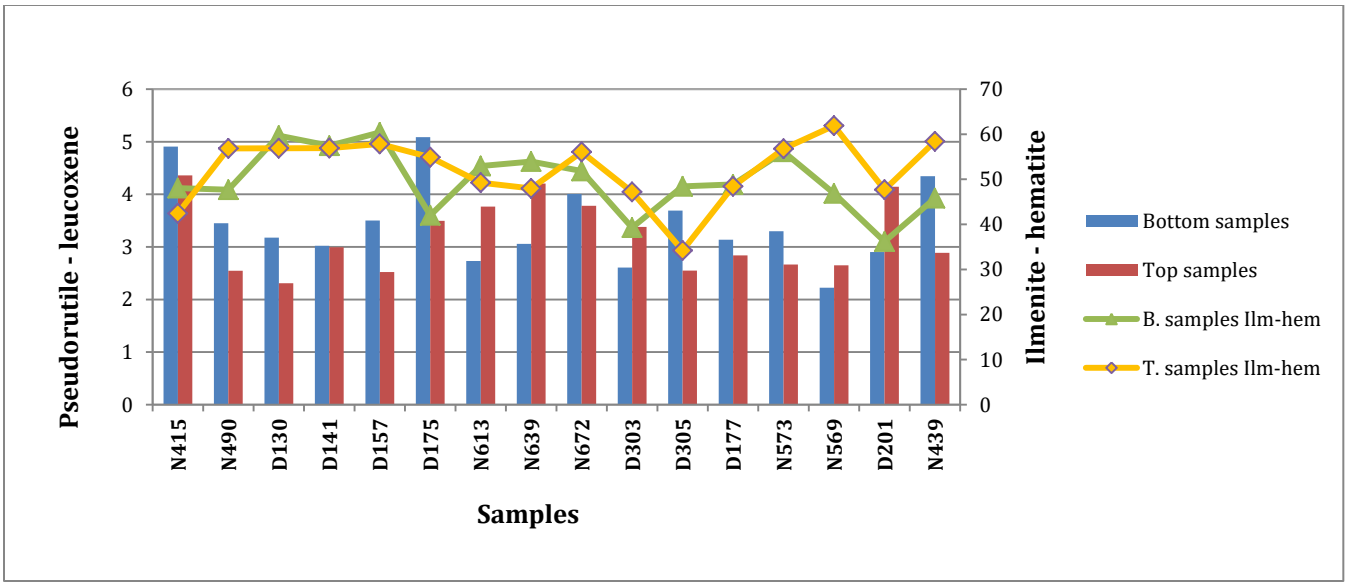

Figure 122. Bar chart of pseudorutile-leucoxene and ilmenite-hematite modal abundances from QEMSCAN results. Both distributions exhibit saw-fashion pattern. Bottom samples are mostly enriched in pseudorutile and leucoxene, and no clear pattern for ilmenite-hematite. B – bottom and T – top.

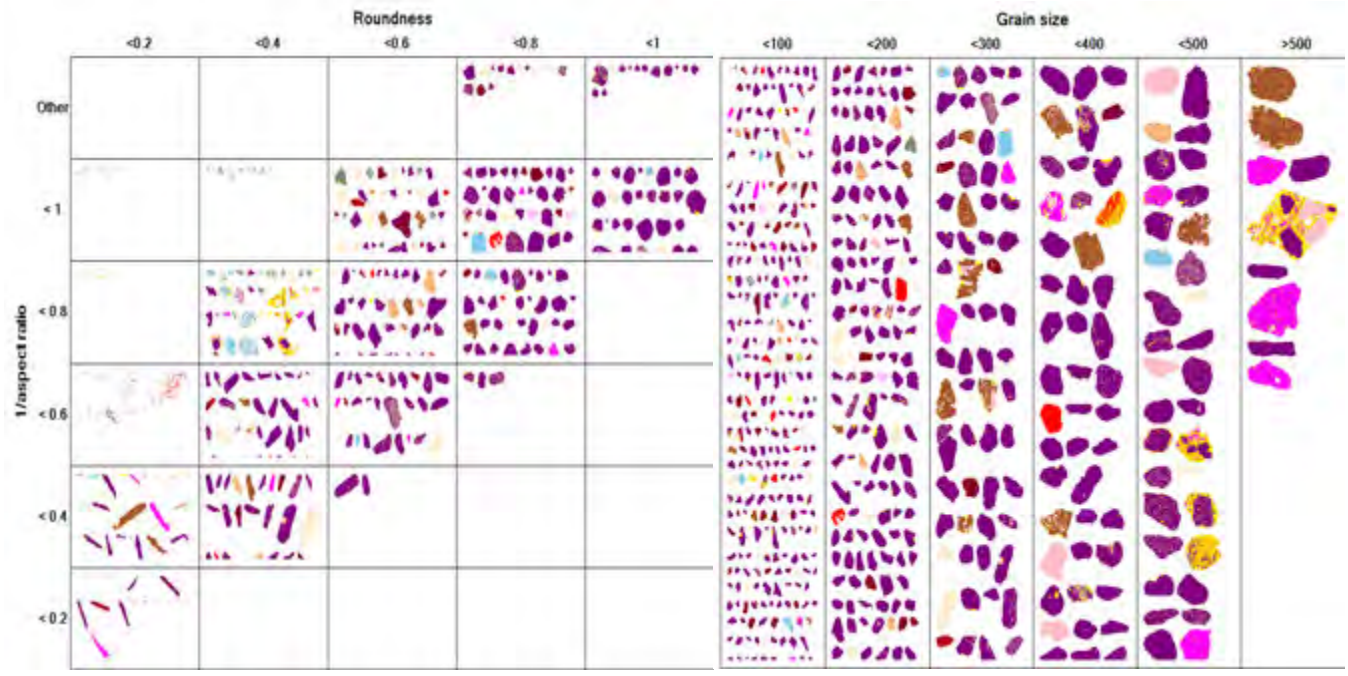

Figure 13. Quantitative particle morphology factor descriptors on the left and grain size distribution on the right. Modified from Little et al. (2015). The roundness improves towards 1.

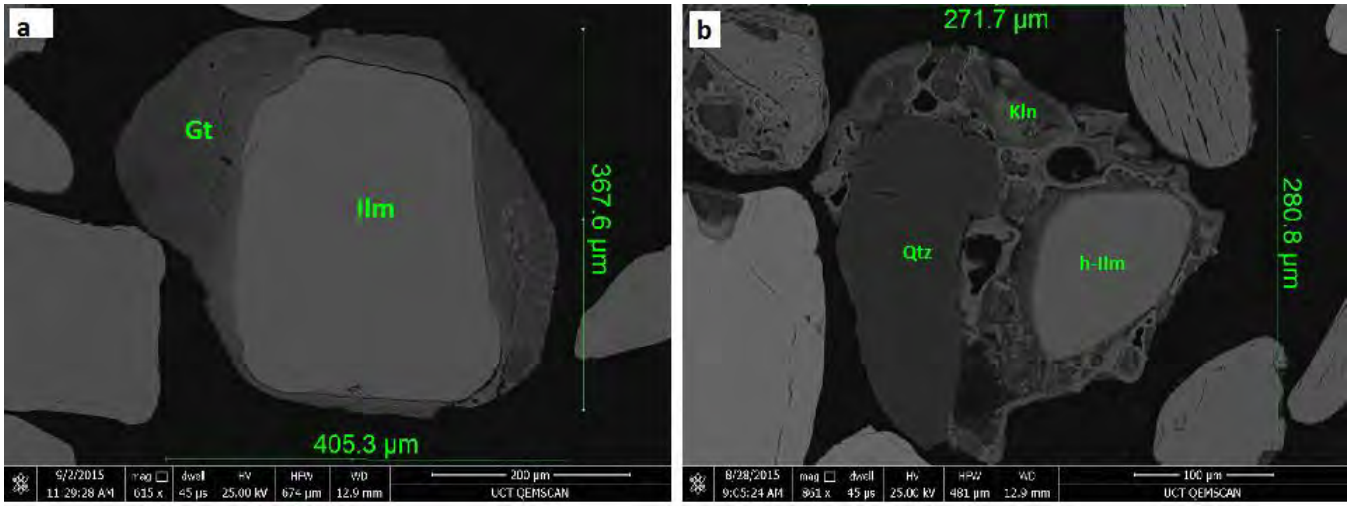

Figure 14. Backscatter images from QEMSCAN. a) Unaltered ilmenite grain surrounded by goethite. b) Agglomerates of quartz and ilmenite grains in kaolinite. Key: Gt = goethite; h-Ilm = hydrated ilmenite; Ilm = ilmenite; Kln = kaolinite; Qtz = quartz.

4.1.2. ILMENITE PETROGRAPHY AND CHEMISTRY

The ilmenite mineralogy has been controversial since early 1900's after Palmer (1909) had discovered a mineral with a composition close to pseudorutile ($Fe^{3+}_2Ti^{4+}_3O_9$), which he called "arizonite". Afterwards, much research was conducted in this field; however less agreement was obtained, specifically concerning the terminology and processes involved in the formation of many phases in the whole spectrum of ilmenite alteration.

Frost et al. (1983), have adopted Ti/(Ti+Fe) ratios as a basis for classification of ilmenite alteration products and grouped the phases as: primary/unaltered ilmenite, hydrated ilmenite and pseudorutile. Other attempts using Fe/Ti ratios were made by Dillon and Franke (2009), and Franke et al. (2007). Their classification has proven to be effective for the identification of series in the system FeO-Fe_2O_3-TiO2 (Fig. 15).

Recently, Grey and Li (2003) have identified another phase which they called 'hydroxylian pseudorutile' and used XRD to confirm its structure.

In this manuscript the foregoing nomenclature will be used, and a brief description is given below:

- Primary Ilmenite = refers to unaltered grains, with composition close to the stoichiometry defined by the formula $FeTiO_3$, where TiO_2 content varies in between 48 and 53 wt. %, and the ratio Ti/(Ti+Fe) < 0.5.

- Hydrated ilmenite = this term is applied to describe ilmenite grains containing crystalline water, TiO_2 contents ranging from 53 to 60 wt. %, and 0.5 ≤ Ti/(Ti+Fe) < 0.6.
- Pseudorutile = a hexagonal oxyhydroxide phase from a solid solution in between one end-member with a formula close to $Fe^{3+}{}_2Ti^{4+}{}_3O_9$ (41 wt. % TiO_2) and other $Fe^{3+}{}_{1.5}Ti_3O_{7.5}(OH)_{1.5}$, with TiO_2 ranging from 60 to 71 wt. % and 0.6 ≤ Ti/(Ti+Fe) < 0.7.
- Leucoxene = is defined as a microcrystalline aggregate of highly altered ilmenite and rutile. The TiO_2 content is above 71 wt. % and 0.7 ≤ Ti/(Ti+Fe) < 0.9.
- Hydroxylian pseudorutile = is a hydrated iron titanate with non-structural water, having a hexagonal space group $P6_3/mmc$ pseudorutile-like structure. Calculated composition range from $Fe^{3+}Ti_6O_{12}(OH)_3*3H_2O$ and $Fe^{3+}Ti_6O_{11}(OH)_5*2H_2O$. The TiO_2 range about 65 to 78 % and the Ti/(Ti+Fe) between 0.83 to 0.90 (Pownceby, 2010).

- Primary Rutile = used to denominate grains with TiO_2 content ≥90 wt. % and not showing any petrographic evidence of alteration.

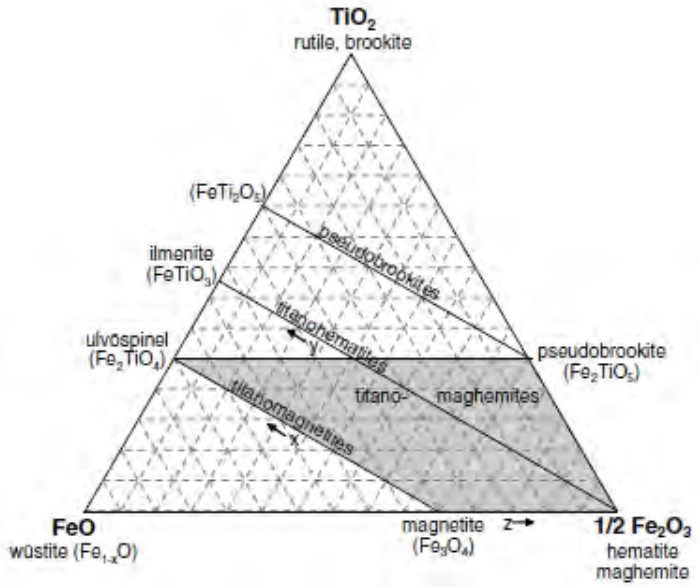

Figure 15. Ternary diagram $FeO\text{-}TiO_2\text{-}Fe_2O_3$ of coexisting phases and solidus-solutions between end-members under low to high temperature conditions. Adapted from Franke et al. (2007).

The ilmenite studied, shows manifold morphologies, textures and association as a result of different stages of alteration that the grains have undergone. This could have occurred at the source rock, and in situ in the deposit. Despite the differences, overall the grains are sub-rounded to rounded, gray to black in colour and exhibiting metallic brightness under reflected light. Most have cracks or pores filled by clay minerals (e.g. kaolinite). Red brown amorphous coating is occasionally seen, but is also extensive to other minerals. Systematic characterization will be made on the basis of observed texture, and further correlated to the genesis.

i. Homogenous textures

Few ilmenites preserve fresh and homogenous surface, suggesting less pervasive or no alteration (Fig. 16a). They are almost pure, not showing associations with other minerals such as hematite or quartz, and have composition close to their theoretical formula, TiO_2 content ranges from 48 to 53 wt. %.

ii. Patchy and porous texture

Aligned tiny voids are characteristic of many ilmenite grains observed (Fig. 16c, d). This pattern is here defined as porous texture, and presumably was due to dissolution and leaching out of thin hematite lamellas or iron removal from the ilmenite structure during the initials stages of alterations. The voids are cut at the grain margins and follow the indentation shown in the grains.

Patches of fine-grained material developing along grain margins, cleavage planes, fractures or other weakness or permeable feature are typical of slightly altered ilmenite grains (Fig. 16d; Fig. 19a) and resemble the amorphous material described by Bailey et al. (1956). In some grains the patches are thin, microporous and less pervasive yielding 2 shades of gray on the grain (Fig. 16e, f). This may result by water percolation along factures, crystallographic planes or weakness areas of the grains, and marks the in situ stage of ilmenite hydration in the deposit.

iii. Intergrowth textures

Many grains exhibit diverse intergrowth textures that are presumed to have evolved at the source rock during the initial crystallization or metamorphic deformation, for instance, randomly arranged small and anhedral rutile crystals forming a vermiform texture in ilmenite (Fig. 17) or

Ti-magnetite grains (Fig. 18a) are common. Other most abundant intergrowth is of ilmenite-rutile (Fig. 18f), although titanomagnetite-rutile has also been found (Fig. 18c), and seldom Ti-magnetite with ilmenite, forming a sandwich-texture (Fig. 18e). The ilmenite-rutile phases intergrown have massive to tabular habit with no preferential orientation. Randomly arranged cracks crosscut indistinctly the phases.

Ilmenite lamellae occur within Ti-magnetite grains (Table 2, row Figure 18a), defining an ex-solution texture. The lamallaes have variegated sizes (Fig. 18a, d), but no intergrowth between them has been noted in this study. The ilmenite lamellae are locally altered to secondary rutile (leucoxene).

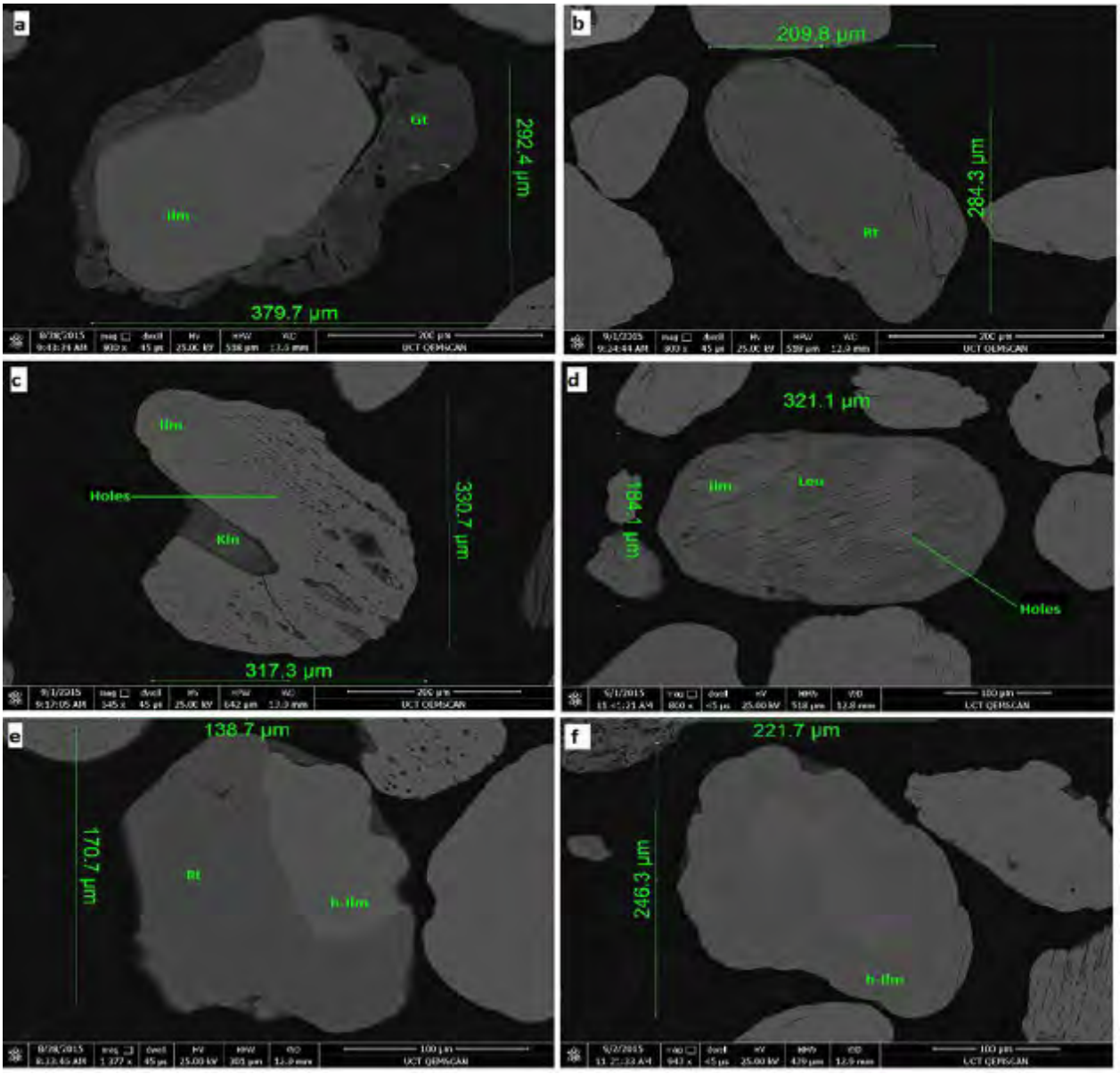

Figure 16. QEMSCAN back-scattered electron images. a) Fresh and homogeneous ilmenite grain surrounded by goethite. b) Primary fresh rutile. c) Patchy ilmenite marked by hematite leached out holes/voids. d) Patchy ilmenite, alteration starting from weakness areas and grain margins. e) Hydrated ilmenite intergrowth with primary rutile. f) Hydrated ilmenite with small ilmenite remnants. Key: Ilm – ilmenite; Gt – goethite; Leu – leucoxene; h-Ilm – hydrated ilmenite; Rt – rutile; Kln – kaolinite.

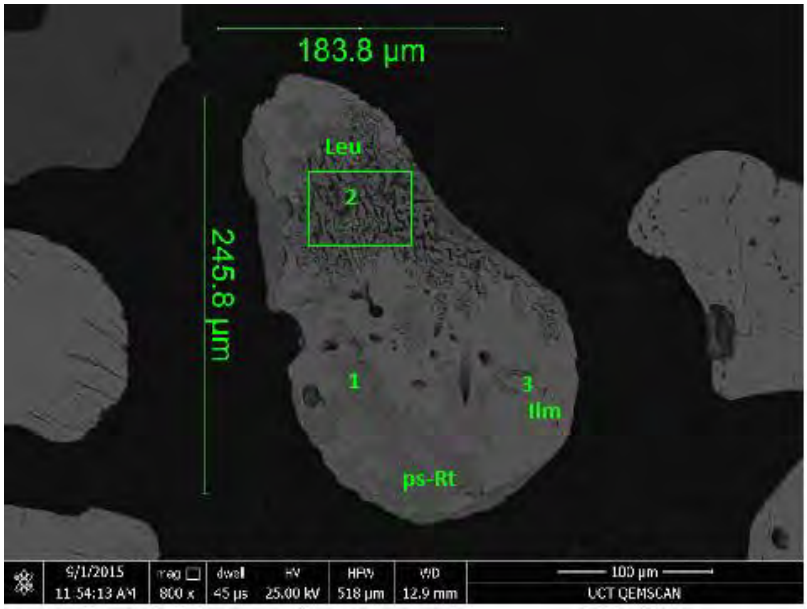

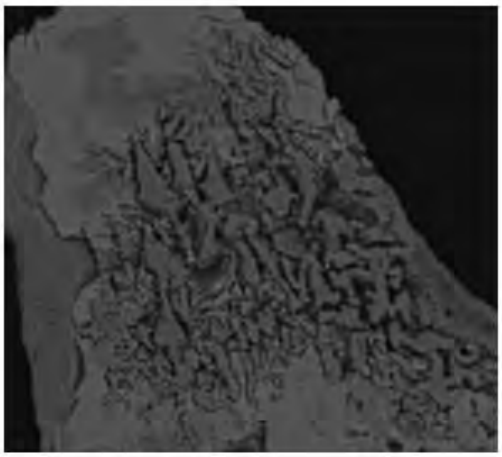

Figure 17. Ilmenite backscatter electron image. The green rectangular shows where the zoomed image (right side) was taken from and the numbers are the locations where spot analyses were performed. The right image illustrates the vermiform-like texture of rutile microcrystals.

Table 2. QEMSCAN spot analyses conducted on individual grains presented on Figures 17, 18 and 19. Low totals are ascribed to coarse porosity and water, characteristic of highly altered spots. Careful reading of the TiO_2 and FeO can lead to identification of diverse Ti-bearing minerals.

Reference	Spot Nr	Al_2O_3	SiO_2	K_2O	TiO_2	MnO_2	FeO	MoO_3	BaO	Fe/Ti*	Total
Figure 17	1	0	0		69	0	22	2	0	0.41	92
	2	13	15		50	0	19	0	0		96
	3	0	0		56	8	36	0	0		100
Figure 18a	1	0	0		70	0	24	0	0	0.45	94
	2	0	0		57	3	40	0	0		100
	3	3	3		87	0	2	0	0		95
	4	0	0		14	0	82	0	4	7.5	100
Figure 18b	1	0	0		67	0	27	0	0	0.52	94
	2	0	0		93	0	0	0	0		93
Figure 18c	1	0	0		92	0	2	0	0		94
	2	0	0		6	0	94	0	0		100
Figure 18d	1	0	0		49	0	51	0	0		100
	2	0	0		55	0	45	0	0		100
	3	0	0		14	0	82	0	4	7.42	100
Figure 18e	1	0	0		15	0	81	0	5		100
	2	0	0		55	0	45	0	0		100
	3	0	0		17	0	79	0	4		100
Figure 22a	1	5	4	2	78	0	11	0	0	0.18	100
	2	0	0		56	6	38	0	0		100
	3	0	0		57	8	35	0	0		100

*Ratios from QEMSCAN's SIP (species identification protocol).

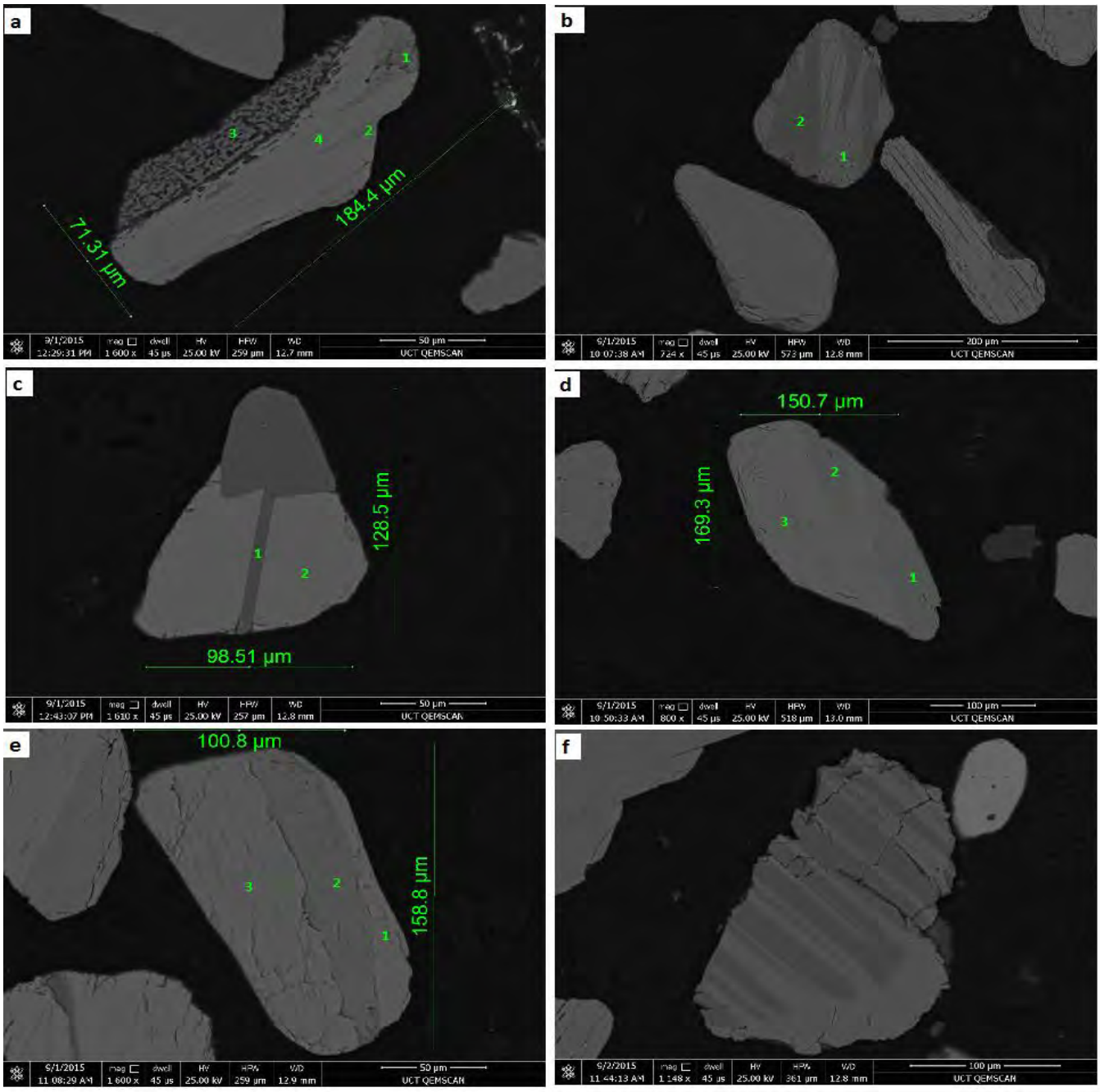

Figure 18. Plate of back-scatter electron images. Phases with more iron have lighter gray tones. a) Ti-magnetite (lighter gray mass - 4) grain with ilmenite lamellae (2), vermiform rutile (3) and pseudorutile (1). b) Ilmenite grain (top-right corner) moderately altered to pseudorutile (1) with rutile intergrowth. c) Titanomagnetite-rutile intergrowt.h, note the difference on the gray tone. d) Titanomagnetite grain (3) with almost primary ilmenite (1 and 2). e) Sandwich-texture. Ilmenite strip (2) within Ti-magnetite grain (1 and 3). f) Rutile-ilmenite intergrowth, dark gray shade stands for rutile and the lighter for ilmenite.

Oxidation and leaching of iron during diagenetic alteration of ilmenite lead to apparent enrichment of Mg, Mn and Cr (e.g. Pownceby, 2010), and Al and Si increase through impurities incorporated into pores (Frost et al., 1983).

In this research 248, 160 and 32 assays were obtained by mean of QEMSCAN, EMP and XRF. The results range from 40.42 to 99.36 wt. % for TiO_2 in particle analyses, and between 44.61 and 55.78 wt. % in bulk analyses. In both particle analysis techniques, the Fe is given as iron total and attempts to recalculate Fe^{3+} and Fe^{2+} yielded non-reliable results. Wet chemistry (Appendix B) performed on 16 combined bulk samples, shows 2 times magnitude oxidation of Fe^{2+} to Fe^{3+}. Scatter plots of the results reveal that the Nataka Deposit consists of ilmenite that has undergone high/advanced alteration stages, therefore yielded different products, that are herein grouped in four classes (Fig. 19a), standing for unaltered to slightly altered ilmenite (**i**), hydrated ilmenite (**ii**), pseudorutile (**iii**) and leucoxene (**iv**) (Table 3). The fifth cluster groups primary rutile that was allowed in the data to assess the impurities of secondary rutile (leucoxene) in comparison with primary rutile. The hydrated ilmenite cluster plots a bit below the linear trend of ilmenite alteration due to low iron, caused by the coarse porosity of the grains.

Another striking variation is observed on the plot of MnO vs. TiO_2. The Mn is higher in grains with between 60 to 65 wt. % TiO_2 and slight depletion towards the right hand side (Fig. 19b). Magnesium in contrast does not show a clear trend (Fig. 19c).

The MnO vs. MgO scatter suggests two distinct ilmenites groups within the population, one with low Mg and high Mn, and the other with high magnesium and low manganese (Fig. 19d). This fact enlightens the possibility of ilmenites sourced from parental rocks with different chemistry.

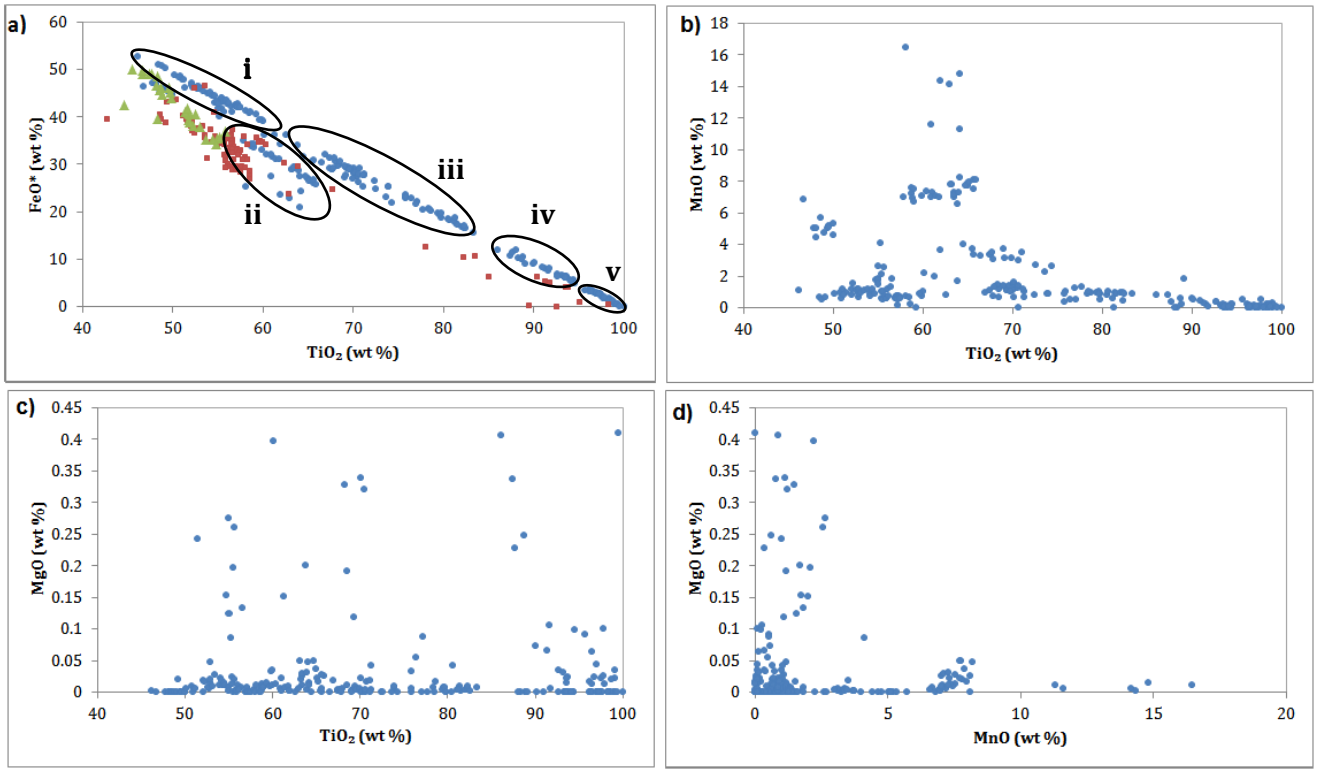

Figure 19. X-Y scatter plots. a, b) Distinct ilmenite alteration product grouped in 4 clases: unaltered ilmenite (i), hydrated ilmenite (ii), pseudorutile (iii) and leucoxene (iv). FeO and TiO_2 normalized by multiplying 100/(100 – K * (Al_2O_3 + SiO_2)); where K is FeO or TiO_2. c, d, e) Mn and Mg deportment with TiO_2 increase. FeO* - total iron; blue dots = 248 analyses from QEMSCAN; red squares = 160 analyses from EMP; green triangles = 32 XRF bulk.

The level of Al, Si and Cr impurities throughout the whole ilmenite alteration spectrum is also well depicted in the plots. The Al_2O_3+SiO_2 against TiO_2 (Fig. 20a) shows an increment on the number of grains with high Al and Si with progressive alterarion of ilmenite. The minimum values are recorded on the field of unaltered ilmenite and the maximum at the leucoxene.

For Cr impurities the same trend is not clearly observed. Some high values on unaltered ilmenite may be due to Fe-Cr solid solution, and maybe the values at the leucoxene field can be ascribed to enrichment as a result of advanced leaching of Fe.

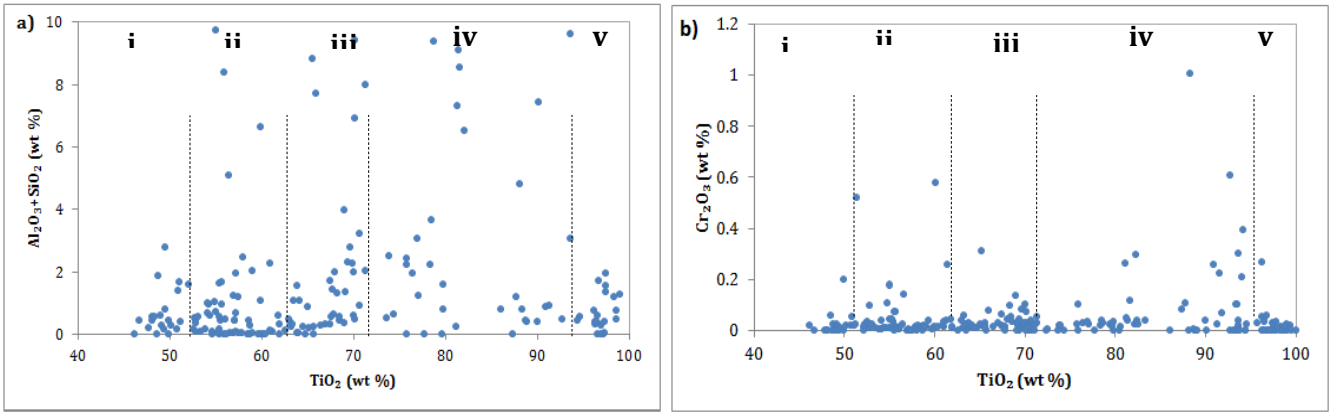

Figure 20. Scatter plots for common ilmenite alteration impurities. Unaltered ilmenite (i), hydrated ilmenite (ii), pseudorutile (iii), leucoxene (iv), and rutile (v). N=248 from QEMSCAN.

Table 3. Selected EMP analyses. The colours in the first column were used to show different Fe-Ti minerals based on the ratios.

Sample ID	NiO	Al_2O_3	TiO_2	FeOt	Cr_2O_3	MgO	MnO	Total	Ti/(Ti+Fe)
N573_45	0.00	0.02	53.49	46.58	0.26	0.03	0.03	100.41	0.53
N439_66	0.00	0.04	50.35	43.71	0.01	0.02	1.36	95.48	0.54
N490_36	0.00	0.01	48.54	40.53	0.02	0.08	7.89	97.07	0.54
N490_36	0.00	0.01	48.72	39.52	0.00	0.11	9.28	97.65	0.55
N490_36	0.00	0.02	49.21	38.84	0.01	0.07	9.10	97.24	0.56
N672_15	0.00	0.29	51.17	40.34	0.00	1.11	0.50	93.41	0.56
N672_15	0.03	0.35	51.54	39.63	0.01	1.20	0.44	93.21	0.57
D303_18	0.00	0.02	51.81	39.12	0.00	0.13	3.60	94.69	0.57
N439_66	0.00	0.09	51.67	38.79	0.00	0.09	1.51	92.15	0.57
N490_36	0.01	0.13	51.67	38.79	0.06	0.06	3.65	94.37	0.57
D177_16	0.00	0.19	55.39	34.70	0.07	0.19	1.21	91.76	0.61
N639_12	0.00	0.22	59.69	34.98	0.10	0.34	0.48	95.81	0.63
D201_21	0.00	0.23	56.10	32.85	0.04	0.17	0.73	90.12	0.63
N639_12	0.00	0.25	59.57	34.79	0.08	0.28	0.44	95.39	0.63
D201_21	0.00	0.80	53.78	31.30	0.34	0.03	5.65	91.90	0.63
N415_6	0.02	0.21	57.09	33.17	0.20	0.21	0.34	91.23	0.63
N639_12	0.00	0.23	59.96	34.78	0.10	0.28	0.40	95.75	0.63
N415_6	0.00	0.21	57.09	33.00	0.24	0.16	0.41	91.11	0.63
D177_16	0.06	0.15	56.31	32.48	0.03	0.00	3.82	92.85	0.63
N639_42	0.00	1.01	55.64	31.97	0.02	0.06	3.07	91.78	0.64
N415_6	0.00	0.20	56.60	32.51	0.18	0.25	0.49	90.23	0.64
D201_21	0.00	0.38	62.79	23.92	0.33	0.01	6.06	93.49	0.72
N639_42	0.01	0.68	67.66	24.86	0.04	0.05	1.58	94.89	0.73
N639_42	0.00	0.00	67.66	24.86	0.03	0.25	1.19	94.00	0.73
D177_10	0.00	0.34	77.95	12.53	0.24	0.03	0.18	91.27	0.86
D177_10	0.03	0.16	83.43	10.68	0.49	0.04	0.16	95.00	0.89
D177_10	0.01	0.87	82.25	10.39	2.10	0.03	0.15	95.80	0.89
D175_8	0.00	0.15	85.00	6.46	0.03	0.04	0.05	91.72	0.93
D175_8	0.00	0.04	90.41	6.40	0.05	0.19	0.05	97.14	0.93
N490_36	0.00	0.02	91.28	5.43	0.02	0.01	0.06	96.82	0.94
D175_8	0.00	0.02	91.76	5.24	0.00	0.13	0.06	97.20	0.95
D175_8	0.00	0.05	93.54	4.13	0.01	0.11	0.06	97.91	0.96
D177_16	0.01	0.03	93.81	4.08	0.29	0.09	0.41	98.71	0.96
D177_10	0.00	0.22	95.07	0.93	0.00	0.00	0.02	96.24	0.99
N569_11	0.00	0.34	98.32	0.50	0.04	0.39	0.92	100.51	0.99
N415_11	0.01	1.52	89.45	0.25	0.10	0.85	2.72	94.90	1.00
N573_11	0.07	0.78	92.59	0.10	0.00	0.42	1.81	95.76	1.00

Note: Same grains were analysed at different spots. Totals are low maybe due to coarse porosity, incorporated water, and Fe oxidation to its ferric state.

4.1.2.1. Ilmenite impurities

The economic value of ilmenite concentrates is intrinsically related to the presence of other phases in the deposit plus the nature and level of impurities in the ilmenite. The Nataka ilmenite concentrate comprises chromite (Cr-spinel), and intra-porous Cr, Al and Si impurities. The Al+Si impurities occur in two modalities, as follow: intra-porous and filling/coating amorphous clays (Fig. 16a and Fig. 21). The intra-porous impurities of Al+Si as demonstrated in Figure 20a, are related to diagenetic alteration of ilmenite, therefore their removal requires laborious and expensive technologies, such as sodium hydroxide leaching. Amorphous coatings of clay formed by superficial precipitation of iron in Al+Si rich environments can easily be washed out using an acid solution or employing light attritioning.

Ilmenite grains with intra-porous Cr impurities concentrations exceeding 0.3 wt. % has reduced market value as a potential feedstock for TiO_2 production (Pownceby, 2005). In the Nataka deposit intra-porous Cr impurity level is negligible (Fig. 20b). Chromite makes up 2.4 % modal abundance of the ore (Fig. 12) and occurs as discrete grains (Fig. 21), therefore enabling easy separation from the concentrate using a low magnetizing roast treatment (Fisher-white et al., 2007).

In summary, the Nataka deposit concentrates have low concentrations of Al+Si impurities, given the low pseudorutile-leucoxene modal abundance (3.32 wt. %), and easily removable chromite impurities relative to coeval deposits worldwide, which have high modal abundances of pseudorutile (e.g. Eucla Basin deposits, South Australia, holding more than 60 wt. % of Ti -rich minerals (Pownceby et al., 2008) and a wide range of spinel composition types (Pownceby, 2005), making their removal problematic (e.g. Murray Basin, southeastern Australia).

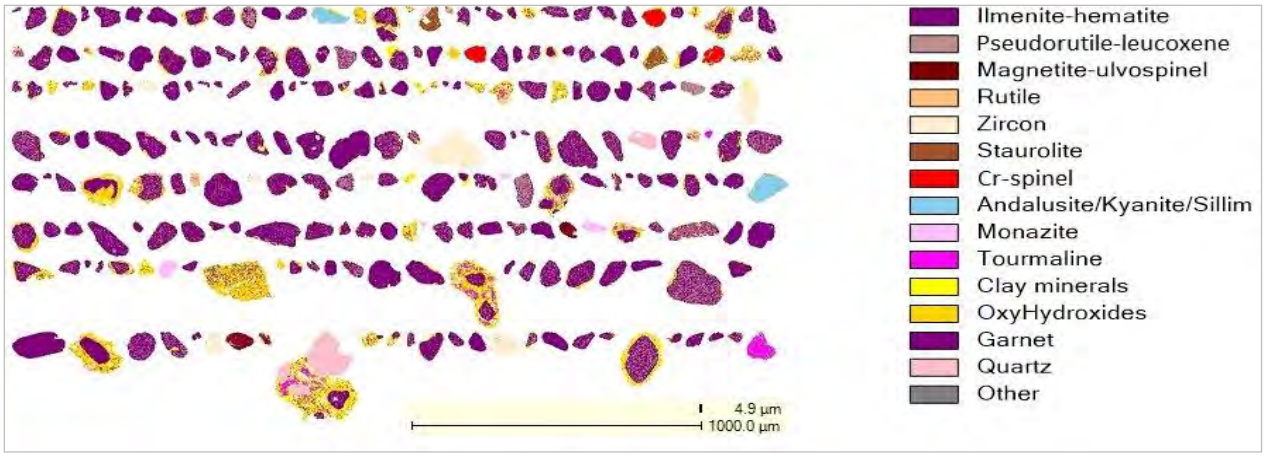

Figure 21. Particle mineral analysis (PMA) false colours image of Nataka concentrates. Cr-spinel generally found as discrete grains (red colour) in the Nataka heavy mineral concentrates.

4.1.3. DISCUSSION

The results presented in the previous section provide evidence that the ilmenite grains in the Nataka deposit have evolved in different environments, and the ilmenite was subjected to diverse types and mechanisms of alterations.

The first type (I) of alteration occurred in the source area, and resulted in diverse Fe-Ti bearing minerals intergrowths. The Type I resulted in oxy-exsolution lamellae textures formed by ilmenite in magnetite by hydrothermal oxidation of ulvospinel upon cooling of the magma (Buddington & Lindsley, 1964; Lattard et al., 2005); and sub-graphic textures of titanomagnetite-rutile (Fig. 18c) and ilmenite-rutile (Fig. 18a, 18e) during eutectic crystallization (Edwards,1965; Ramdohr, 1969). Recognized solidus solutions of ilmenite-hematite series with pseudobrookite-ferropseudobrookite series above 1199.85 ^{o}C (Pownceby & Fisher-White, 1999; Lattard et al., 2005), followed by decomposition at temperature below 1099.85 ^{o}C to ilmenite + rutile may have taken place, and some grains originated from the foregoing mechanism probably mimicked the parental-pseudobookite structure, thereafter the latter being identified by XRD spectroscopy study. In addition, a vermiform texture of rutile in titanomagnetite or ilmenite (Fig. 17, 18a) was observed, and ascribed to diffusion controlled growth (Roeder et al., 2001) of rutile crystals during partial melt in metamorphic events.

During the oxidation stage near surface in Type I alteration, Fe might have been removed from ilmenite grains leaving voids (Fig. 16c, 16d). This observation is supported by a good match of the voids with grain indentations and also agrees with the findings of Babu et al. (1994), which in their study of the Manavalakurichi ilmenite concluded that the ferrous iron oxidation is advanced compared to the ferrous iron removal. Hugo and Cornell (1991), however identified the same fact, but they did not take it as an essential step of ilmenite alteration.

After the Type I alteration, weathering and alteration took place on the sediments, either along the transportation or after deposition. Available petrographic data do not yield clear evidence for a time frame; however, it is believed that alteration during transportation was negligible. In the deposition place, two different environments may have prevailed and been responsible for types II and III of ilmenite alteration.

Type II alteration was long described by other authors (e.g. Bailey et al., 1959; Frost et al., 1983), and was similarly observed in the Nataka deposit. This type of alteration is assumed to be continuous, and happen in 3 stages: The first starts with hydration, oxidation and progressive Fe removal from the structure to form amorphous material along the grain margins or weakness parts. In favouring conditions, water can be incorporate in the ilmenite structure resulting in a hydrated mineral. Whether hydrated ilmenite is formed or not, the previous stage continues to stage 2, where all the ferrous iron has been oxidized to ferric state and one third of it removed to form the hexagonal structure of pseudorutile according to the equation [3] of Grey and Reid (1975). The third stage occurs with the removal of 95 % of the Fe and simultaneous removal of oxygen from the structure to produce micro-crystalline leucoxene (Equation 4).

$$3Fe^{2+}TiO_3 + \frac{3}{4}O_2 + \frac{3}{2}H_2O \rightarrow Fe_2^{3+}Ti_3O_9 + Fe(OH)_3 \qquad [3]$$

$$Fe_2Ti_3O_9 \rightarrow 3TiO_2 + 2Fe^{2+} + 3O^{2-} \qquad [4]$$

The Type III alteration involves direct alteration of ilmenite or slightly altered ilmenite to leucoxene, normally beginning from the grain margins or cracks (Fig. 22c, 22d). The Type III is ascribed to take place in a different environment compared to Type II.

Available alteration models cite two different environments as favourable for ilmenite alteration by chemical weathering (e.g. Grey & Reid, 1975; Frost et al., 1986). The models postulate that the stage 1 and 2, of Type II alteration takes place gradually, below water table, in oxidizing and mildly acidic to acidic-neutral conditions (Weibel, 1998; Van Houten, 1973), where groundwater plays an important role for the hydration and oxidation of iron. This results in pseudorutile as final phase according to Equation [3] at the second stage.

The third stage of alteration in Type II, takes place in acidic and reducting conditions, prevailing near top surface of the deposit. These conditions are found more conducive to cause in pseudorutile simultaneous dissolution of Fe and Ti, and posterior precipitation of TiO_2 as leucoxene and Fe_2O_3 leached out, as per Equation [4] (Grey & Reid, 1975). Meanwhile, this explains well the simultaneous occurrence of pseudorutile and leucoxene in the same deposit, as observed in this study, however does not give a plausible explanation for concomitant presence of pseudorutile and leucoxene in the same grain (Fig. 22a, 22b), and natural conditions for the formation of hydrated ilmenite. Frost et al. (1983), while not providing an alternative model, are among the authors that suggest that the Grey and Reid (1975) model should be reviewed, and mechanism of hydration and hydroxylization included. Grey and Li (2003) and Pownceby (2010) have unfruitfully tried to explain the hydroxylization mechanism and, so far, no further work has been published.

Despite the misgiving reviewed above, this model has been validated by other workers, due to ascertaining vertical TiO_2 enrichment in the top meters of the deposits (e.g. Temple, 1966). In this study no vertical gradation of TiO_2 was observed (Fig. 11). In addition, the roughly uniform red colour of the deposit means that any portion of the deposit has been bleached, producing drab patches/layers (Weibel, 1998). Thus, based on the models aforementioned and the results obtained from this study, the Nataka deposit genesis is hereafter tentatively reconstructed.

The Nataka deposit might have evolved in a hot and humid climate (e.g. Woltering et al., 2011; Holmgren et al., 2003) that prevailed during the Pleistocene, favoured by sea level fluctuations and high sediment supply from the hinterland. Its reddening may have developed with in situ dissolution of unstable iron-bearing silicates, and precipitation of goethite and hematite (Weibel, 1998) resulting from Type I alteration. The iron removals that happen in Type I, may have worked

as a mechanism for ilmenite hydration. The hydration was interrupted due to volume reduction of the ilmenite structure, thus inhibiting the incorporation of water, thereby giving room to the formation of pseudorutile.

The ilmenite alteration occurred in situ, and the first two stages of Type II took place when the deposit was wholly submerged in water, under oxidizing and mildly acidic conditions. The Eh and Ph may have varied through the alteration process causing simultaneous occurrence of ilmenite, pseudorutile and leucoxene.

The third stage, in contrast to the available model (Grey & Reid, 1975), probably developed randomly within the deposit due to localized reducing conditions developed during decomposition of organic matter, which were deposited together with detritus sediments, and their decomposition was stimulated by sediments exposure to sun (Frost et al., 1986), during regression periods. In a similar way, direct alteration of ilmenite to rutile/leucoxene (Type III) may also be explained by decomposition of organic matter, to produce humic acids that interact with fresh/slightly altered ilmenite grains dissolving the mineral and leaching the iron, and titanium precipitated (Hugo and Cornell, 1991) according to the equation:

$$FeTiO_3 + 2H^+ \rightarrow TiO_2 + Fe^{2+} + H_2O \qquad [5]$$

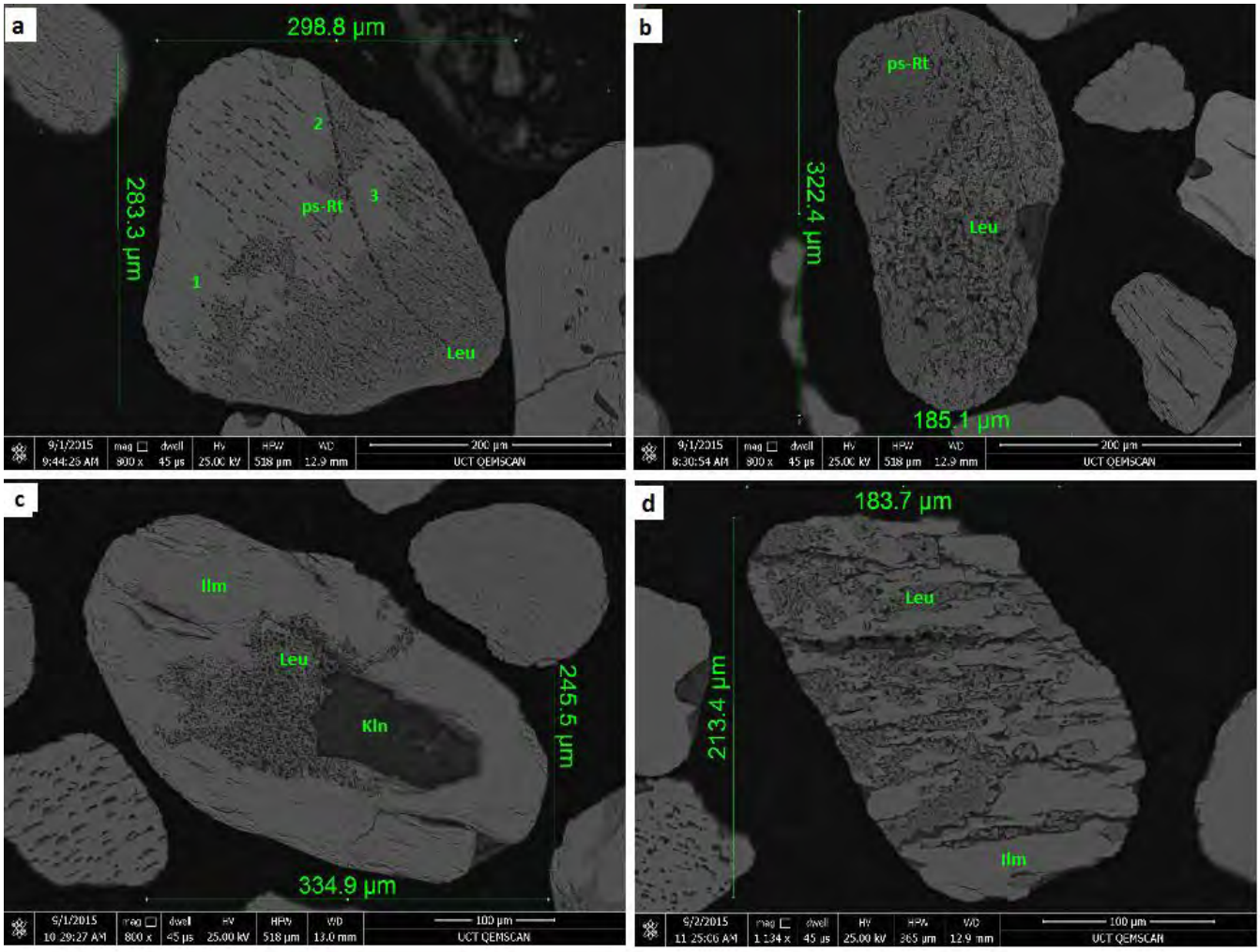

Figure 22. a,b) Grains with concomitant occurrence of slight altered ilmenite, pseudorutile and leucoxene. c,d) Fresh to slightly altered ilmenite grain directly altered to leucoxene. key: Ilm – ilmenite; Kln – kaolinite; ps-Rt – pseudorutile; Leu – leucoxene.

4.1.3.1. Ilmenite chemistry and its significance for parental rock identification

The elements Mn, Mg, Cr and V are common constituents of iron-bearing oxides, due to their similarity of charge and size that allows them to substitute for Fe^{2+}. In the Nataka deposit Cr and V concentrations are very low; Mn shows a correlation with titanium, where it increases up to about 65 wt. % Ti and a gradual depletion towards 100 wt. % (Fig. 19b). The correlation between Mn and Ti is explained by relatively low oxidation potentials (Frost et al., 1986) compared to Fe, then being enriched during the Type I and II (stage 1 and 2) alteration, where Fe is partial removed. With the progression of alteration, Mn also reaches its trivalent oxidation state and is together

leached out with iron from the ilmenite structure. In contrast, magnesium does not have a clear correlation with alteration of ilmenite, therefore the random relatively high Mg observed (Fig. 19d) may be ascribed to limited enrichment during ilmenite alteration, as the values are too low to assume the presence of geikelite ($MgTiO_3$).

The MnO vs. MgO plot also shows the existence of two different domains: one Mn-rich (low Mg) considered typical of peraluminous granites and metapelites; and other Mg-rich (low Mn) that tend to be of mafic igneous rock (Pownceby et al. 2008).

A parallel test (Table 4) to track the parental rock was also conducted based on Buddington and Lindsley (1964) ratio intervals of Mn in ilmenite and coexisting Mn in titanomagnetite, which define:

- 1.4 – 5; for dolerite, gabbro, and anorthosites;
- 5 – 5.5; for quartz-bearing syenites and granites;
- 5.5 – 15; for high-grade metamorphic rocks and pegmatite granite.

The test based on Buddington and Lindsley (1964) reveals a full agreement with the findings of Pownceby et al. 2008, in that the ilmenite may have had mafic igneous precursors (dolerite, gabbro and anorthosites – light gray in Table 4) and granite rocks (dark gray ratios in Table 4) as parental rocks.

Table 4. Representative QEMSCAN assays used to calculate the ratio of Mn in ilmenite and coexisting Mn in titanomagnetite (right edge column). The gray tones were used to mark different ranges. Values sorted using final column.

Sample ID	NiO	Al_2O_3	SiO_2	TiO_2	FeO	Cr_2O_3	MgO	MnO_2		NiO	Al_2O_3	SiO_2	TiO_2	FeO	Cr_2O_3	MgO	MnO_2		
	Magnetite-ulvospinel									Ilmenite-hematite									il-Mn/Mgt-Mn
D303_18	0	0	0	23	73	0	0	1		0	0	1	47	37	0	0	1		1
D305_15	0	1	1	35	58	0	0	0		0	1	1	68	20	0	0	0		1
D305_8	0	2	2	28	63	0	0	1		0	0	0	52	37	0	0	1		1
D157_6	0	0	0	36	59	0	0	1		0	0	0	66	27	0	0	1		1
D305_15	0	0	0	35	62	0	0	0		0	0	0	44	38	0	0	1		2
N672_15	0	0	0	18	79	0	0	0		0	0	0	17	74	0	0	0		2
D201_21	0	1	1	29	65	0	0	0		0	0	0	56	40	0	0	1		2
N569_11	0	0	0	22	74	0	0	0		0	0	0	17	74	0	0	0		2
D177_6	0	1	1	29	63	0	0	0		0	0	1	47	38	0	0	1		2
D303_7	0	0	0	21	74	0	0	0		0	0	0	56	41	0	0	1		2
N439_66	0	0	0	30	66	0	0	0		0	3	5	48	21	0	0	1		2
D130_10	0	0	0	37	59	0	0	1		0	0	0	50	39	0	0	2		2
N613_37	0	0	0	32	63	0	0	0		0	0	0	49	47	0	0	1		2
N415_6	0	4	3	32	53	0	0	1		0	3	3	50	22	0	0	1		2
D305_8	0	2	1	25	66	0	0	1		0	6	7	38	29	0	0	1		2
D177_10	0	0	0	14	83	0	0	0		0	0	0	57	40	0	0	0		3
N613_37	0	0	0	31	65	0	0	0		0	0	0	45	38	0	0	1		3
D141_7	0	0	0	28	68	0	0	0		0	0	0	49	46	0	0	1		3
D157_32	0	0	0	18	79	0	0	0		0	0	0	52	41	0	0	1		3
N613_37	0	0	0	28	68	0	0	0		0	0	0	45	38	0	0	1		3
N573_11	0	0	0	20	77	0	0	0		0	0	0	56	41	0	0	1		6
N439_11	0	0	0	22	75	0	0	0		0	0	0	45	40	0	0	1		6
N569_11	0	0	0	23	73	0	0	0		0	0	0	51	44	0	0	1		6
N639_12	0	0	0	34	62	0	0	1		0	0	0	67	24	0	0	3		6
D130_35	0	0	0	31	65	0	0	1		0	0	0	61	30	0	0	4		6
D130_10	0	0	0	31	65	0	0	1		0	0	0	59	33	0	0	4		7
N573_11	0	0	0	20	76	0	0	0		0	0	0	52	41	0	0	1		7
D201_21	0	0	1	26	70	0	0	0		0	5	5	42	33	0	0	2		7
D201_9	0	0	0	13	82	0	0	0		0	0	0	72	0	0	0	1		7
D177_6	0	1	1	28	65	0	0	1		0	0	0	48	45	0	0	5		7
D157_32	0	0	0	19	78	0	0	0		0	0	0	56	41	0	0	1		7
N569_49	0	0	0	19	77	0	0	0		0	0	0	46	38	0	0	1		8
D305_8	0	1	1	28	65	0	0	0		0	0	1	62	29	0	0	1		8
D141_7	0	0	0	27	70	0	0	0		0	3	4	43	31	0	0	3		8
N573_11	0	0	0	21	76	0	0	0		0	0	0	69	27	0	0	1		12
N613_13	0	0	0	24	72	0	0	0		0	0	1	46	36	0	0	1		12
N672_41	0	0	0	21	75	0	0	0		0	0	0	68	29	0	0	1		13
N439_66	0	0	0	24	72	0	0	0		0	0	0	67	25	0	0	3		14
N639_42	0	0	0	18	78	0	0	0		0	0	0	67	27	0	0	2		14
D305_8	0	1	1	26	66	0	0	1		0	0	0	57	21	0	0	13		14
N639_12	0	0	0	14	83	0	0	0		0	1	1	64	25	0	0	1		15

4.2. PROVENANCE APPROACH

Determination of sediments source have been for long time solely based on heavy mineral assemblage analysis. However, this proxy is biased, as minerals have different stability (Pettijohn, 1941; Morton, 1984) during processes in the sedimentary cycle such as hydrodynamic fractionation and burial diagenesis (Morton & Hallsworth, 1999; Morton et al., 2005). These processes affect and control the mineral assemblages during transportation and, ultimately, at the place of deposition. To circumvent the effects of the aforementioned processes, ratios of hydrodynamic and diagenetic equivalent minerals have been recommended (Morton & Hallsworth, 1999; Hallsworth & Chisholm, 2008). Furthermore, with the availability of single grain analytical techniques, such as EMPA, mineral assemblage analysis can be fruitfully combined with grain morphology (e.g. Tsikouras et al., 2011), and varietal studies of single-mineral or mineral group, like Fe-Ti phases (e.g. Basu & Molinaroli, 1991), magnetite (e.g. Yang et al., 2009), garnet (e.g. Morton, 1985), tourmaline (e.g. Henry & Guidotti, 1985; Li at al., 2015) and rutile (e.g. Zack et al., 2002; Meinhold, 2010; Triebold et al. 2012).

4.2.1. VARIETAL STUDIES

A few years after the detailed study of mineral stability (Pettijohn, 1941), provenance studies were focused on optical varietal studies (e.g. colour, morphology) of the stable minerals. Nevertheless the improvement, the method was still subjective by being user-dependent and due to different physical propriety being obtained by many combinations of mineral end-members in different proportion or the presence of an inclusion.

Therefore, with the forthcoming rapid quantitative individual particle analysis techniques, varietal studies for sediments provenance have been revitalized. Consequently, much research into sediment provenance was conducted, being garnet and tourmaline the most employed, given their wide range in composition and correlation with the source rock.

In detrital mineral provenance studies, representative geological rocks types is essential, to avoid biased sources, due to different rock fertility in a certain phase [rock fertility is the propensity of source-rock to yield a certain detrital mineral when subjected to erosion - (Dickinson, 2008)]. For this thesis, 6 minerals were selected, of which three are common in igneous mafic rocks (ilmenite,

magnetite and Cr-spinel), one in igneous felsic rocks (zircon) and the other two typical of metamorphic environments (tourmaline and rutile).

4.2.1.1. Magnetite

Magnetite can form at diverse environments, from high to low hydrothermal temperature (Dare et al., 2012), with distinct trace/minor elements.

The petrographic study of magnetite presented in previous sections, outlined the occurrence of titanomagnetite/ulvospinel exsolution. Consequently, magnetite chemical composition shows a wide range of Fe (tot) and Ti spanning from 52.85 to 84.84 wt. % and 32.19 to 10.40 wt. %, respectively. Magnesium, Al, V, Cr and Mn have concentrations dominantly less than 1.0 wt. % and averages around 0.08 to 0.41 wt. % for the latter four elements, and about 0.01 wt. % for Mg. Discriminant diagrams TiO_2+V_2O_5 vs. MgO/(MgO+Al_2O_3) (Yang et al., 2009) and Ni/Cr vs. Ti (Dare et al., 2014), point out mafic plutonic and maybe intermediate volcanic source rock (Fig. 23a). The magmatic genesis is also depicted in Figure 23b, where samples cluster below Ni/Cr < 1.

The mafic plutonic source is also supported by scarce occurrence of homogenous grains, which are typical of felsic plutonic and volcanic parent rocks (Yang et al., 2009), high Ti (Nadoll et al., 2012; Dupuis and Beaudoin, 2011; Nadoll et al., 2014), and magnetite crystallized in a free ilmenite magmas, which enabled Ti to partition into magnetite (Dare et al., 2014).

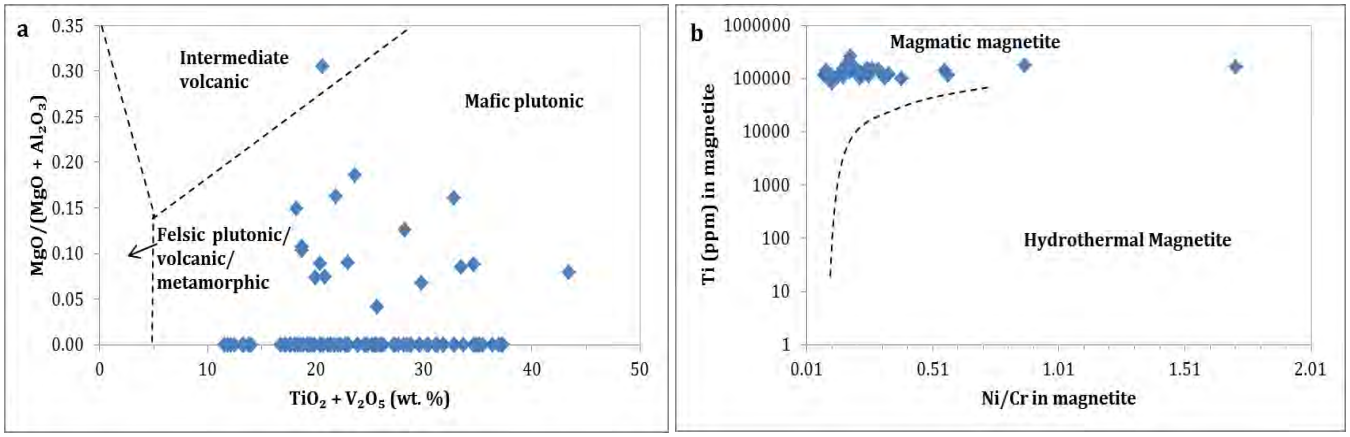

Figure 23. Source rock discriminant diagrams. a) MgO/(MgO + Al_2O_3) vs. TiO_2 + V_2O_5, adapted from Yang et al. (2009). b) Ni/Cr vs. Ti, adapted from Dare et al. (2014). Data form QEMSCAN.

4.2.1.2. Cr-spinel

Cr-spinels are useful petrogenetic indicator, as they crystallize in diverse mafic and ultramafic conditions, and are resistant to alteration over other mafic minerals (Barnes & Roeder, 2001). Their chemistry is commonly used to constrain the nature of mantle peridotite source and degree of partial melting (Kamenetsky et al., 2001), applying Cr-number [Cr# = Cr/ (Cr + Al)] and Mg-number [Mg# = Mg/ (Mg +Fe)] (e.g. Dick & Bullen, 1984; Roeder, 1994). Moreover, Al_2O_3 and TiO_2 can with a certain degree of overlap discriminate mid-ocean ridge basalts (MORB), large igneous province (LIP), ocean-island basalt (OIB) and island-arc magmas (IA), given the lack of change expected during post-entrapment re-equilibration (Kamenetsky et al., 2001).

Cr-spinel chemical compositions from the study area, revealed Type III peridotite parental rock (Fig. 24a) and a Fe-Ti trend (Barnes & Roeder, 2001) in FeO/ (FeO + MgO) versus Cr# in Figure 24b. In the Cr# vs. TiO_2 diagram of Arai (1992), chromite data plot in intra-plate and boninites probably overlapped with island-arc basalt fields (Fig. 24c). Slightly similar results were obtained in Al_2O_3 vs. TiO_2 diagram (Fig. 24d), where IA, MORB and OIB parental sources were identified.

The Type III peridotite in Figure 24a is analogous to arc-related volcanic rocks (Dick & Bullen, 1984). This is in agreement with intra-plate basalt and boninite source depicted in Figure 24c, which have Cr# > 0.6 (Arai, 1992), and OIB and IA in Figure 24d. However, mid-ocean ridge basalts genesis identified in Figure 24d cannot be assertively related to other diagrams, however, Arai (1992) conceive closeness of intra-plate basalts to MORB.

The basaltic petrogenesis is supported by clustering of samples in roughly left and centre in Figure 24b (Roeder, 1994) and average progressive Fe/(Fe + Mg) ratio (Roeder, 1994). The slight downward of Fe/(Fe + Mg) point to a probable basaltic or most differentiated mafic-ultramafic bodies (Barnes & Roeder, 2001). Metamorphic overprint if occurred did not cause significant composition changes, as no top right agglomeration is seen in Figure 24b (Roeder, 1994).

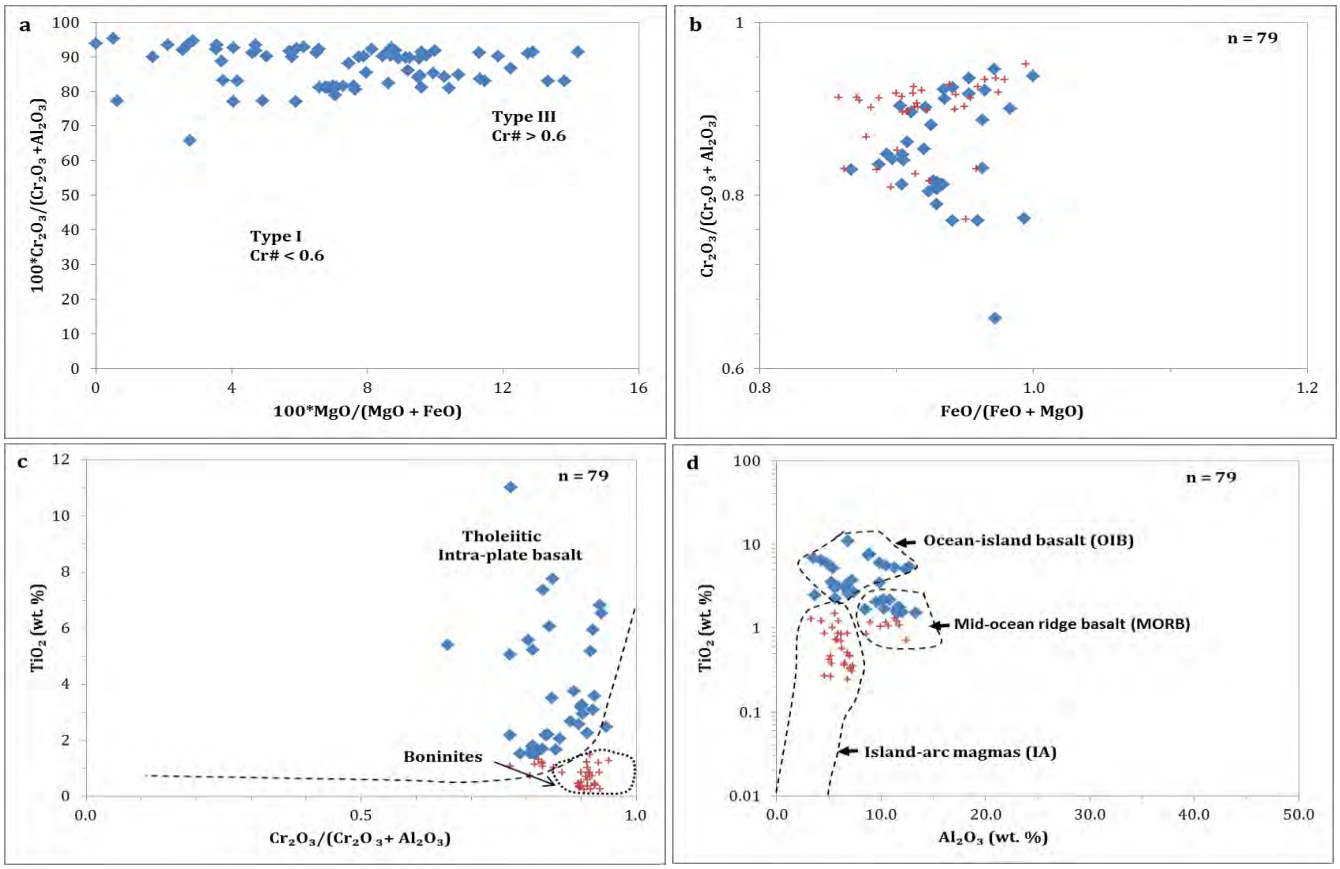

Figure 24. Rock genesis discrimination diagrams using Cr-spinel composition obtained from QEMSCAN. a) Mg# vs. Cr # adapted after Dick and Bullen (1984). b) FeO/(FeO + MgO) vs. Cr# after Roeder (1994). c) Cr# vs. TiO_2 adapted after Arai (1992). d) Al_2O_3 vs. TiO_2 after Kamenetsky et al. (2001). Red plus symbols stand for samples with $TiO_2 < 1.5$; and blue diamond indicate $TiO_2 > 1.5$.

4.2.1.3. Zircon

Zircon is a common phase in detrital assemblages, as it can withstand mechanical and chemical-breakdown over a long time (Hoskin & Ireland, 2000). It has traditionally used for revealing the maximum ages of sediment deposition, and to define the age spectrum of the terrain that might have been the source area. However, this information is only one piece of the sediment source-area puzzle reconstruction, since it does not account for lithological composition (Morton et al. 2005). Its ultra-stability was the impetus for many composition studies, especially in revealing the source of mature sediments, where zircon can be the only one heavy mineral in the assemblage (Hoskin & Schaltegger, 2003).

After the advent of zircon geochemistry for provenance studies, no consensus was reached and debate is still taking place. Some authors have argued that zircon chemistry is less useful than other minerals as a provenance indicator, given that it is only a liquidus phase in felsic and some intermediate melts (Hoskin & Ireland, 2000), REE patterns are variable and do not characterize either igneous or metamorphic environment (Rubatto, 2002). Nevertheless, some element ratios or concentrations, such as Th/U, Zr/Hf, Ce/[(La + Nd)/2], Y [pmm], Nb/Ta and P [ppm] reached reasonable credibility (de Barros et al., 2010), therefore hereafter employed.

Thorium/uranium ratios of 101 analysed zircons span from 0 to 4.24. Based upon El-Naby and Dawood (2014), SiO_2 versus Th/U diagram provide clear distinction between igneous and metamorphic zircon at Th/U = 0.1. Using the aforementioned diagram, the Nataka zircons were found to have igneous genesis (Fig. 25a). Using other classifications, the following grouping can be made: (1) Th/U < 1 and Th/U > 1 are consistent with igneous granitoids and metamorphic source, respectively (de Barros et al., 2010); (2) igneous related zircon have Th/U greater than 0.07 (Rubatto, 2002).

To assess previous classifications, further constrains were made using Yttrium versus U/Yb diagrams (Grimes et al., 2007) (Fig. 25b), scatter plot of Th versus Y (Fig. 25c), U versus Y (Fig. 25e), and Ta versus Nb (Fig. 25f) (Belousova et al., 2002), and similar to previous discrimination, these also pointed out continental granitoids (plagiogranite is a minor component of oceanic crust) as the source material, with contributions dominantly from aplites, leucogranite and granite, and in a few extent from granodiorite and tonalite (Fig. 25e).

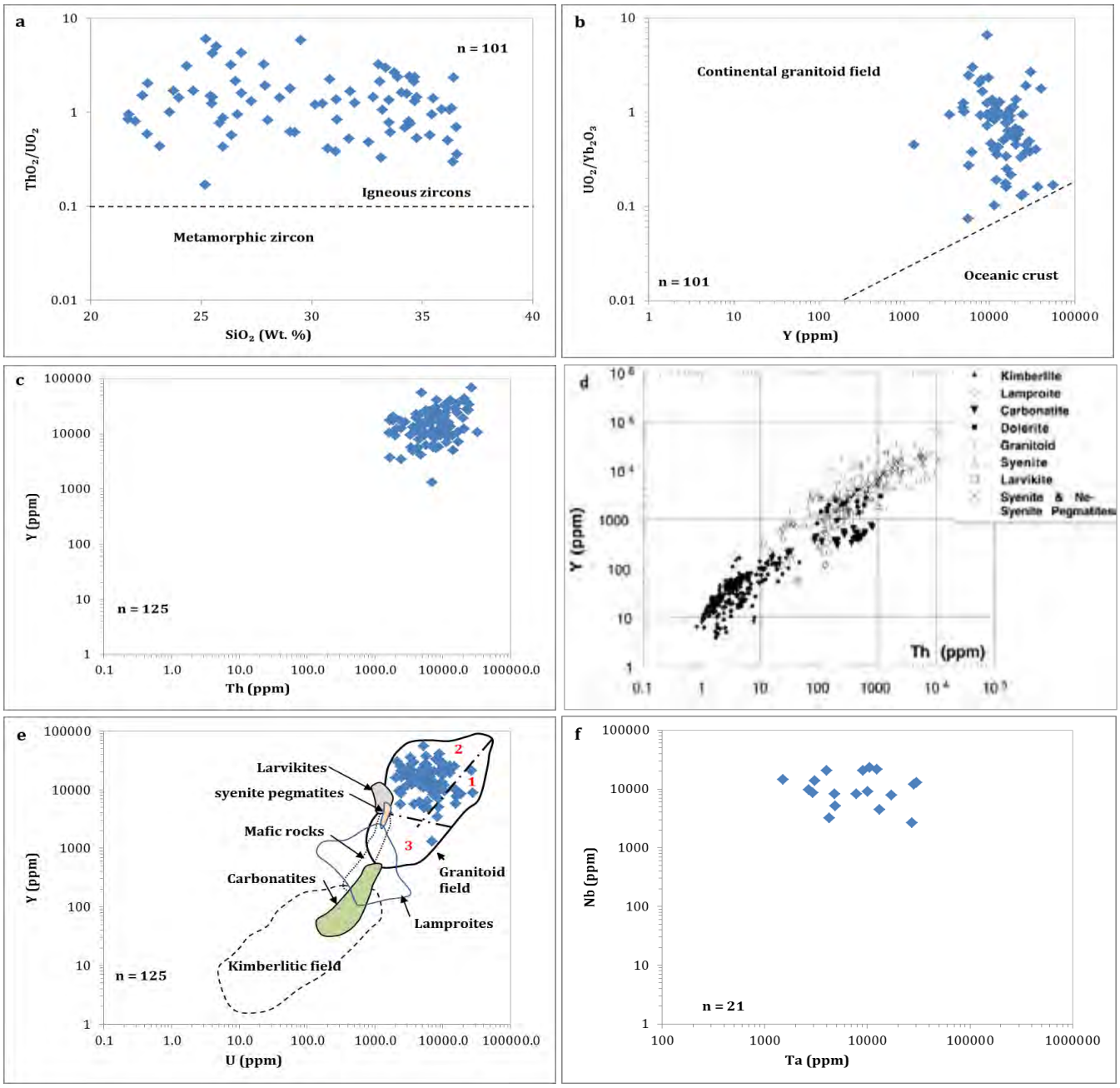

Figure 25. Source discriminant diagrams based upon zircon chemistry obtained from QEMSCAN. A) SiO_2 vs. Th/U adapted after El-Naby and Dawood (2014). B) Y vs. U/Yb modified after Grimes et al. (2007). C) Th vs. Y, adapted after Belousova et al. (2002). D) diagram from Belousova et al. (2002) used for comparison purposes with (c). e,f) U vs. Y and Ta vs. Nb, respectively. Adapted from Belousova et al. (2002). 1 – aplite, leucogranite; 2 – Granite; 3 – granodiorite, tonalite.

4.2.1.4. Tourmaline

Tourmaline is a stable (Morton, 1984) boron-containing silicate with a complex general formula $XY_3Z_6(BO_3)Si_6O_{18}(OH)_4$ (Henry & Guidotti, 1985), likely to occur in greenschist to upper amphibolite facies (Thompson, 2006) metamorphic rocks of diverse compositions, and granitoid rocks. The X and Z positions are usually occupied by Na and Al, respectively, nevertheless Ca and Mg can substitute for Na, and Fe, Ti, Mg, Cr and V replace Al. the Y position can be occupied by monovalent, divalent, trivalent and quadrivalent cations. The wide compositional variation of tourmaline is normally described using the end-members schorl $[Na(Fe^{2+})Al_6(Si_6O_{18})(BO_3)_3(OH)_3(OH)]$ – dravite $[Na(Mg_3)Al_6(Si_6O_{18})(BO_3)_3(OH)_3(OH)]$ and schorl – elbaite $[Na(Li_{1.5}Al_{1.5})Al_6(Si_6O_{18})(BO_3)_3(OH)_3(OH)]$ are commonly used (Henry & Guidotti, 1985).

In spite of the complex tourmaline chemistry, its composition is governed by Al, Ca, Mg and Fe substitutions, and it can be related to bulk sample composition of the host rock, hence the Al - $Fe_{(tot)}$ - Mg and Ca - $Fe_{(tot)}$ – Mg diagram by Henry and Guidotti (1985) is feasible to discriminate parental rocks.

The Nataka tourmalines are dominated by schorl-elbaite and schorl-dravite series (Fig. 26), which characterize granitoid and pegmatite rocks (Von Eynatten & Gaupp, 1999), and regional and contact metamorphic areas (Brocker & Franz, 2000). In a ternary diagram (Fig. 26), the majority data plot in the granitoid pegmatite and associated aplite fields in a broad sense (Fig. 26a field 1,2,3; Fig. 26b, field 1,2), and metapelic and metapsammitic fields (Fig. 26a, fields 4,5,6; Fig 26b, field 3). Minor contribution from Low-Ca meta-ultramafic and Cr, V-rich metasediments is also represented by samples plotting in field 7.

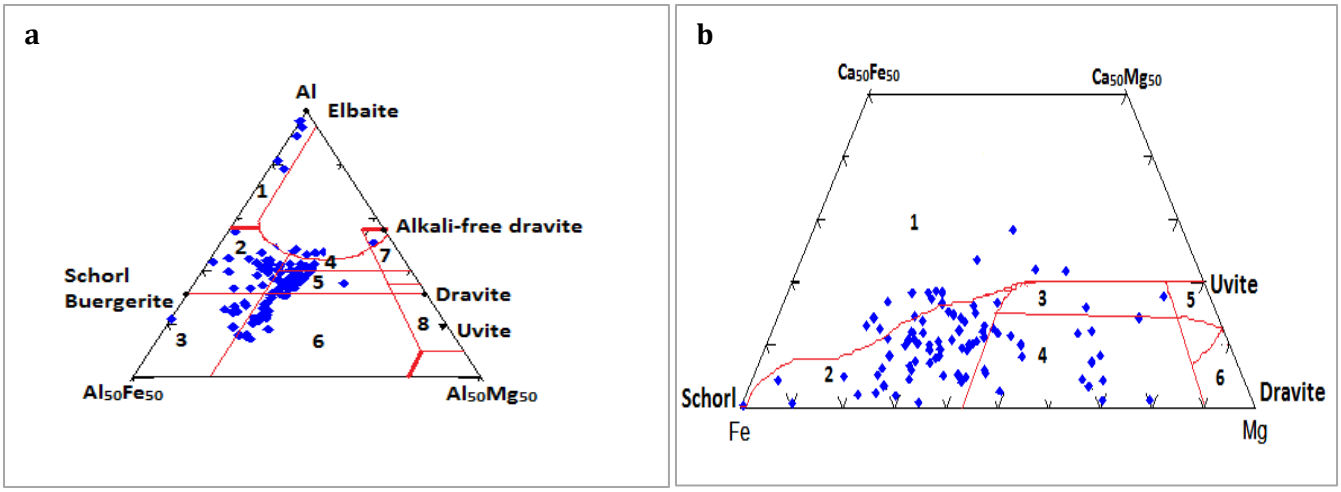

Figure 26. Ternary discrimination diagrams for tourmaline compositions analysed by QEMSCAN. After Henry and Guidotti (1985). a) Al – $Fe_{(tot)}$ – Mg. 1 – Li-rich granitoid pegmatites and aplites; 2 – Li-poor granitoid and their associated pegmatites and aplites; 3 – Fe^{3+}-rich quartz-tourmaline rock (hydrothermal altered granites); 4 – Metapelites and metapsammites coexisting with Al-satured phase; 5 – Metapelites and metapsammites not coexisting with Al-satured phase; 6 – Fe^{3+} -rich quartz-tourmaline rocks, calc-silicate rocks, and metapelites; 7 – Low-Ca metaultramafic and Cr, V-rich metasediments; 8 – Metacarbonates and meta-pyroxenites. b) Ca – $Fe_{(tot)}$ – Mg. 1 – Li-rich granitoid pegmatite and aplites; 2 – Li-poor granitoid and associated pegmatite and aplite; 3 – Ca-poor metapelites, metapsammites, and quartz-tourmaline rocks; 5 – Metacarbonates; 6 – Metaultramafics.

4.2.1.5. Rutile

i. Compositional variety

Rutile is ubiquitous in medium– to high-grade metamorphic rocks (Force, 1980), and in sedimentary environments, given its stability in mechanical and chemical-breakdown (Morton, 1984). Under low-grade conditions it usually breaks down and reacts to form sphene or ilmenite (Triebold et al., 2012).

Recently, rutile chemistry drew attention as a likely controller of Na and Ta in subduction zones (Zack et al., 2002) and due to its feasibility in provenance studies. Zack et al. (2002) demonstrated that relative proportions of Ti, Nb, Ta, Mo, and other HFS elements in rutile are diagnostic of the provenance. These authors proposed that Fe, Zr, V, W, Mo and Pb have similar enrichment in metagabbroic eclogites, metabasaltic eclogites and garnet mica schists. Even though, their Cr and

Nb content are markedly different between garnet schist (metapelitic) and metagrabbroic plus metabasaltic eclogites (metamafic), thus Zack et al. (2002) proposed a discriminant diagram Nb (in rutile) vs. Cr (in rutile).

The Nb versus Cr diagram of Zack et al. (2002), however has proved to be useful, the distinction between metapelitic and metamafic was not always effective, therefore Triebold et al. (2007) proposed a line defined by log (Cr/Nb) = 0, as the boundary between the two groups. Subsequently Meinhold et al. (2008) argued that rutile from metapelitic rocks has negative log (Cr/Nb) and Nb > 800 ppm contrary to metamafic which has negative log (Cr/Nb) values and Nb < 800 ppm, hence suggesting that the log (Cr/Nb) line should have its origin at Nb = 800 ppm. Triebold et al. (2012) in their summary paper of the uses of rutile in sediment provenance analysis, have introduced a line generated by the equation X = 5 * (Nb[ppm] – 500) – Cr[ppm], and comparatively demonstrated its efficiency to separate different sourced rutile.

In this study, both lines Log (Cr/Nb) = 0 with minimum Nb = 800 ppm (Meinhold et al., 2008) and X = 5 * (Nb[ppm] – 500) – Cr[ppm] (Triebold et al., 2012) were assessed (Table 5), and the latter used (Fig. 27). No different results were obtained using the line proposed either by Meinhold et al. (2008) or Triebold et al. (2012). Thus, the two groups, metamafic and metapelitic, were identified, with the latter being more abundant.

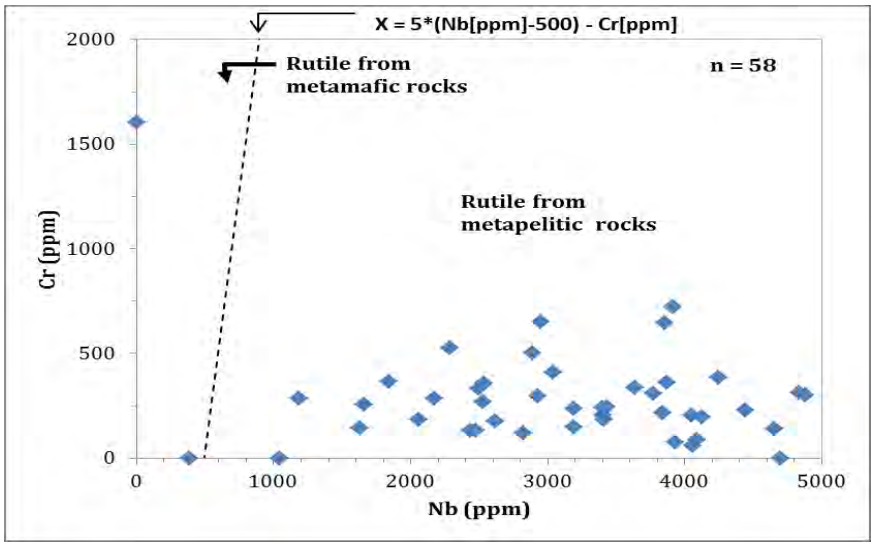

Figure 27. Nb vs. Cr discriminator rutile provenance diagram, after Triebold et al. (2012). Data from QEMSCAN.

Table 5. Chromium and niobium concentrations in rutile from QEMSCAN analysis. The two columns with conditional formulas were used to assess the line proposed by Meinhold et al. (2008) and the last column to calculate Cr [ppm] based on X = 5 * (Nb[ppm] – 500) – Cr[ppm]) (Triebold et al., 2012)

Sample_ID	Nb_2O_5	Nb (ppm)	Cr_2O_3	Cr (ppm)	Ta_2O_5	Ta (ppm)	Cr>Nb	Cr<Nb and Nb<800	Cr _from eq.
D305_15	0.00	0.00	0.16	1602.78	0.20	2031.77	1602.775	false	-2500.00
N613_37	0.00	0.00	0.25	2533.44	0.00	0.00	2533.443	false	-2500.00
N490_36	0.00	0.00	0.94	9416.37	1.57	15733.04	9416.367	false	-2500.00
N672_41	0.12	1183.98	0.03	285.03	0.02	204.30	false	false	3419.89
N490_36	0.16	1629.70	0.01	145.48	0.21	2050.83	false	false	5648.49
N672_41	0.17	1657.13	0.03	255.28	0.00	0.00	false	false	5785.63
N573_45	0.18	1840.97	0.04	366.26	0.00	0.00	false	false	6704.85
D157_32	0.21	2058.14	0.02	183.22	0.39	3948.26	false	false	7790.69
D177_6	0.22	2176.42	0.03	285.34	0.54	5371.25	false	false	8382.12
N415_11	0.23	2287.98	0.05	527.20	0.03	320.40	false	false	8939.91
N569_49	0.24	2440.45	0.01	133.72	0.02	218.97	false	false	9702.25
N573_45	0.25	2477.00	0.01	133.68	0.20	2044.91	false	false	9885.02
N613_37	0.25	2498.98	0.03	330.88	0.05	490.72	false	false	9994.92
D303_18	0.25	2531.02	0.03	269.73	0.34	3390.24	false	false	10155.08
D305_15	0.25	2533.90	0.04	357.28	0.66	6602.92	false	false	10169.50
N569_49	0.26	2616.00	0.02	174.60	0.04	401.53	false	false	10580.01
D305_8	0.28	2822.13	0.01	121.45	0.30	2972.23	false	false	11610.65
N613_13	0.29	2886.14	0.05	501.32	0.00	0.00	false	false	11930.70
N415_11	0.29	2928.43	0.03	297.35	0.35	3491.11	false	false	12142.14
D157_6	0.29	2948.33	0.07	650.20	0.37	3715.82	false	false	12241.63
D130_10	0.30	3036.52	0.04	410.11	0.34	3421.54	false	false	12682.62
N439_11	0.32	3188.35	0.02	237.63	0.44	4418.10	false	false	13441.74
D201_21	0.32	3191.36	0.01	149.82	0.19	1940.51	false	false	13456.82
D201_21	0.34	3398.51	0.02	202.95	0.39	3934.63	false	false	14492.56
D141_36	0.34	3403.62	0.02	238.48	0.17	1689.89	false	false	14518.10
N613_13	0.34	3408.20	0.02	183.03	0.38	3754.51	false	false	14540.99
N439_66	0.34	3428.71	0.02	243.16	0.03	313.84	false	false	14643.56
D177_10	0.36	3639.48	0.03	337.83	0.43	4313.65	false	false	15697.42
N672_15	0.38	3769.18	0.03	309.84	0.00	0.00	false	false	16345.91
N672_41	0.38	3836.64	0.02	216.03	0.02	212.05	false	false	16683.18
D305_15	0.39	3852.70	0.06	645.51	0.09	860.71	false	false	16763.48
N573_11	0.39	3868.93	0.04	360.80	0.35	3454.78	false	false	16844.63
N613_37	0.39	3918.86	0.07	724.74	0.38	3843.33	false	false	17094.28
D305_8	0.39	3930.07	0.01	75.98	0.24	2429.92	false	false	17150.34
N439_66	0.40	4047.56	0.02	204.87	0.15	1488.92	false	false	17737.78
N613_13	0.41	4054.99	0.01	59.69	0.24	2411.19	false	false	17774.95
N569_11	0.41	4086.64	0.01	87.50	0.26	2609.45	false	false	17933.22
N639_42	0.41	4122.84	0.02	194.47	0.35	3450.89	false	false	18114.19
D201_9	0.42	4245.86	0.04	384.58	0.42	4234.78	false	false	18729.30
N672_41	0.44	4444.87	0.02	228.76	0.40	3970.05	false	false	19724.36
D141_36	0.47	4653.69	0.01	140.68	0.51	5129.76	false	false	20768.43
N639_12	0.47	4702.36	0.00	0.00	0.45	4538.86	false	false	21011.79
N639_42	0.48	4834.98	0.03	313.94	0.13	1280.13	false	false	21674.89
D303_7	0.49	4880.79	0.03	300.58	0.42	4162.95	false	false	21903.93
N490_36	0.51	5118.01	0.26	2621.43	0.84	8364.20	false	false	23090.03
N415_6	0.53	5330.38	0.08	839.22	0.41	4069.85	false	false	24151.89
N569_11	0.54	5369.99	0.02	152.52	0.31	3082.44	false	false	24349.96
D305_15	0.54	5406.71	0.00	0.00	0.00	0.00	false	false	24533.57
N439_66	0.57	5671.43	0.01	71.39	0.30	2983.56	false	false	25857.16
N672_15	0.58	5781.19	0.02	201.04	0.48	4754.29	false	false	26405.93
N415_11	0.58	5835.49	0.09	903.58	0.55	5502.32	false	false	26677.47
N639_42	0.61	6120.95	0.00	0.00	0.12	1178.08	false	false	28104.74
D303_18	0.68	6754.17	0.19	1887.18	0.34	3417.54	false	false	31270.83
D303_7	0.69	6937.48	0.09	897.30	0.55	5525.14	false	false	32187.39
D303_18	0.90	8980.00	0.53	5251.92	0.39	3880.04	false	false	42400.00
N415_6	0.95	9538.79	0.34	3354.30	0.75	7548.46	false	false	45193.93
D175_20	0.04	382.51	0.00	0.00	0.09	913.12	false	true	-587.46
D141_36	0.10	1038.69	0.00	0.00	0.00	0.00	false	false	2693.44

ii. Thermometry

Detailed rutile chemistry study untaken by Zack et al. (2002) not only revealed the role of rutile as a carrier of HFS elements (Zr, Nb, Mo, Sn, Sb, Hf, Ta, W) and its feasibility to discriminate metamafic and metapelitic rocks, but also noted that in zircon-buffered assemblages, zirconium (Zr) incorporation in rutile is temperature dependent (Zack et al., 2004). This finding motivated the authors to calculate the first empirical thermometer based on the chemistry of natural rutile inclusions in garnet occurring eclogites rocks, with temperature spanning from 430 to 1100 ^{o}C, as defined by the equation below.

$T(^0C) = 127.8 * \ln[Zr\ in\ ppm] - 10$ (Zack et al., 2004) [6]

The authors, (Zack et al., 2004) did indeed recognize that their calibration might have been affected by errors inherited from temperatures calculated by other methods. This may probably have encourage Watson et al. (2006) to revise and present a Zr-in-rutile thermometer based on experimental data at approximately 10 kbar and temperature in the range of 675 to 1450 ^{0}C, and constrained by natural rutile from metamorphic rocks (Meinhold, 2010). Their calibration is expressed as:

$$T(^0C) = \frac{4470}{(7.36 - \log[Zr\ in\ ppm])} - 273$$ (Watson et al., 2006) [7]

Watson et al. (2006) compared their calibration with the one from Zack et al. (2004) and found a considerable discrepancy at temperatures below and above 540 ^{0}C, where the two thermometers intersect. This, lead the authors to assume pressure as a factor behind the difference and suggest further investigation, therefore Tomkins et al. (2007) undertook a consistent study of Zr-in-rutile thermometer involving pressure.

Tomkins et al. (2007) calibrated their thermometer based upon experiments taken under 10, 20 and 30 kbar in the ZrO_2 – TiO_2 – SiO_2 system, and concluded that pressure has secondary effect accompanying the primary temperature dependence of the Zr uptake of rutile (Tomkins et al., 2007). They demonstrated as could be predicted by the difference of Zr^{4+} (0.72 Å) and Ti^{4+} (0.61 Å) ionic radius, that rutile subjected to different pressure conditions allows different Ti rates of substitution by Zr as a response of crystal-structure volume reduction. Hence, they defined 3

thermometers calibrated for rutile coexisting with α-quartz, β-quartz and coesite, as follow respectively:

$$T(^0C) = \frac{83.9 + 0.410 * P}{0.1428 - R * \ln[Zr\ in\ ppm]} - 273 \quad [8]$$

$$T(^0C) = \frac{85.7 + 0.473 * P}{0.1453 - R * \ln[Zr\ in\ ppm]} - 273 \quad [9]$$

$$T(^0C) = \frac{88.1 + 0.206 * P}{0.1412 - R * \ln[Zr\ in\ ppm]} - 273 \quad [10]$$

where: P is pressure in kbar and R (gas constant) = 0.0083144 kJK^{-1}.

All the 3 thermometers, Zack et al. (2004), Watson et al. (2006) and Tomkins et al. (2007), hereafter designated T_Z, T_W and T_T have been constrained by several studies and convergence on the reliability of T_W and T_T obtained (e.g. Morton and Chenery, 2009; Meinhold, 2010; Triebold et al., 2012; Liu et al. 2014), nevertheless Zack and Luvizotto (2006) have also claimed reliability of the T_Z over the T_W.

In detrital sediments, the T_W is recommended, as the pressure is an unknown parameter (Meinhold, 2010), with additional screening for exclusion of other TiO_2 polymorphs, rather than rutile for which the thermometers were calibrated for (Triebold et al., 2012). Therefore, in this study the TiO_2 analyses were first submitted to "phase probability" test using the excel spreadsheet of Triebold et al. (2011), and only samples with probability of being rutile ≥ 0.75 used to calculate temperatures based on the T_W.

Calculated temperatures for the Nataka rutiles varies from 600 to 1000 ^{0}C, with the majority falling in the range from 750 to 850 ^{0}C (Fig. 28), meaning large contribution high-grade metamorphic rocks.

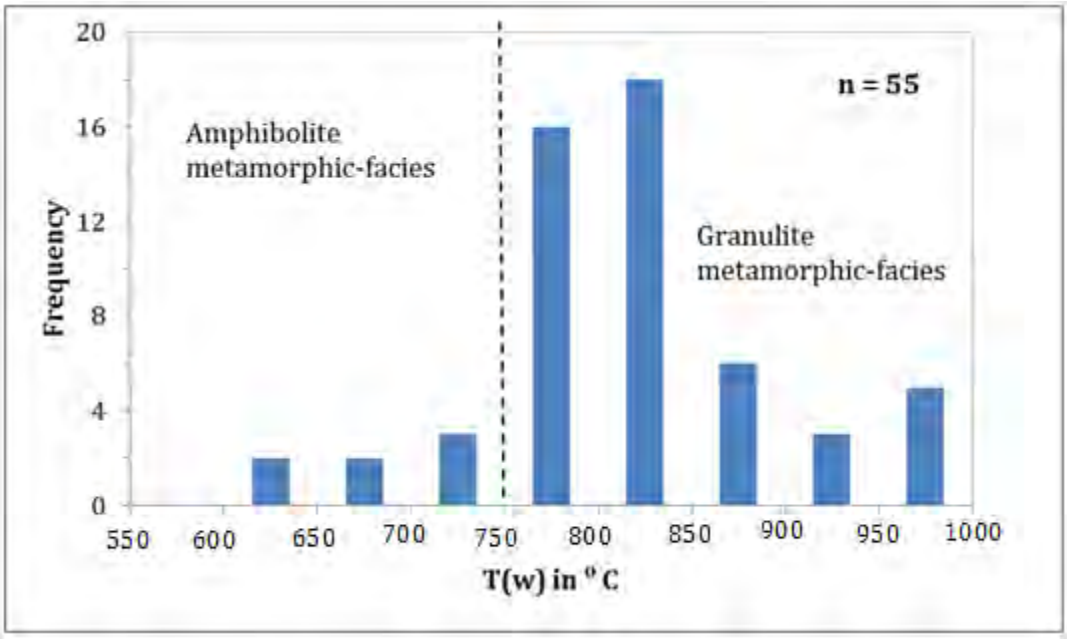

Figure 28. Temperatures distribution histogram. Data obtained using Zr concentrations in rutile (from QEMSCAN analysis) and calibrated thermometer of Watson et al. (2006)

4.2.2. U-Pb DATING

In situ U-Pb geochronology of zircon has been applied in the geoscience field to constrain age growth of minerals from igneous and metamorphic rocks (Mezger & Krogstad, 1997), and to infer maximum deposition ages and correlation of sedimentary basins, using well established high-resolution secondary ion mass spectrometry (SIMS) or sensitive high mass resolution ion microprobe (SHRIMP). Recently, the introduction and development of laser ablation inductively coupled plasma mass spectrometry (LA-ICP-MS), which provide high throughput, accurate and precise standalone data at relatively short time and low operational costs (e.g. Frei & Gerdes, 2009; Jackson et al., 2004; Gerdes & Zeh, 2006), has enabled the application of U-Pb geochronology for sediment provenience studies (Kosler et al., 2002).

The valuable contribution of zircon geochronology in provenance studies, is however biased, due to the factors: (1) inert propriety of zircon in low to moderate temperatures (Mezger & Krogstad, 1997; Fedo et al., 2003; Moecher & Samson, 2006), thus not pointing out metasedimentary sources affected by low to moderate-grade metamorphic facies, (2) different zircon fertility

(Dickinson, 2008; Moecher & Samson, 2006), and (3) its much less and very small grains occurrence in ultra/mafic rocks (Fedo et al., 2003; Hoskin & Schaltegger, 2003).

i. Brown prismatic zircon (SE#1-1a)

This population comprises essentially brown, euhedral and long prismatic {101} grains. In cathodoluminescence (CL) images, the SE#1-1a grains commonly exhibit weak to nearly non-existent luminescence (Fig. 29e).

The U-Pb ages of 50 analyses that passed the concordance test yielded two age clusters, one between 1100 to 900 Ma, and the other about 600 to 500 Ma, considering 5 % frequency cutoff (Fig. 30). In general, cores and rims of these zircons have similar ages (e.g. A103 and 106 in Table 6, Appendix. E); slightly younger ages (~ 900 Ma) from the rims are preliminary ascribed to Pb-loss during metamictization (Mezger & Krogstad, 1997; Whitehouse et al., 1999).

A few grains have ages bracketed between 1473 and 1248 Ma (A-022, A027, A034 and A118 in Table 6). Surprisingly, the grain which yields 1473 Ma for the core, also has a rim dated at 992 Ma. Thus, these grains may represent a 1473 Ma source rock that was subsequently metamorphosed during 1000 to 900 Ma. In a similar way to the older zircon grains (1000 - 900 Ma cluster), the younger grains with ages around 600 and 500 Ma, also have metamict structure as mentioned before, therefore, these grains may have resided for a long period at medium to low temperatures, during their cooling history, where structural recovery/healing is limited (Mezger & Krogstad, 1997; Geisler et al., 2003). Their long residence at moderate- to low temperatures is supported by slow cooling rates (~ 2.2 ^{0}C to 0.1 ^{0}C Myr $^{-1}$) of the NE Mozambique basement after the EAAO reported by Emmel et al. (2011).

ii. Transparent prismatic zircon (SE#1-1b)

The zircons of this group are transparent, euhedral and prismatic {101}, with diverse internal structures, with sector and patchy zoning (Fig. 29a) prevailing over oscillatory zoning (Fig. 29c) and inherited/xenocrysts cores (Fig. 29b). The ages obtained from this population form three clusters bracketed at ca. 650 – 550 Ma, 900 – 700 Ma, and 1100 – 1000 Ma, with the latter group being dominant (Fig. 31). Age assessment within the grains support the existence of growth rims dated between 650 and 550 Ma (A221/A222, A251/A252 in Table 7), and crystallization event

during 900 and 700 Ma, as depicted by oscillatory zoning and closeness of rim and core ages (Fig. 29c and A140/A141 in Table 6).

iii. Transparent rounded zircon (SE#1-1c)

This population is made up by transparent subhedral to anhedral grains, slightly rounded, showing patchy, sector zoning (Fig. 29d, f), homogenous CL intensity, and faded oscillatory zoning (Fig. 29g). The U-Pb age spectrum is dominated by 600 – 500 Ma cluster, followed by 1100 – 1000 Ma group. Zircons with ages around 900 and 700 Ma occur in a frequency below 5 % (Fig. 32), therefore will not be discussed.

A combined interpretation of grain morphology, internal structure and ages of the younger zircon cluster (600 – 500 Ma), suggest two different prospective formation mechanisms: (i) solid-state recrystallization; and (ii) dissolution-precipitation recrystallization.

The solid-state recrystallization is essentially marked by the development of faded oscillatory zoning (Hoskin & Black, 2000; Marsh & Stockli, 2015) and growth of rims (Fig. 30g). However, this mechanism is unlikely to cause complete re-setting of the U-Pb isotopic system (Hoskin & Black, 2000), thus its prevalence may be regarded as minimum, meaning that the majority of the zircon were crystallized from melt during the peak of metamorphism.

In contrast, many grains show homogenous cathodoluminescence or inherited cores (Fig. 29d), trunked primary oscillatory zoning and amoebic morphology, suggesting that dissolution-precipitation was the likely crystallization mechanism (Geisler et al., 2007; O'Brien & Miller, 2014; Marsh & Stockli, 2015).

In summary, the validity of the U-Pd data and interpretations presented above will only be meaningful if they are related to well-defined igneous and metamorphic events, and in this particular case correlated with prospective source rocks. This will be attempted in following sections.

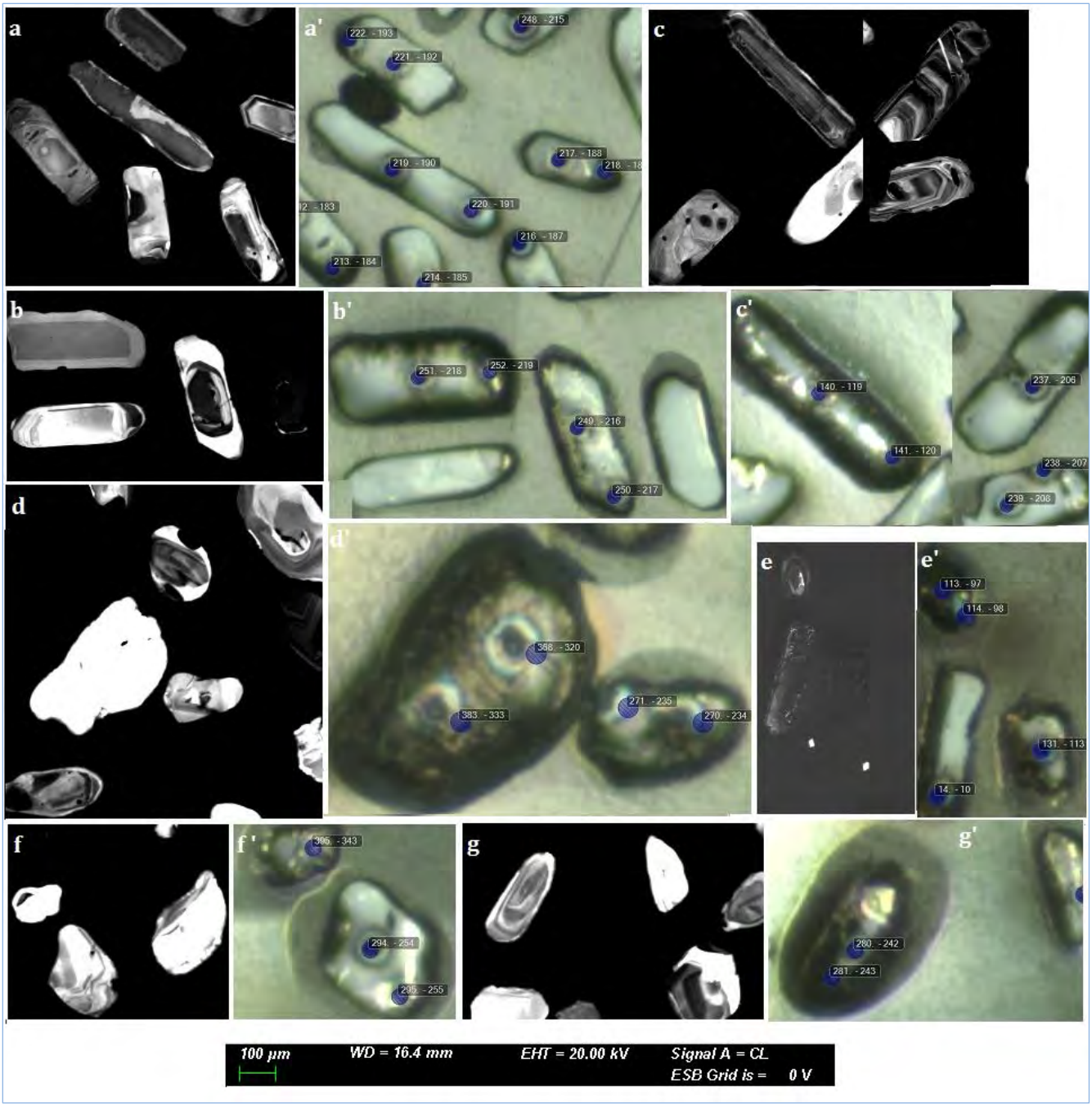

Figure 29. Collage picture of zircon CL and respective LA-ICP-MS images. a- c) Images taken from transparent prismatic zircon (SE#1-1b), showing predominantely patchy, inherited core, and oscillatory zoning respectively. d,f,g) Images of rounded transparent zircon population (SE#1-1b), ilustrating homogenous CL (centred grain in –d) and faded oscillatory zoning (f,g) . e) Brown long prismatic zircon. LA-ICP-MS not on scale. Numbered blue dots represent ablation spots.

Table 6. Representative U-Pb data for the three analysed zircon populations.

			RATIOS							AGES [Ma]						Conc.	Age Display				
Sample	Analysis-No	Sequence-No	$^{207}Pb/^{235}U$[b]	2 s[d]	$^{206}Pb/^{238}U$[b]	2 s[d]	rho[c]	$^{207}Pb/^{206}Pb$[e]	2 s[d]	$^{207}Pb/^{235}U$	2 s	$^{206}Pb/^{238}U$	2 s	$^{207}Pb/^{206}Pb$	2 s	%	analysis	$^{207}Pb/^{206}Pb$	1 s	2 s	conc %
SE#1-1a	10	A_014	1.06	0.03	0.097	0.002	0.70	0.0788	0.0017	733	22	599	13	1168	42	51	A_014	599	6	13	51
SE#1-1a	20	A_026	1.69	0.05	0.166	0.004	0.69	0.0736	0.0016	1004	31	992	21	1029	45	96	A_026	992	11	21	96
	21	A_027*	3.25	0.10	0.255	0.005	0.72	0.0923	0.0019	1469	43	1466	31	1473	39	100	A_027	1473	20	39	100
SE#1-1a	89	A_103	1.85	0.06	0.179	0.004	0.71	0.0751	0.0016	1064	33	1061	23	1070	43	99	A_103	1061	12	23	99
	90	A_106*	1.58	0.05	0.154	0.003	0.71	0.0744	0.0016	963	30	924	20	1053	44	88	A_106	924	10	20	88
SE#1-1a	97	A_113*	1.73	0.05	0.172	0.004	0.71	0.0729	0.0016	1020	32	1024	23	1011	44	101	A_113	1024	11	23	101
	98	A_114	0.68	0.02	0.083	0.002	0.65	0.0597	0.0016	528	18	513	12	593	57	86	A_114	513	6	12	86
SE#1-1a	102	A_118	2.58	0.09	0.219	0.005	0.63	0.0852	0.0024	1294	47	1278	29	1320	54	97	A_118	1320	27	54	97
SE#1-1a	103	A_119	1.90	0.06	0.177	0.004	0.68	0.0778	0.0019	1080	36	1050	24	1143	49	92	A_119	1050	12	24	92
SE#1-1b	119	A_140*	1.238	0.041	0.1309	0.0029	0.68	0.0686	0.0017	818	27	793	18	886	50	89	A_140	793	9	18	89
	120	A_141	1.425	0.047	0.1466	0.0033	0.68	0.0705	0.0017	900	29	882	20	943	49	94	A_141	882	10	20	94
SE#1-1b	183	A_212*	1.757	0.058	0.1716	0.0039	0.68	0.0743	0.0018	1030	34	1021	23	1049	49	97	A_212	1021	12	23	97
	184	A_213	1.768	0.057	0.1737	0.0039	0.70	0.0738	0.0017	1034	33	1032	23	1036	46	100	A_213	1032	12	23	100
SE#1-1b	185	A_214	1.979	0.070	0.1861	0.0043	0.65	0.0771	0.0021	1108	39	1100	25	1124	54	98	A_214	1100	13	25	98
SE#1-1b	187	A_216	1.729	0.059	0.1712	0.0039	0.67	0.0732	0.0019	1019	35	1019	23	1020	51	100	A_216	1019	12	23	100
SE#1-1b	188	A_217*	1.999	0.067	0.1888	0.0043	0.68	0.0768	0.0019	1115	37	1115	25	1116	49	100	A_217	1115	13	25	100
	189	A_218	1.926	0.061	0.1852	0.0042	0.71	0.0754	0.0017	1090	35	1095	25	1080	45	101	A_218	1095	12	25	101
SE#1-1b	190	A_219*	1.208	0.040	0.1267	0.0029	0.69	0.0691	0.0016	804	26	769	17	903	49	85	A_219	769	9	17	85
	191	A_220	1.886	0.061	0.1815	0.0041	0.70	0.0754	0.0018	1076	35	1075	24	1079	47	100	A_220	1075	12	24	100
SE#1-1b	192	A_221*	1.731	0.057	0.1724	0.0039	0.69	0.0728	0.0017	1020	34	1025	23	1009	48	102	A_221	1025	12	23	102
	193	A_222	0.878	0.031	0.1039	0.0024	0.65	0.0613	0.0016	640	22	637	14	648	57	98	A_222	637	7	14	98
SE#1-1b	208	A_239	1.923	0.062	0.1846	0.0042	0.70	0.0756	0.0017	1089	35	1092	25	1084	46	101	A_239	1092	12	25	101
SE#1-1b	216	A_249*	1.697	0.057	0.1687	0.0038	0.68	0.0730	0.0018	1008	34	1005	23	1013	50	99	A_249	1005	11	23	99
	217	A_250	1.742	0.067	0.1735	0.0040	0.60	0.0728	0.0022	1024	40	1031	24	1008	62	102	A_250	1031	12	24	102
SE#1-1b	218	A_251*	0.739	0.027	0.0914	0.0021	0.63	0.0587	0.0017	562	21	564	13	555	62	102	A_251	564	6	13	102
	219	A_252	0.700	0.028	0.0870	0.0020	0.57	0.0584	0.0019	539	22	538	12	543	73	99	A_252	538	6	12	99
SE#1-1c	234	A_270	0.683	0.025	0.0854	0.0020	0.63	0.0580	0.0017	528	19	528	12	529	63	100	A_270	528	6	12	100
	235	A_271	0.684	0.025	0.0854	0.0020	0.63	0.0581	0.0017	529	19	528	12	533	63	99	A_271	528	6	12	99
SE#1-1c	242	A_280*	0.777	0.028	0.0955	0.0022	0.63	0.0590	0.0017	584	21	588	14	567	61	104	A_280	588	7	14	104
	243	A_281	0.768	0.027	0.0935	0.0021	0.64	0.0596	0.0016	579	21	576	13	588	59	98	A_281	576	7	13	98
SE#1-1c	254	A_294*	1.791	0.069	0.1741	0.0041	0.61	0.0746	0.0023	1042	40	1035	24	1058	62	98	A_294	1035	12	24	98
	255	A_295	1.787	0.065	0.1746	0.0041	0.63	0.0742	0.0021	1041	38	1038	24	1047	57	99	A_295	1038	12	24	99
SE#1-1c	320	A_368	0.679	0.029	0.0855	0.0020	0.55	0.0576	0.0021	526	23	529	13	514	79	103	A_368	529	6	13	103
	333	A_383	0.674	0.028	0.0845	0.0020	0.57	0.0579	0.0020	523	22	523	12	525	74	100	A_383	523	6	12	100

* Used to denote analysis of the core.

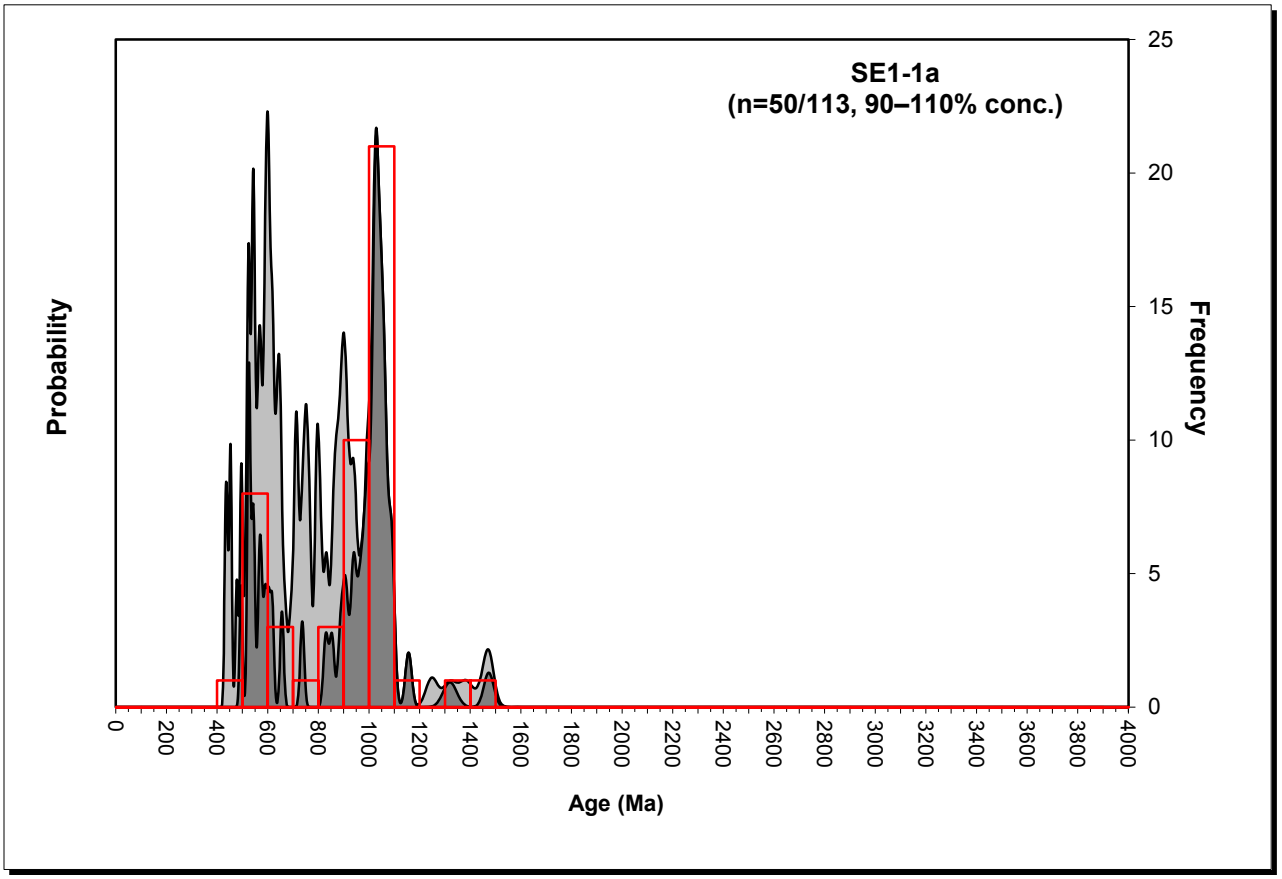

Figure 30. Combined probability-binary histograms for brown prismatic zircon (SE#1-1a). Max. age = 1473 Ma, min. age = 495 Ma, std. dev. error = 3.5, mean error = 10.2.

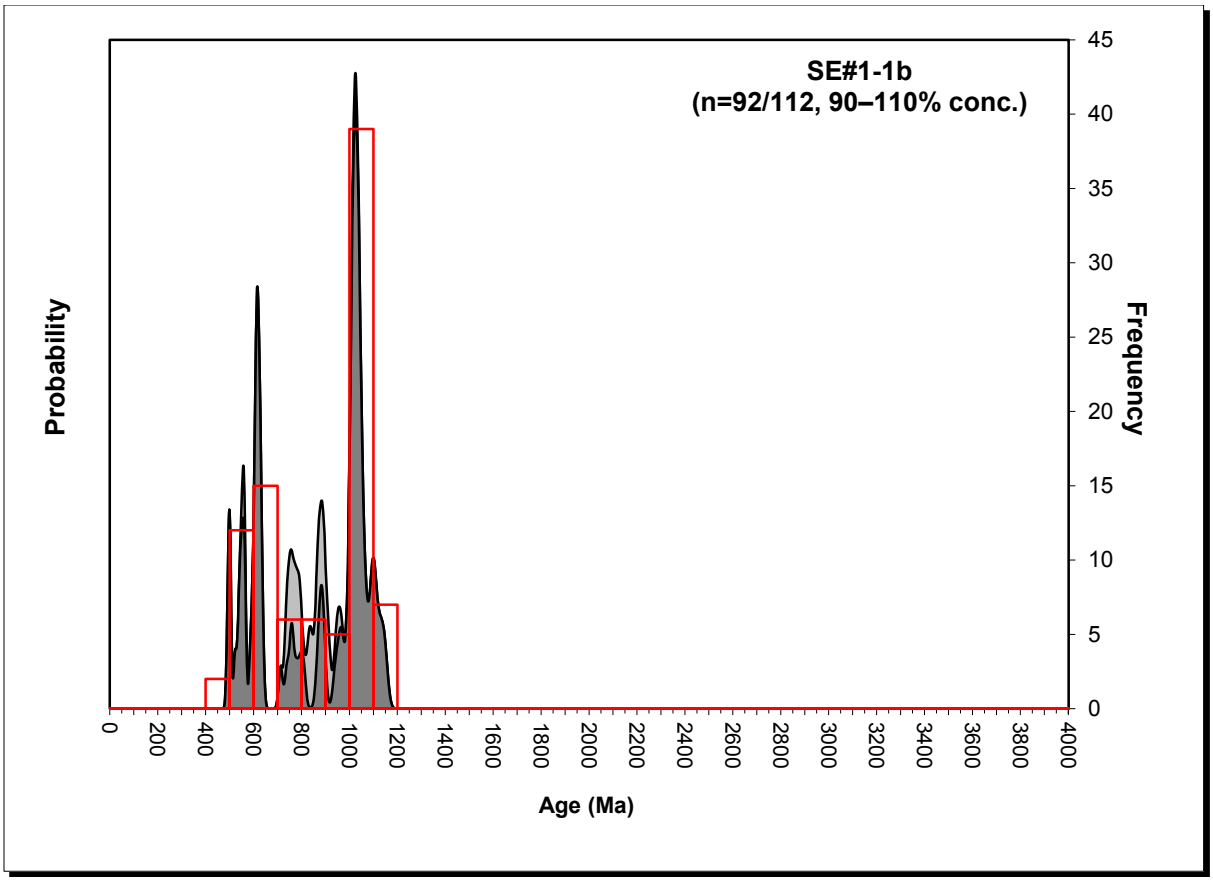

Figure 31. Combined probability-binary histograms for transparent prismatic zircon (SE#1-1b). Max. age = 1149 Ma, min. age = 492 Ma, std. dev. error = 2.4, mean error = 9.9.

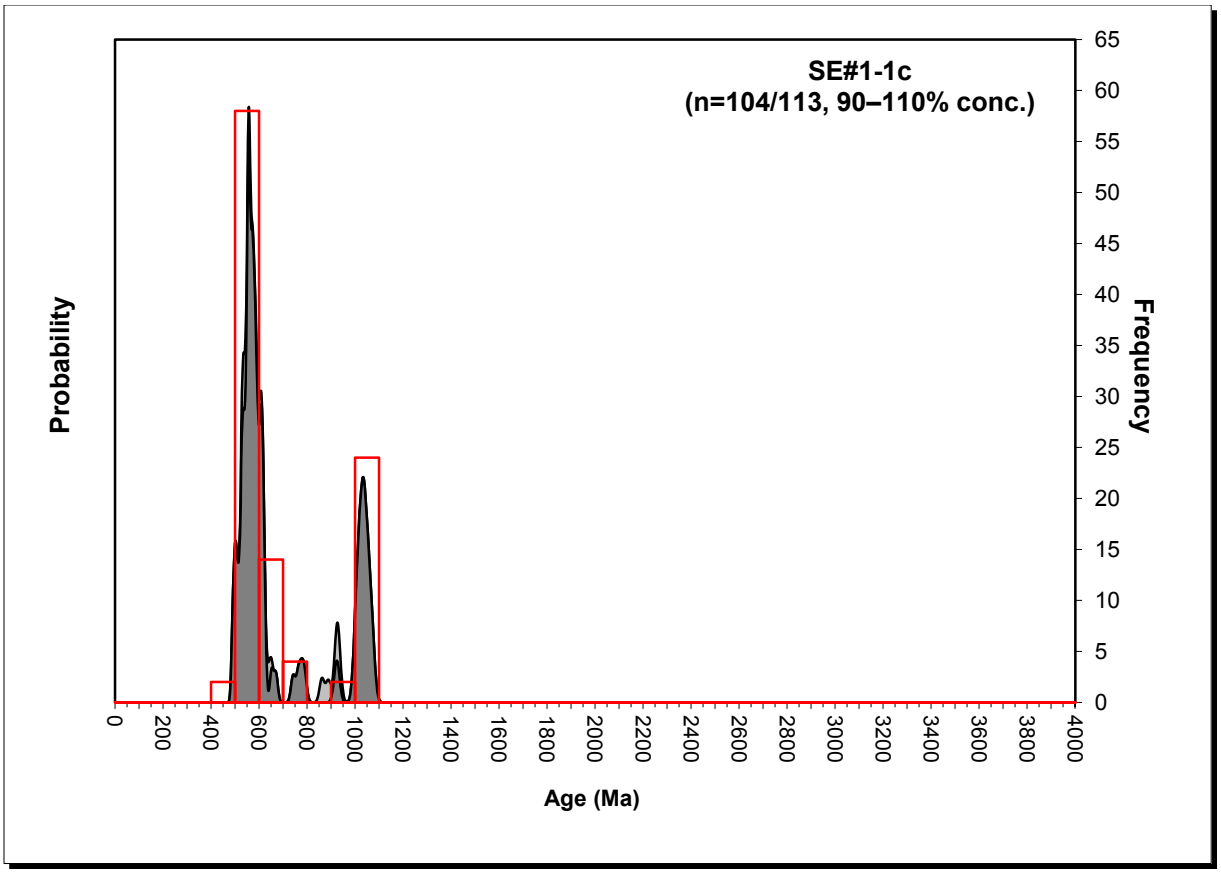

Figure 32. Combined probability-binary histograms for transparent rounded zircon (SE#1-1c). Max. age = 1072 Ma, min. age = 490 Ma, std. dev. error = 2.3, mean error = 8.1.

4.2.3. O-ISOTOPES

Morphologically different zircons (see Fig. 33, and the section above for further description), yield $\delta^{18}O$ values that are higher than those expected for mantle zircon (5.0 to 5.7± 0.3 ‰ (e.g. Valley et al., 1998), and span an extremely narrow range. A zircon megacryst from the Monastery kimberlite gave a $\delta^{18}O$ value of 5.06 ± 0.18 ‰ (2σ, n = 5) using the same laser fluorination system (Harris, unpublished data). Two analyses of the brown prismatic fraction gave $\delta^{18}O$ of 7.47 and 7.15 ‰ (avg. 7.31 ‰), and the transparent prismatic and transparent rounded fractions gave values of 7.07 ‰ and 7.69 ‰, respectively. The zircons from the concentrate, therefore, have $\delta^{18}O$ values that are about 2.0 to 2.5 ‰ higher than that of mantle zircon. At the first glance, the slight variance of these results may suggest a normal drift expected at any analytical process, but the lower values, 7.31 ‰ and 7.07 ‰ for the brown and transparent prismatic zircons, relative to the transparent rounded (7.69 ‰) may be significant, especially if considered in conjunction with the

genesis of the zircon fractions proposed in the previous section. Two hypotheses are discussed to explain the $\delta^{18}O$ values; nevertheless, the data are scanty, and to draw many conclusions would be too speculative.

The first hypothesis may be stated as: variations in the $\delta^{18}O$ values of the samples represent a normal behaviour expected in any analytical process, where the variation is due to analytical and human (sample separation) errors. The $\delta^{18}O$ values of the zircons, not surprisingly are higher than the mantle value, and are within the range of typical zircon from granitoids magmatic O-isotope ratio [6-10 ‰ (Hoefs, 2010), 7 – 14 ‰ (Eiler, 2001)]. The fact that the $\delta^{18}O$ values were measured in a composite sample, means there is likely to be quite a large range in $\delta^{18}O$ values. Thus differences in $\delta^{18}O$ of the bulk zircons may just reflect variation in proportions of zircon from different sources. Alternatively, in the second hypothesis, only the transparent prismatic zircons with $\delta^{18}O$ value of 7.07 ‰ are interpreted as representing magmatic O-isotope ratio. This interpretation is consistent with the typical magmatic oscillatory zoning observed in many zircons of this fraction (see previous section), and supported by the two values (7.47 and 7.15 ‰) obtained from the brown prismatic fraction sample, which may impart that the lower value (7.15 ‰) was less affected by grains with growth rim, thus its closeness to the magmatic O-isotope ratio, whereas the 7.47 ‰ was more affected.

If the second hypothesis holds true, as suggested here, then the $\delta^{18}O$ = 7.69 ‰ calculated for the transparent rounded zircon fraction represent O-isotope equilibration attained during the high-grade metamorphism, which was assumed to be the driving force for dissolution-precipitation mechanism proposed for the transparent rounded population formation. Hence, a question may arise concerning the way O-isotope exchange happened.

In the previous section was demonstrated by means of radioactive isotopes (U-Pb) that both prismatic populations (brown and transparent) have roughly crystallization ages around 1100 and 900 Ma, but the former zircons have experienced metamictization and Pb-loss, and developed growth rims during the metamorphic event bracket between 600 and 500 Ma, which also formed transparent rounded zircon. Thus, it is stressed that the structure damage (metamictization) has created pathways for O-isotopes exchange by volume diffusion, enhanced by high-temperature (Valley, 2003; Peck et al., 2001; Davies et al., 2015) at anhydrous conditions, on which diffusion

rate is very slow (e.g. Valley et al., 2003) and structure recovery negligible (Geisler et al. 2003). In contrast, the transparent prismatic zircons have been in equilibrium with melt, thus their pristine structure was maintained and O-isotopes exchange did not take place. The transparent rounded retained their O-isotope ratio during crystallization from melt with slightly high- $\delta^{18}O$ by diffusion-precipitation (Bindeman et al., 2008; Hoefs, 2010) in a closed system, isolated from low-$\delta^{18}O$ surface water (Fourie & Harris, 2011).

Figure 33. Zircon images taken under reflected light. Scale bar = 0.2 mm. a) Brown prismatic grains. b) Transparent prismatic. c) Transparent rounded grains

From the genesis point of view, the approximately 9 ‰ magma $\delta^{18}O$ value (if assuming $\Delta_{magma-zircon} \simeq 2$ ‰ (e.g. Valley et al. 1994) represent the high-end of I-type granitoids (6-10 ‰) and has generally been ascribed to magmas formed by partial melting of the lower-to middle crust (Hoefs, 2010; Harris et al., 1997), where subducted sediments cause $\delta^{18}O$ enrichment (Eiler, 2001). Harris et al. (1997) demonstrated that S- and I-type granites can be effectively separated using $\delta^{18}O$, and suggested a boundary at 10 ‰ (Harris & Vogeli, 2010). Thus, the 9 ‰ $\delta^{18}O$ calculated for the magma (which is close to the boundary for S- and I-type) substantiate an I-type granitoid, with

small contribution from sediments subducted during the Gondwana assemblage. This conclusion, and others achieved from previous sections will be tailored together with regional geology to decipher the provenance of the Nataka sediments in the following section.

4.2.4. DISCUSSION

Detrital zircon dating revealed four different age clusters, ca. 1400 to 1200 Ma, 1100 to 900 Ma, 900 to 700 Ma, and 600 to 500 Ma. Excepting the cluster with ages bracketed between 1400 and 1200 Ma, all the others represent typical Greenville and East Africa Antarctica orogeny ages. The age spectrum agrees well with calculated temperatures based on Zr-in rutile thermometry, which impart major contribution from granulite metamorphic-facies terranes, and some from amphibolite facies (Fig. 28). Therefore, taking into consideration the present location of the deposit, on a broad scale the sediments may have been sourced from the Mozambique belt Meso- and Neoproterozoic complexes that crop out NE of Mozambique (Fig. 4) and extending into neighbour countries (e.g. Malawi, Tanzania).

The ages bracketed between 1400 and 1200 Ma were not reported from any nearby Mozambique belt Complex to date. However on a regional scale, rocks dated in that time interval were reported from sedimentary sequence of the Burindi Supergroup, including A and S-types granitoids (GTK Consortium, 2006c). Additional information of rocks aged between 1400 and 1200 Ma comes from Mivula Hill syenite and Nyka-type granitoids (eastern Zambia), supracrustal rocks of the Zâmbuè Supergroup and volcanic rocks of the Fíngoè Supergoup (Tete province, NW Mozambique), and the Chewore ophiolite (northern Zimbabwe) (GTK Consortium, 2006c). Thus, assuming the reconstruction model of the Nampula block (which hosts the Nataka deposit) prior to Gondwana collision and amalgamation, which assemblies the block with the Kalahari craton and the West Dronning Mound Land (e.g. Grantham et al., 2011), the likely primary source of sediments may has been the Chewore ophiolite of Zimbabwe, thereafter the sediments were assimilated by juvenile volcanic magmas that formed the Nampula block during the Greenville orogeny.

Macey et al. (2010) based upon 1250 Ma inherited zircon from Culicui Suite, and 1800 Ma aged detrital zircon from a metasedimentary portion of the Mesoproterozoic Molócuè Group, which is partially made up of sediments from the Mocuba Suite, proposed that the Nampula block evolved close to Palaeoprotorozoic and early-Mesoproterozoic terranes. This evidence and the roughly

constant drainage pattern of the lower-Zambezi river (runs across NW Mozambique) after breakup of Gondwana compared to its present vicinity (e.g. Moore & Larkin, 2001), are tentatively used to support the Mocuba Suite and Molócuè Groups as ultimate sources of sediments with ages bracket between 1400 to 1200 Ma.

Crystallization ages between 1100 and 900 Ma are reported throughout the Nampula, Unango and Marrupa Complexes. The former has ages slightly older ca. 1100 than the other two. Thus, the abundance of detrital zircons with ages between 1100 to 1000 Ma (Fig. 30 – 32) suggests a major contribution from the Nampula Complex, favoured by its closeness to the deposition location. Furthermore, Cr-spinel varietal studies (Fig. 27) revealed sediments provenance from rocks with intra-plate basalts, OIB (Ocean-island basalt), IA (Island-arc magmas) and MORB (?) signatures. These go along with mixed IA and MORB (?) signatures from the Molócuè Group, within- plate from the Culicui Suite, volcanic- arc settings from the Rapale Gneiss and Mocuba Suite, described by Macey et al. (2010) in the Nampula Complex, and is consistent with granitoids generated by partial melting of the lower-to middle crust (more I-type granite than S-type – 9 ‰ $\delta^{18}O$) in a continental-oceanic active margin, which culminated with the closure of the Mozambican ocean, during Greenville orogeny.

In addition, provenance from the Molócuè Group is envisaged by the tholeitic character observed in Figure 24c, the projection of nearly all rutile analysed in the field of metapelitic source (Fig. 27), and for instance the scatter of tourmaline analyses in the Li-rich granitoid pegmatites, Fe-rich quartz-tourmaline, and metapelites and metapsamites fields (Fig. 26), given that this geologic unit (the Molócuè Group) encompasses most of the metapelitic rocks within the Nampula Complex, and is wealthy in Li-minerals, tourmaline, and other valuable minerals (e.g. Lächelt, 2004).

Within the age cluster 1100 – 1000 Ma, transparent rounded zircon form a prominent population (Fig. 32), which can be ascribed to distal sourcing, for instance the Tete Suite with associated massifs (NW Mozambique), and/or reworking by waves of red dune. Provenance from the Tete Suite, nevertheless its impressive Fe-Ti mineral layers (e.g. GTK Consortium, 2006d; Cílek & Duda, 1989) is unlikely, due to its location across the Zambezi river, which runs along the Zambezi graben (to some extent works as a boundary between NE and NW Mozambique) and discharges in the Indian Ocean (about 500 km from the deposit), and shore-parallel currents that run

southward (Castelino et al., 2015), hindering marine sediments transportation from the Zambezi river loads to the north. Therefore, the reworking of red dune formations is thought to be feasible, as younger sediments are seen veneering the red dune Topuito Formation (Fig. 6) and form important accumulations such as the Moebase Formation (Macey et al., 2007).

Ages between 900 and 700 Ma are reported from transparent euhedral zircons (Fig. 31), with inherited xenocrysts, patchy, sector and oscillatory zoning structures. Corfu et al. (2003) ascribe xenocrystic and zoning structures to zircon of igneous genesis. Therefore, on a local perspective (within NE Mozambique), rocks dated at this time interval (900 – 700 Ma) are predominantly found in plutons within the Xixano, including minor contribution of the Montepuez and Lalamo Complexes (Norconsult Consortium, 2007), Karoo aged basalts and andesites of the Angoche Group (resorption zircon aged between ca. 494 and 716 Ma) (Macey et al., 2007), and metasedimentary rocks of the Ocua Complex. In this context, two ultimate prospective sources are surmised and assessed: (1) the Xixano, Montepuez and Lalamo Complexes, together with metasediments of the Ocua Complex; and (2) the basalts and andesites of the Angoche Group.

The source (1) comprises, among other rock types, massive mafic intrusions (enderbite, mafic gabbro and diorite), which is in accord with predominant mafic plutonic feature observed in Figure 23a. In contrast, the source (2) has volcanic rocks of intermediate composition, and calc-alkine character (Macey et al., 2007), conflicting with the projection of many magnetite in the mafic plutonic field (Fig. 23a) and Cr-spinel in the tholeitic character (Fig. 24c). Therefore, despite the closeness of the Angoche Group (at some place it makes the basement of the deposit) its contribution to the sediment load is unlikely, hence the Xixano, Montepuez, Lalamo and Ocua Complexes suggested as major sediments source.

The features of the transparent rounded zircons, aged between 600 and 500 Ma, suggest a metasedimentary source rock which was subjected to high-grade metamorphic conditions, in order to enable dissolution-precipitation of zircons (proposed genesis in this research – see previous sections). Such a condition is observed in the Ocua Complex (Lúrio Belt), where metasedimentary rocks with Neoproterozoic ages are found, and metamorphism reached granulite facies at ca. 575 Ma (Ueda et al., 2012).

CHAPTER 5. CONCLUSION AND RECOMMENDATIONS

The results presented in this thesis, argue that the Nataka deposit was formed in a warm climate, prevailed during Pleistocene, as a result of protracted interplay of high erosion rates at the hinterland and sea level fluctuations. The sediments were sourced from the Meso- and Neoproterozoic rocks cropping out in the NE Mozambique, of which the metapelites, metamafic, Li-rich/poor granitoids and pegmatite of the Molócuè Group, and mafic plutonic of the Xixano Complex (with associated Lalamo, Montepuez and Ocua Complex) have been the major sources. Speckled organic matter is thought to have been deposited in conjunction with clastic sediments.

The Nataka heavy mineral assemblage is made up of valuable minerals dominated by unaltered to slightly altered ilmenite (~50 Wt. %), zircon (~9 wt. %), rutile (~3.5 wt. %) and pseudorutile-leucoxene (~3.0 wt. %), in association with less-valuable magnetite-ulvospinel (~9 wt. %), tourmaline (~ 4 wt. %), staurolite (~ 4 wt. %) and Cr-spinel (~2 wt. %).

The ilmenite has experienced three types of alteration, summarized as follow:

- Type I – took place during magmatic crystallization or metamorphism at the source rock, via oxy-exsolution mechanism and produced ilmenite intimately associated with Ti-magnetite and rutile, forming vermiform, sandwich, and exsolution lamellae textures. The lamellae were subsequently leached out as Fe hydroxides opening up voids in the hosting mineral (mostly ilmenite);
- Type II – developed in three stages, of which the last stage is related to Al and Si impurity increase. In the first stage, it consisted of progressive hydration, oxidation of ferrous ion to its ferric state and ion removal. In grains with weaken structures due to iron removal, water was incorporated to ilmenite structure forming hydrated ilmenite. Sediments diagenese and burial compacted the ilmenite structure hindering water to be added to the structure, pushing alteration to proceed and forming pseudorutile in the second stage. During the third stage, reducing conditions prevailed and all Fe^{3+} and Ti^{4+} was dissolved, followed by Ti^{4+} precipitation as polycrystalline TiO_2.
- Type III – occurred randomly within the deposit, as a result of ilmenite interaction with acidic humus generated by organic matter decomposition catalysed by direct sunshine.

The occurrence of diagenetic alteration phases spanning through the entire spectrum qualify the Nataka ilmenite into typical ilmenite (TiO_2 between 48 and 52 wt. %) and medium-to highly altered ilmenite (TiO_2 between 55 to 90 wt. %), however the predominance of unaltered to slightly altered ilmenite has concealed the occurrence of high-TiO_2 minerals (pseudorutite and leucoxene) using bulk sample analytical techniques.

Titanomagnetite with a TiO_2 content approaching 35 wt. % (ulvospinel) is likely to occur, together with intimately intergrown Fe–Ti oxides mineral, which have their magnetic and electrostatic properties governed by the degree of association.

In the light of this research the following is recommended:

- Detailed heavy minerals study of different fractions obtained from manifold magnetic field and electrostatic amperages, which can provide to mining companies valuable information to better predict their products;
- Assess the effect of ilmenite comminution to disaggregate and enhance the recoverability of high-Ti phases;
- In situ measurement of oxygen and Hf isotopes of zircons, to further constrain the provenance of the sediments.

REFERENCES

Ahmed, M.M. 2010. Effect of comminution on particle shape and surface roughness and their relation to flotation process. International Journal of Mineral Processing. 94(3):180-191.

Andersen, J.C., Rollinson, G.K., Snook, B., Herrington, R. & Fairhurst, R.J. 2009. Use of QEMSCAN® for the characterization of Ni-rich and Ni-poor goethite in laterite ores. Minerals Engineering. 22(13):1119-1129.

Arai, S. 1992. Chemistry of chromian spinel in volcanic rocks as a potential guide to magma chemistry. Mineralogical Magazine. 56(383):173-184.

Ayling, B., Rose, P., Petty, S., Zemach, E. & Drakos, P.2012. QEMSCAN (Quantitative evaluation of minerals by scanning electron microscopy): capability and application to fracture characterization in geothermal systems. Proc, Thirty-Seventh Workshop on Geotherm Reserv Eng. Stanford, California: Stanford University.

Babu, D.S., Thomas, K., Mohan Das, P. & Damodaran, A. 1994. Alternation of ilmenite in the Manavalakurichi deposit, India. Clays and Clay Minerals. 42(5):567-571.

Bagheri, G., Bonadonna, C., Manzella, I. & Vonlanthen, P. 2015. On the characterization of size and shape of irregular particles. Powder Technology. 270:141-153.

Bailey, S.W., Weege, R.J., Cameron, E.N. & Spedden, H. 1956. The alteration of ilmenite in beach sands. Economic Geology. 51(3):263-279.

Barnes, S.J. & Roeder, P.L. 2001. The range of spinel compositions in terrestrial mafic and ultramafic rocks. Journal of Petrology. 42(12):2279-2302.

Basu, A. & Molinaroli, E. 1991. Reliability and application of detrital opaque Fe-Ti oxide minerals in provenance determination. Geological Society, London, Special Publications. 57(1):55-65.

Belousova, E., Griffin, W.L., O'Reilly, S.Y. & Fisher, N. 2002. Igneous zircon: trace element composition as an indicator of source rock type. Contributions to Mineralogy and Petrology. 143(5):602-622.

Bindeman, I.N., Fu, B., Kita, N.T. & Valley, J.W. 2008. Origin and evolution of silicic magmatism at Yellowstone based on ion microprobe analysis of isotopically zoned zircons. Journal of Petrology. 49(1):163-193.

Bingen, B., Jacobs, J., Viola, G., Henderson, I., Skår, Ø., Boyd, R., Thomas, R., Solli, A. et al. 2009. Geochronology of the Precambrian crust in the Mozambique belt in NE Mozambique, and implications for Gondwana assembly. Precambrian Research. 170(3):231-255.

Bröcker, M. & Franz, L. 2000. The contact aureole on Tinos (Cyclades, Greece): tourmaline-biotite geothermometry and Rb-Sr geochronology. Mineralogy and Petrology. 70(3-4):257-283.

Buddington, A. & Lindsley, D. 1964. Iron-titanium oxide minerals and synthetic equivalents. Journal of Petrology. 5(2):310-357.

Castelino, J.A., Reichert, C., Klingelhoefer, F., Aslanian, D. & Jokat, W. 2015. Mesozoic and Early Cenozoic sediment influx and morphology of the Mozambique Basin. Marine and Petroleum Geology. 66:890-905.

Cílek, V.G. & Duda, J. 1989. Industrial minerals of Mozambique. Geological Survey.

Coastal & Environmental Sevices. Grahamstown. 2000. Environmental Impact Assessment, Kenmare Moma Titanium Minerals Project in Mozambique. Vol 1. Grahamstown. South Africa.

Corfu, F., Hanchar, J.M., Hoskin, P.W. & Kinny, P. 2003. Atlas of zircon textures. Reviews in Mineralogy and Geochemistry. 53(1):469-500.

Dare, S.A., Barnes, S. & Beaudoin, G. 2012. Variation in trace element content of magnetite crystallized from a fractionating sulfide liquid, Sudbury, Canada: implications for provenance discrimination. Geochimica Et Cosmochimica Acta. 88:27-50.

Dare, S.A., Barnes, S., Beaudoin, G., Méric, J., Boutroy, E. & Potvin-Doucet, C. 2014. Trace elements in magnetite as petrogenetic indicators. Mineralium Deposita. 49(7):785-796.

Davies, J.H., Stern, R.A., Heaman, L.M., Rojas, X. & Walton, E.L. 2015. Resolving oxygen isotopic disturbance in zircon: A case study from the low $\delta^{18}O$ Scourie dikes, NW Scotland. American Mineralogist. 100(8-9):1952-1966.

Dawood, Y. & El-Naby, H. 2007. Mineral chemistry of monazite from the black sand deposits, northern Sinai, Egypt: a provenance perspective. Mineralogical Magazine. 71(4):389-406.

de Barros, C.E., Nardi, L.V., Dillenburg, S.R., Ayup, R., Jarvis, K. & Baitelli, R. 2010. Detrital minerals of modern beach sediments in southern Brazil: a provenance study based on the chemistry of zircon. Journal of Coastal Research. :80-93.

Dick, H.J. & Bullen, T. 1984. Chromian spinel as a petrogenetic indicator in abyssal and alpine-type peridotites and spatially associated lavas. Contributions to Mineralogy and Petrology. 86(1):54-76.

Dickinson, W.R. 2008. Impact of differential zircon fertility of granitoid basement rocks in North America on age populations of detrital zircons and implications for granite petrogenesis. Earth and Planetary Science Letters. 275(1):80-92.

Dillon, M. & Franke, C. 2009. Diagenetic alteration of natural Fe–Ti oxides identified by energy dispersive spectroscopy and low-temperature magnetic remanence and hysteresis measurements. Physics of the Earth and Planetary Interiors. 172(3):141-156.

Dupuis, C. & Beaudoin, G. 2011. Discriminant diagrams for iron oxide trace element fingerprinting of mineral deposit types. Mineralium Deposita. 46(4):319-335.

Edwards, A. 1965. The texture of the minerals and their significance. The Australisian Institute of mining and metallurgy. Melbourne, Australia.

Eiler, J.M. 2001. Oxygen isotope variations of basaltic lavas and upper mantle rocks. Reviews in Mineralogy and Geochemistry. 43(1):319-364.

El-Naby, H.H.A. & Dawood, Y.H. 2014. Testing the validity of detrital zircon chemistry as a provenance indicator. Arabian Journal of Geosciences. 7(1):341-353.

Emmel, B., Kumar, R., Ueda, K., Jacobs, J., Daszinnies, M., Thomas, R. & Matola, R. 2011. Thermochronological history of an orogen-passive margin system: An example from northern Mozambique. Tectonics. 30(2).

Fedo, C.M., Sircombe, K.N. & Rainbird, R.H. 2003. Detrital zircon analysis of the sedimentary record. Reviews in Mineralogy and Geochemistry. 53(1):277-303.

Fisher-White, M., Freeman, D., Grey, I., Lanyon, M., Pownceby, M. & Sparrow, G. 2007. Removal of chrome spinels from Murray Basin ilmenites by low temperature roasting. Mineral Processing and Extractive Metallurgy. 116(2):123-132.

Force, E.R. 1980. The provenance of rutile. Journal of Sedimentary Research. 50(2).

Fourie, D.S. & Harris, C. 2011. O-isotope study of the Bushveld Complex granites and granophyres: constraints on source composition, and assimilation. Journal of Petrology. 52(11):2221-2242.

Franke, C., Pennock, G., Drury, M., Engelmann, R., Lattard, D., Garming, J., Von Dobeneck, T. & Dekkers, M. 2007. Identification of magnetic Fe-Ti oxides in marine sediments by electron backscatter diffraction in scanning electron microscopy. Geophysical Journal International. 170(2):545-555.

Frei, D. & Gerdes, A. 2009. Precise and accurate in situ U–Pb dating of zircon with high sample throughput by automated LA-SF-ICP-MS. Chemical Geology. 261(3):261-270.

Frost, M., Grey, I., Harrowfield, I. & Mason, K. 1983. The dependence of alumina and silica contents on the extent of alteration of weathered ilmenites from Western Australia. Mineral.Mag. 47(343):201.

Frost, M., Grey, I., Harrowfield, I. & Li, C. 1986. Alteration profiles and impurity element distributions in magnetic fractions of weathered ilmenite. American Mineralogist. 71(1-2):167-175.

Gehrels, G., Rusmore, M., Woodsworth, G., Crawford, M., Andronicos, C., Hollister, L., Patchett, J., Ducea, M. et al. 2009. U-Th-Pb geochronology of the Coast Mountains batholith in north-coastal

British Columbia: Constraints on age and tectonic evolution. Geological Society of America Bulletin. 121(9-10):1341-1361.

Geisler, T., Pidgeon, R.T., Kurtz, R., Bronswijk, W.V. & Schleicher, H. 2003. Experimental hydrothermal alteration of partially metamict zircon. American Mineralogist. 88(10):1496-1513.

Geisler, T., Schaltegger, U. & Tomaschek, F. 2007. Re-equilibration of zircon in aqueous fluids and melts. Elements. 3(1):43-50.

Gerdes, A. & Zeh, A. 2006. Combined U–Pb and Hf isotope LA-(MC-) ICP-MS analyses of detrital zircons: comparison with SHRIMP and new constraints for the provenance and age of an Armorican metasediment in Central Germany. Earth and Planetary Science Letters. 249(1):47-61.

Goodall, W.R. & Scales, P.J. 2007. An overview of the advantages and disadvantages of the determination of gold mineralogy by automated mineralogy. Minerals Engineering. 20(5):506-517.

Gottlieb, P., Wilkie, G., Sutherland, D., Ho-Tun, E., Suthers, S., Perera, K., Jenkins, B., Spencer, S. et al. 2000. Using quantitative electron microscopy for process mineralogy applications. JOM. 52(4):24-25.

Grantham, G., Macey, P., Horie, K., Kawakami, T., Ishikawa, M., Satish-Kumar, M., Tsuchiya, N., Graser, P. et al. 2013. Comparison of the metamorphic history of the Monapo Complex, northern Mozambique and Balchenfjella and Austhameren areas, Sør Rondane, Antarctica: Implications for the Kuunga Orogeny and the amalgamation of N and S. Gondwana. Precambrian Research. 234:85-135.

Grantham, G., Manhica, A., Armstrong, R., Kruger, F. & Loubser, M. 2011. New SHRIMP, Rb/Sr and Sm/Nd isotope and whole rock chemical data from central Mozambique and western Dronning Maud Land, Antarctica: Implications for the nature of the eastern margin of the Kalahari Craton and the amalgamation of Gondwana. Journal of African Earth Sciences. 59(1):74-100.

Greig, D. 2001. Kenmare Moma Titanium Minerals Project. Definitive Feasibility Study. Section 3: Geology And Resource Estimation. Western Australia, MiniProc Limited.

Grey, I. & Reid, A. 1975. The structure of pseudorutile and its role in the natural alteration of ilmenite. American Mineralogist. 60(9/10):179-181.

Grey, I. & Li, C. 2003. Hydroxylian pseudorutile derived from picroilmenite in the Murray Basin, southeastern Australia. Mineralogical Magazine. 67(4):733-747.

Grimes, C.B., John, B.E., Kelemen, P., Mazdab, F., Wooden, J., Cheadle, M.J., Hanghøj, K. & Schwartz, J. 2007. Trace element chemistry of zircons from oceanic crust: a method for distinguishing detrital zircon provenance. Geology. 35(7):643-646.

Groenewald, P., Grantham, G. & Watkeys, M. 1991. Geological evidence for a Proterozoic to Mesozoic link between southeastern Africa and Dronning Maud Land, Antarctica. Journal of the Geological Society. 148(6):1115-1123.

GTK Consortium. 2006a. Map Explanation; Volume 2: Sheets 1630 – 1934. Geology of Degree Sheets Mecumbura, Chioco, Tete, Tambara, Guro, Chemba, Manica, Catandica, Gorongosa, Rotanda, Chimoio and Beira, Mozambique. Ministério dos Recursos Minerais, Direcção Nacional de Geologia, Maputo.

GTK Consortium (2006c). Map Explanation; Volume 3: Sheets 1735-1739, 1835-1836 and 1935. Geology of Degree Sheets Mutarara, Quelimane, Namacurra/Maganja, Pebane, Marromeu/Inhaminga, Chinde and Savane, Mozambique. Ministério dos Recursos Minerais, Direcção Nacional de Geologia, Maputo.

GTK Consortium. 2006d. Map Explanation; Volume 4: Sheets 1430 – 1432 and 1530 – 1534. Geology of Degree Sheets Inhamambo, Maluwera, Chifunde, Zumbo, Fíngoè-Mágoè, Songo, Cazula and Zóbuè, Mozambique. Ministério dos Recursos Minerais, Direcção Nacional de Geologia, Maputo.

Hallsworth, C. & Chisholm, J. 2008. Provenance of late Carboniferous sandstones in the Pennine Basin (UK) from combined heavy mineral, garnet geochemistry and palaeocurrent studies. Sedimentary Geology. 203(3):196-212.

Harris, C., Faure, K., Diamond, R.E. & Scheepers, R. 1997. Oxygen and hydrogen isotope geochemistry of S-and I-type granitoids: the Cape Granite suite, South Africa. Chemical Geology. 143(1):95-114.

Harris, C. & Vogeli, J. 2010. Oxygen isotope composition of garnet in the Peninsula Granite, Cape Granite Suite, South Africa: constraints on melting and emplacement mechanisms. South African Journal of Geology. 113(4):401-412.

Henry, D.J. & Guidotti, C.V. 1985. Tourmaline as a petrogenetic indicator mineral- An example from the staurolite-grade metapelites of NW Maine. American Mineralogist. 70(1-2):1-15.

Hoefs, J. & Hoefs, J. 2010. Stable isotope geochemistry. 6th Ed. ed. Berlin, Germany: Springer.

Holmgren, K., Lee-Thorp, J.A., Cooper, G.R., Lundblad, K., Partridge, T.C., Scott, L., Sithaldeen, R., Talma, A.S. et al. 2003. Persistent millennial-scale climatic variability over the past 25,000 years in Southern Africa. Quaternary Science Reviews. 22(21):2311-2326.

Hoskin, P. & Black, L. 2000. Metamorphic zircon formation by solid-state recrystallization of protolith igneous zircon. Journal of Metamorphic Geology. 18(4):423-439.

Hoskin, P.W. & Ireland, T.R. 2000. Rare earth element chemistry of zircon and its use as a provenance indicator. Geology. 28(7):627-630.

Hoskin, P.W. & Schaltegger, U. 2003. The composition of zircon and igneous and metamorphic petrogenesis. Reviews in Mineralogy and Geochemistry. 53(1):27-62.

Hugo, V. & Cornell, D. 1991. Altered ilmenites in Holocene dunes from Zululand, South Africa: petrographic evidence for multistage alteration. South African Journal of Geology. 94(5-6):365-378.

Ingram, B.A. 2005. Compiled geological map. Sheet 1639-40 Angoche. Geological seirie 1: 250 000: South Africa, Council For Geoscience.

Ireland, T., Flöttmann, T., Fanning, C., Gibson, G. & Preiss, W.V. 1998. Development of the early Paleozoic Pacific margin of Gondwana from detrital-zircon ages across the Delamerian orogen. Geology. 26(3):243-246.

Jackson, S.E., Pearson, N.J., Griffin, W.L. & Belousova, E.A. 2004. The application of laser ablation-inductively coupled plasma-mass spectrometry to in situ U–Pb zircon geochronology. Chemical Geology. 211(1):47-69.

Jacobs, J., Fanning, C.M., Henjes-Kunst, F., Olesch, M. & Paech, H. 1998. Continuation of the Mozambique Belt into East Antarctica: Grenville-age metamorphism and polyphase Pan-African high-grade events in central Dronning Maud Land. The Journal of Geology. 106(4):385-406.

Jacobs, J., Bauer, W. & Fanning, C. 2003. Late Neoproterozoic/Early Palaeozoic events in central Dronning Maud Land and significance for the southern extension of the East African Orogen into East Antarctica. Precambrian Research. 126(1):27-53.

Jacobs, J., Bingen, B., Thomas, R.J., Bauer, W., Wingate, M.T. & Feitio, P. 2008. Early Palaeozoic orogenic collapse and voluminous late-tectonic magmatism in Dronning Maud Land and Mozambique: insights into the partially delaminated orogenic root of the East African–Antarctic Orogen? Geological Society, London, Special Publications. 308(1):69-90.

Jenkins, R., Gould R.W., Gedcke, D. 1995. Quantitative X-ray spectrometry. Vol 20. 2nd ed. Marcel Dekker, Inc. New York.

Jones, G. 2009. Mineral sands: An overview of the industry. Unpublished.Capel: Iluka Resources Limited.

Hurlbut, C. S. & Sharp, W.E. 1998. Dana's minerals and how to study them. 4th ed. John Wiley & Sons, Inc.

Kamenetsky, V.S., Crawford, A.J. & Meffre, S. 2001. Factors controlling chemistry of magmatic spinel: an empirical study of associated olivine, Cr-spinel and melt inclusions from primitive rocks. Journal of Petrology. 42(4):655-671.

Karkhanavala, M. 1959. The nature of arizonite. Economic Geology. 54(7):1302-1308.

Komar, P.D. & Wang, C. 1984. Processes of selective grain transport and the formation of placers on beaches. The Journal of Geology. :637-655.

Košler, J., Fonneland, H., Sylvester, P., Tubrett, M. & Pedersen, R. 2002. U–Pb dating of detrital zircons for sediment provenance studies—a comparison of laser ablation ICPMS and SIMS techniques. Chemical Geology. 182(2):605-618.

Kroner, A. 1977. Precambrian mobile belts of southern and eastern Africa—ancient sutures or sites of ensialic mobility? A case for crustal evolution towards plate tectonics. Tectonophysics. 40(1):101-135.

Kröner, A., Collins, A., Hegner, E., Willner, A., Muhongo, S. & Kehelpannala, K. 2001. The East African Orogen: new zircon and Nd ages and implications for Rodinia and Gondwana supercontinent formation and dispersal. Gondwana Research. 4(2):179-181.

Lächelt, S. 2004. The geology and mineral resources of Mozambique. República de Moçambique, Monostério dos Recursos Minerais e Energia, Direcçâo Nacional de Geologia.

Lattard, D., Sauerzapf, U. & Käsemann, M. 2005. New calibration data for the Fe–Ti oxide thermo-oxybarometers from experiments in the Fe–Ti–O system at 1 bar, 1,000–1,300 C and a large range of oxygen fugacities. Contributions to Mineralogy and Petrology. 149(6):735-754.

Li, G., Yan, W., Zhong, L., Xia, Z. & Wang, S. 2015. Provenance of heavy mineral deposits on the northwestern shelf of the South China Sea, evidence from single-mineral chemistry. Marine Geology. 363:112-124.

Little, L., Becker, M., Wiese, J. & Mainza, A.N. 2015. Auto-SEM particle shape characterisation: Investigating fine grinding of UG2 ore. Minerals Engineering. 82 (2015): 92-100.

Liu, L., Xiao, Y., Wörner, G., Kronz, A., Simon, K. & Hou, Z. 2014. Detrital rutile geochemistry and thermometry from the Dabie orogen: Implications for source–sediment links in a UHPM terrane. Journal of Asian Earth Sciences. 89:123-140.

LST heavy liquid. n.d. Available: https://www.uvm.edu/cosmolab/msds/lst_msds.pdf [2015, August 03].

Lynd, L.E. 1960. Alteration of ilmenite. Economic Geology. 55(5):1064-1068.

Lynn, B. C. & Goldup, N. 2000. Geology and geomorphology. In Environmental Impact Assessment, Kenmare Moma Titanium Minerals Project in Mozambique. Coastal & Environmental Sevices. Grahamstown. South Africa. 34-62

Maboko, M. 2000. Nd and Sr isotopic investigation of the Archean–Proterozoic boundary in north eastern Tanzania: constraints on the nature of Neoproterozoic tectonism in the Mozambique Belt. Precambrian Research. 102(1):87-98.

Macey, P.H., Ingram, B.A., Cronwright, M.S., Botha, G.A., Roberts, M.R., Grantham, G.H., Maree, L.P., Botha, P.M.W., Kota, M., Opperman, R. and Haddon, I.G. 2007. Map explanation of sheets Alto Molócuè, 1537. Murrupula, 1538. Nampula, 1539. Mogincual, 1540. Errego, 1637. Gilé (1638) and Angoche (1639-40). National Directorate of Geology, Republic of Mozambique, p.418.

Macey, P., Thomas, R., Grantham, G., Ingram, B., Jacobs, J., Armstrong, R., Roberts, M., Bingen, B. et al. 2010. Mesoproterozoic geology of the Nampula Block, northern Mozambique: Tracing fragments of Mesoproterozoic crust in the heart of Gondwana. Precambrian Research. 182(1):124-148.

Mahanjane, E.S. 2012. A geotectonic history of the northern Mozambique Basin including the Beira High–A contribution for the understanding of its development. Marine and Petroleum Geology. 36(1):1-12.

Marsh, J.H. & Stockli, D.F. 2015. Zircon U–Pb and trace element zoning characteristics in an anatectic granulite domain: Insights from LASS-ICP-MS depth profiling. Lithos. 239:170-185.

Meert, J.G. & van der Voo, R. 1997. The assembly of Gondwana 800-550 Ma. Journal of Geodynamics. 23(3):223-235.

Meert, J.G. 2003. A synopsis of events related to the assembly of eastern Gondwana. Tectonophysics. 362(1):1-40.

Meert, J.G., van der Voo, R. & Ayub, S. 1995. Paleomagnetic investigation of the Neoproterozoic Gagwe lavas and Mbozi complex, Tanzania and the assembly of Gondwana. Precambrian Research. 74(4):225-244.

Meinhold, G. 2010. Rutile and its applications in earth sciences. Earth-Science Reviews. 102(1):1-28.

Meinhold, G., Anders, B., Kostopoulos, D. & Reischmann, T. 2008. Rutile chemistry and thermometry as provenance indicator: an example from Chios Island, Greece. Sedimentary Geology. 203(1):98-111.

Melezhik, V., Bingen, B., Fallick, A., Gorokhov, I., Kuznetsov, A., Sandstad, J., Solli, A., Bjerkgård, T. et al. 2008. Isotope chemostratigraphy of marbles in northeastern Mozambique: apparent depositional ages and tectonostratigraphic implications. Precambrian Research. 162(3):540-558.

Mezger, K. & Krogstad, E. 1997. Interpretation of discordant U-Pb zircon ages: an evaluation. Journal of Metamorphic Geology. 15(1):127-140.

Moecher, D.P. & Samson, S.D. 2006. Differential zircon fertility of source terranes and natural bias in the detrital zircon record: Implications for sedimentary provenance analysis. Earth and Planetary Science Letters. 247(3):252-266.

Moore, A. & Larkin, P. 2001. Drainage evolution in south-central Africa since the breakup of Gondwana. South African Journal of Geology. 104(1):47-68.

Morton, A. 1984. Stability of detrital heavy tertiary sandstones from sea basin. Clay Minerals. 19:287-308.

Morton, A.C. 1985. A new approach to provenance studies: electron microprobe analysis of detrital garnets from Middle Jurassic sandstones of the northern North Sea. Sedimentology. 32(4):553-566.

Morton, A. & Chenery, S. 2009. Detrital rutile geochemistry and thermometry as guides to provenance of Jurassic–Paleocene sandstones of the Norwegian Sea. Journal of Sedimentary Research. 79(7):540-553.

Morton, A., Whitham, A. & Fanning, C. 2005. Provenance of Late Cretaceous to Paleocene submarine fan sandstones in the Norwegian Sea: integration of heavy mineral, mineral chemical and zircon age data. Sedimentary Geology. 182(1):3-28.

Morton, A.C. & Hallsworth, C.R. 1999. Processes controlling the composition of heavy mineral assemblages in sandstones. Sedimentary Geology. 124(1):3-29.

Nadoll, P., Mauk, J.L., Hayes, T.S., Koenig, A.E. & Box, S.E. 2012. Geochemistry of magnetite from hydrothermal ore deposits and host rocks of the Mesoproterozoic Belt Supergroup, United States. Economic Geology. 107(6):1275-1292.

Nadoll, P., Angerer, T., Mauk, J.L., French, D. & Walshe, J. 2014. The chemistry of hydrothermal magnetite: a review. Ore Geology Reviews. 61:1-32.

Nair, A.G., Babu, D., L Vivekanandan, K. & Vlach, S.R. 2006. Differential alteration of ilmenite in a tropical beach placer, southern India: microscopic and electron probe evidences. Resource Geology. 56(1):75-81.

Nair, A.G., Babu, D.S., Damodaran, K., Shankar, R. & Prabhu, C. 2009. Weathering of ilmenite from Chavara deposit and its comparison with Manavalakurichi placer ilmenite, southwestern India. Journal of Asian Earth Sciences. 34(2):115-122.

Nesse, W.D. 2000. Introduction to mineralogy. Oxford University Press. New York.

Norconsult Consortum. 2007. Geological Mapping - Lot 1. Sheet explanation: 1039 Muidine, 1040 Palma, 1134 Ponta Messuli, 1135 Lupilichi, 1136 Milepa, 1137 Macalange, 1138, Negomano, 1139 Mueda, 1140 Moçimboa da Praia, 1234 Metangula, 1235 Macaloge-Chiconono, 1236 Mavago, 1237 Mecula, 1238 Xixano, 1239 Meluco, 1240 Quissinga-Pemba, 1334 Meponda, 1335 Lichinga, 1336 Majune, 1337 Marrupa, 1338 Namuno, 1339 Montepuez, 1340 Mecufi, 1435 Mandimba, 1436

Cuamba, 1437 Malema, 1438 Ribáuè-Mecuburi, 1535 Insaca, 1536 Gurué, 1635 Milange, 1636 Lugela-Mocuba. National Directorate of Geology, Republic of Mozambique.

O'Brien, T.M. & Miller, E.L. 2014. Continuous zircon growth during long-lived granulite facies metamorphism: a microtextural, U–Pb, Lu–Hf and trace element study of Caledonian rocks from the Arctic. Contributions to Mineralogy and Petrology. 168(4):1-19.

Palmer, C. 1909. Arizonite, ferric metatitanate. American Journal of Science. (166):353-356.

Peck, W.H., Valley, J.W., Wilde, S.A. & Graham, C.M. 2001. Oxygen isotope ratios and rare earth elements in 3.3 to 4.4 Ga zircons: Ion microprobe evidence for high $\delta^{18}O$ continental crust and oceans in the Early Archean. Geochimica Et Cosmochimica Acta. 65(22):4215-4229.

Pettijohn, F. 1941. Persistence of heavy minerals and geologic age. The Journal of Geology. :610-625.

Pirrie, D., Power, M.R., Rollinson, G.K., Wiltshire, P.E., Newberry, J. & Campbell, H.E. 2009. Automated SEM-EDS (QEMSCAN®) Mineral analysis in forensic soil investigations: Testing instrumental reproducibility. In Criminal and Environmental Soil Forensics. Springer. 411-430.

Philander, C. & Rozendaal, A. 2015a. Geology of the Cenozoic Namakwa Sands Heavy Mineral Deposit, West Coast of South Africa: A World-Class Resource of Titanium and Zircon. Economic Geology. 110(6):1577-1623.

Philander, C. & Rozendaal, A. 2015b. Detrital zircon geochemistry and U–Pb geochronology as an indicator of provenance of the Namakwa Sands heavy mineral deposit, west coast of South Africa. Sedimentary Geology. 328:1-16.

Pownceby, M. 2005. Compositional and textural variation in detrital chrome-spinels from the Murray Basin, southeastern Australia. Mineralogical Magazine. 69(2):191-204.

Pownceby, M. 2010. Alteration and associated impurity element enrichment in detrital ilmenites from the Murray Basin, southeast Australia: a product of multistage alteration. Australian Journal of Earth Sciences. 57(2):243-258.

Pownceby, M.I. & Fisher-White, M.J. 1999. Phase equilibria in the systems Fe_2O_3-MgO-TiO_2 and FeO-MgO-TiO_2 between 1173 and 1473 K, and Fe^{2+} -Mg mixing properties of ilmenite, ferrous-pseudobrookite and ulvospinel solid solutions. Contributions to Mineralogy and Petrology. 135(2-3):198-211.

Pownceby, M.I., Sparrow, G.J. & Fisher-White, M.J. 2008. Mineralogical characterisation of Eucla Basin ilmenite concentrates–First results from a new global resource. Minerals Engineering. 21(8):587-597.

Ramdohr, P. 1969. The ore minerals and their intergrowths. International series of monographs on earth sciences.

Ramsay, P. 1996. 9000 years of sea-level change along the southern African coastline. Quaternary International. 31:71-75.

Ramsay, P.J. & Cooper, J.A.G. 2002. Late Quaternary sea-level change in South Africa. Quaternary Research. 57(1):82-90.

Roeder, P.L. 1994. Chromite; from the fiery rain of chondrules to the Kilauea Iki lava lake. The Canadian Mineralogist. 32(4):729-746.

Roeder, P.L., Poustovetov, A. & Oskarsson, N. 2001. Growt.h forms and composition of chromian spinel in MORB magma: diffusion-controlled crystallization of chromian spinel. The Canadian Mineralogist. 39(2):397-416.

Rollinson, G.K., Andersen, J.C., Stickland, R.J., Boni, M. & Fairhurst, R. 2011. Characterisation of non-sulphide zinc deposits using QEMSCAN®. Minerals Engineering. 24(8):778-787.

Rothnie, C. 2011. Kenmare Moma Mining and Processing Annual Report. Mozambique.

Rubatto, D. 2002. Zircon trace element geochemistry: partitioning with garnet and the link between U–Pb ages and metamorphism. Chemical Geology. 184(1):123-138.

Sacchi, R., Cadoppi, P. & Costa, M. 2000. Pan-African reactivation of the Lurio segment of the Kibaran Belt system: a reappraisal from recent age determinations in northern Mozambique. Journal of African Earth Sciences. 30(3):629-639.

Salman, G. & Abdula, I. 1995. Development of the Mozambique and Ruvuma sedimentary basins, offshore Mozambique. Sedimentary Geology. 96(1):7-41.

Scotese, C.R., Gahagan, L.M. & Larson, R.L. 1988. Plate tectonic reconstructions of the Cretaceous and Cenozoic ocean basins. Tectonophysics. 155(1):27-48.

Shackleton, R. 1996. The final collision zone between East and West Gondwana: where is it? Journal of African Earth Sciences. 23(3):271-287.

Sircombe, K. 2000. The usefulness and limitations of binned frequency histograms and probability density distributions for displaying absolute age data; Radiogenic age and isotopic studies: Report 13.

Stern, R.J. 1994. Arc-assembly and continental collision in the Neoproterozoic African orogen: implications for the consolidation of Gondwanaland. Annual Review of Earth and Planetary Sciences. 22:319-351.

Taylor, M. & Stone, G.W. 1996. Beach-ridges: a review. Journal of Coastal Research. 612-621.

Technical and other information on LST float. n.d. Available: https://www.polytungstate.co.uk/LST_Fastfloat.pdf [2015, August 03].

Temple, A. 1966. Alteration of ilmenite. Economic Geology. 61(4):695-714.

Teufer, G. & Temple, A. 1966. Pseudorutile—A new mineral intermediate between ilmenite and rutile in the N alteration of ilmenite.

Thomson, J.A. 2006. A rare garnet-tourmaline-sillimanite-biotite-ilmenite-quartz assemblage from the granulite-facies region of south-central Massachusetts. American Mineralogist. 91(11-12):1730-1738.

Tomkins, H., Powell, R. & Ellis, D. 2007. The pressure dependence of the zirconium-in-rutile thermometer. Journal of Metamorphic Geology. 25(6):703-713.

Triebold, S., von Eynatten, H., Luvizotto, G.L. & Zack, T. 2007. Deducing source rock lithology from detrital rutile geochemistry: an example from the Erzgebirge, Germany. Chemical Geology. 244(3):421-436.

Triebold, S., Luvizotto, G.L., Tolosana-Delgado, R., Zack, T. & von Eynatten, H. 2011. Discrimination of TiO_2 polymorphs in sedimentary and metamorphic rocks. Contributions to Mineralogy and Petrology. 161(4):581-596.

Triebold, S., von Eynatten, H. & Zack, T. 2012. A recipe for the use of rutile in sedimentary provenance analysis. Sedimentary Geology. 282:268-275.

Tsikouras, B., Pe-Piper, G., Piper, D.J. & Schaffer, M. 2011. Varietal heavy mineral analysis of sediment provenance, Lower Cretaceous Scotian Basin, eastern Canada. Sedimentary Geology. 237(3):150-165.

Ueda, K., Jacobs, J., Thomas, R.J., Kosler, J., Jourdan, F. & Matola, R. 2012. Delamination-induced late-tectonic deformation and high-grade metamorphism of the Proterozoic Nampula Complex, northern Mozambique. Precambrian Research. 196:275-294.

Valley, J.W. 2003. Oxygen isotopes in zircon. Reviews in Mineralogy and Geochemistry. 53(1):343-385.

Valley, J.W., Chiarenzelli, J.R. & McLelland, J.M. 1994. Oxygen isotope geochemistry of zircon. Earth and Planetary Science Letters. 126(4):187-206.

Valley, J.W., Kinny, P.D., Schulze, D.J. & Spicuzza, M.J. 1998. Zircon megacrysts from kimberlite: oxygen isotope variability among mantle melts. Contributions to Mineralogy and Petrology. 133(1-2):1-11.

Valley, J.W., Bindeman, I.N. & Peck, W.H. 2003. Empirical calibration of oxygen isotope fractionation in zircon. Geochimica Et Cosmochimica Acta. 67(17):3257-3266.

van Houten, F.B. 1973. Origin of red beds: a review-1961-1972. Annual Review of Earth and Planetary Sciences. 1:39.

Viola, G., Henderson, I., Bingen, B., Thomas, R., Smethurst, M. & De Azavedo, S. 2008. Growt.h and collapse of a deeply eroded orogen: Insights from structural, geophysical, and geochronological constraints on the Pan-African evolution of NE Mozambique. Tectonics. 27(5).

von Eynatten, H. & Gaupp, R. 1999. Provenance of Cretaceous synorogenic sandstones in the Eastern Alps: constraints from framework petrography, heavy mineral analysis and mineral chemistry. Sedimentary Geology. 124(1):81-111.

Watson, E., Wark, D. & Thomas, J. 2006. Crystallization thermometers for zircon and rutile. Contributions to Mineralogy and Petrology. 151(4):413-433.

Weibel, R. 1998. Diagenesis in oxidising and locally reducing conditions—an example from the Triassic Skagerrak formation, Denmark. Sedimentary Geology. 121(3):259-276.

Whitehouse, M.J., Kamber, B.S. & Moorbath, S. 1999. Age significance of U–Th–Pb zircon data from early Archaean rocks of west Greenland—a reassessment based on combined ion-microprobe and imaging studies. Chemical Geology. 160(3):201-224.

Woltering, M., Johnson, T. C., Werne, J. P., Schouten, S., & Damsté, J. S. S. 2011. Late Pleistocene temperature history of Southeast Africa: a TEX 86 temperature record from Lake Malawi. Palaeogeography, Palaeoclimatology, Palaeoecology. 303(1): 93-102.

Wort, M. & Jones, M. 1980. X-ray diffraction and magnetic studies of altered ilmenite and pseudorutile. Mineral Mag. 43(329):659.

Xia, X., Sun, M., Zhao, G., Li, H. & Zhou, M. 2004. Spot zircon U-Pb isotope analysis by ICP-MS coupled with a frequency quintupled (213 nm) Nd-YAG laser system. Geochemical Journal. 38(2):191-200.

Yang, S., Wang, Z., Guo, Y., Li, C. & Cai, J. 2009. Heavy mineral compositions of the Changjiang (Yangtze River) sediments and their provenance-tracing implication. Journal of Asian Earth Sciences. 35(1):56-65.

Zack, T. & Luvizottow, G. 2006. Application of rutile thermometry to eclogites. Mineralogy and Petrology. 88(1-2):69-85.

Zack, T., Kronz, A., Foley, S. & Rivers, T. 2002. Trace element abundances in rutiles from eclogites and associated garnet mica schists. Chemical Geology. 184(1):97-122.

Zack, T., Moraes, R. & Kronz, A. 2004. Temperature dependence of Zr in rutile: empirical calibration of a rutile thermometer. Contributions to Mineralogy and Petrology. 148(4):471-488.

Zussman, J. 1967. Physical methods in determinative mineralogy. Academic Press, Inc. London.

APPENDIXES

Appendix A – Drill holes coordinates (UTM/WGS84/37S) and samples collected for the study.

BHID	East	North	RL	Drilled Depth	Samples
DHNAT130	552000	8167801	93	**51**	D130_10 D130_35
DHNAT141	552798	8167801	91	**48**	D141_7 D141_36
DHNAT157	553597	8167805	82	**45**	D157_6 D157_32
DHNAT175	554400	8168000	60	**27**	D175_8 D175_20
DHNAT177	554400	8168401	60	**24**	D177_10 D177_16
DHNAT201	550413	8168805	61	**27**	D201_9 D201_21
DHNAT303	554400	8170200	56	**23**	D303_7 D303_18
DHNAT305	554400	8169400	57	**17**	D305_8 D305_15
NT00415	549600	8167800	57	**12**	N415_6 N415_11
NT00439	550401	8165202	103	**75**	N439_11 N439_66
NT00490	551192	8167798	92	**45**	N490_11 N490_36
NT00569	554400	8166000	93	**58**	N569_11 N569_49
NT00573	554399	8166799	87	**57**	N573_11 N573_45
NT00613	555594	8167801	77	**51**	N613_13 N613_37
NT00639	556403	8167800	77	**52**	N639_12 N639_42
NT00672	557595	8167799	78	**51**	N672_15 N672_41

Appendix B – XRF results for composite and stand-alone samples of ilmenite concentrates.

Bulk sample_ID	Sample_ID	LOI	TiO2	TiO2_correct	Fe2O3	Fe2O3_correct	Al2O3	Cr2O3	SiO2	Al2O3+SiO2	V2O5	CaO	MgO	MnO
		%	%		%		%	%	%		%	%	%	%
14BS0199	**D175_8 & D175_20**	0.75	44.59	50.19	33.49	37.69	4.74	0.21	6.42	11.16	0.09	0.05	0.49	1.25
14BS0194	**N573_11**	-0.67	42.56	48.07	39.27	44.35	5.45	0.20	6.01	11.46	0.10	0.06	0.55	1.30
14BS0195	**N573_45**	-0.85	42.49	47.49	39.50	44.14	4.74	0.21	5.78	10.52	0.11	0.05	0.53	1.32
14BS0123	**N613_13**	0.99	42.89	48.00	39.33	44.02	4.77	0.22	5.87	10.65	0.11	0.05	0.51	1.30
14BS0124	**N613_37**	-0.53	42.55	47.42	39.17	43.66	4.52	0.24	5.76	10.27	0.11	0.05	0.52	1.29
14BS0072	**N639_12**	-0.67	43.76	48.50	40.22	44.58	4.60	0.21	5.18	9.78	0.11	0.04	0.51	1.31
14BS0073	**N639_42**	1.00	46.97	52.34	32.84	36.59	4.68	0.30	5.57	10.25	0.10	0.04	0.53	1.17
14BS0017	**N672_41**	1.57	44.64	52.69	29.21	34.48	6.75	0.32	8.53	15.28	0.11	0.06	0.60	1.10
14BS0018	**N672_15**	-1.25	41.90	46.66	42.18	46.98	4.89	0.20	5.33	10.22	0.11	0.05	0.56	1.35
10BS006	**D130_10 & D130_35**	-1.40	41.08	45.08	43.65	47.90	3.75	0.17	5.12	8.87	0.13	0.03	0.45	1.39
10BS007	**D141_7 & D141_36**	-1.38	39.73	44.37	44.11	49.26	3.46	0.13	6.99	10.45	0.13	0.03	0.40	1.37
10BS014	**D157_6 & D157_32**	-0.30	43.36	47.64	41.11	45.17	4.10	0.20	4.89	8.99	0.12	0.03	0.47	1.38
10BS023	**D201_9 & D201_21**	0.02	44.41	52.22	31.64	37.19	5.37	0.23	9.58	14.95	0.13	0.04	0.43	1.14
11BS104	**D177_10 & D177_16**	1.51	44.11	50.28	34.26	39.06	5.16	0.21	7.12	12.28	0.09	0.05	0.48	1.27
11BS105	**D305_8 & D305_15**	0.74	45.13	51.07	34.42	38.95	4.97	0.23	6.65	11.62	0.10	0.05	0.50	1.33

Sample_ID	Nb2O5	ZrO2	HfO2	P2O5	K2O	CeO2	SnO2	PbO	Th	U	Total	Fe^{2+}	FeO	Fe^{3+}	Fe_2O_3
	%	%	%	%	%	%	%	[ppm]	[ppm]	[ppm]	%	%	%	%	%
D175_8 & D175_20	0.09	4.44	0.09	0.18	0.00	0.18	0.01	235.73	544.88	65.46	**96.32**	8.39	10.80	18.72	26.77
N573_11	0.10	3.47	0.07	0.13	0.01	0.14	0.01	23.75	310.16	40.73	**99.44**	15.02	19.32	16.12	23.04
N573_45	0.09	3.54	0.07	0.11	0.00	0.13	0.01	17.60	304.29	60.49	**98.66**	16.35	21.04	14.96	21.39
N613_13	0.10	3.83	0.08	0.16	0.00	0.17	0.01	33.26	336.52	60.07	**99.41**	14.68	18.88	16.67	23.83
N613_37	0.10	3.74	0.08	0.14	0.00	0.15	0.00	54.40	370.79	68.09	**98.41**	15.22	19.58	15.93	22.77
N639_12	0.10	3.67	0.07	0.13	0.00	0.14	0.00	51.48	328.86	57.92	**100.05**	14.68	18.88	16.95	24.24
N639_42	0.11	3.97	0.08	0.18	0.00	0.23	0.00	275.81	465.25	62.55	**96.78**	6.54	8.42	19.70	28.17
N672_41	0.10	5.06	0.10	0.18	0.00	0.22	0.00	456.48	516.68	68.73	**96.97**	4.90	6.30	20.17	28.83
N672_15	0.10	2.84	0.06	0.14	0.00	0.16	0.00	46.89	342.24	65.54	**99.87**	16.23	20.88	16.43	23.48
D130_10 & D130_35	0.09	2.97	0.06	0.11	0.00	0.17	0.00	81.02	315.69	23.23	**99.17**	17.37	22.34	16.28	23.27
D141_7 & D141_36	0.09	2.87	0.06	0.12	0.00	0.14	0.00	49.82	293.36	18.22	**99.63**	18.94	24.36	15.69	22.43
D157_6 & D157_32	0.10	3.16	0.06	0.11	0.00	0.14	0.00	112.90	323.20	33.79	**99.24**	16.18	20.81	15.72	22.47
D201_9 & D201_21	0.06	3.77	0.07	0.19	0.01	0.19	0.02	247.71	638.85	40.00	**97.28**	2.85	3.67	21.21	30.32
D177_10 & D177_16	0.09	4.54	0.09	0.18	0.01	0.24	0.01	386.33	559.94	42.32	**97.91**	9.24	11.89	18.37	26.27
D305_8 & D305_15	0.10	3.82	0.07	0.21	0.01	0.23	0.01	445.98	671.92	51.00	**97.83**	7.37	9.48	19.56	27.96

Cont. of the table above. [Ti and Fe] $_{corrected}$ = [Oxide]*100/(100 – [Al + Si])

	SiO2	TiO2	Al2O3	Fe2O3	MnO	MgO	CaO	Na2O	K2O	P2O5	SO3	Cr2O3	NiO	ZrO2	H2O-	LOI	Sum
D130-10	4.72	43.33	4.40	44.57	1.45	0.61	0.02	0.35	0.01	0.12	b.d.	0.15	0.01	2.19	0.11	-1.84	100.20
D130-35	4.01	43.15	3.45	45.37	1.42	0.56	0.02	0.33	0.01	0.14	b.d.	0.15	0.01	2.80	0.11	-1.93	99.59
D141-7	4.49	42.60	4.18	45.45	1.44	0.60	0.02	0.33	0.02	0.13	b.d.	0.12	0.01	2.58	0.13	-1.99	100.12
D141-36	4.24	42.18	3.08	46.32	1.41	0.49	0.01	0.33	0.02	0.17	b.d.	0.13	0.01	3.44	0.12	-2.06	99.89
D157-6	4.70	44.19	4.60	41.86	1.40	0.60	0.02	0.34	0.02	0.11	b.d.	0.17	0.01	2.43	0.16	-1.47	99.14
D157-32	4.01	45.80	3.58	42.63	1.42	0.56	0.01	0.33	0.02	0.13	b.d.	0.20	0.01	2.58	0.08	-1.68	99.68
D175-8	5.35	46.49	4.92	36.65	1.34	0.61	0.02	0.32	0.02	0.18	0.01	0.23	0.01	3.36	0.16	-0.30	99.36
D175-20	5.33	48.29	4.60	31.61	1.24	0.58	0.01	0.32	0.02	0.17	0.01	0.24	0.01	4.07	0.66	0.97	98.14
D177-10	4.76	47.22	4.26	36.95	1.41	0.60	0.03	0.33	0.02	0.17	b.d.	0.20	0.01	3.23	0.12	-0.43	98.89
D177-16	5.23	47.43	4.38	36.74	1.38	0.58	0.01	0.33	0.02	0.17	b.d.	0.22	0.01	3.20	0.13	-0.38	99.45
D201-9	3.78	51.38	4.10	33.96	1.37	0.61	0.02	0.32	0.01	0.20	b.d.	0.19	0.01	1.85	0.13	1.08	99.01
D201-21	7.05	45.32	5.29	34.51	1.22	0.56	0.03	0.31	0.02	0.19	b.d.	0.24	0.01	2.33	0.18	1.63	98.89
D303-7	6.10	46.92	4.21	34.12	1.41	0.59	0.02	0.32	0.02	0.18	0.01	0.14	0.01	4.01	0.12	0.07	98.24
D303-18	5.34	46.86	4.30	35.00	1.33	0.53	0.01	0.33	0.02	0.18	b.d.	0.20	0.01	3.47	0.14	0.59	98.31
D305-8	8.43	41.52	5.62	34.10	1.20	0.47	0.01	0.33	0.02	0.25	0.01	0.26	0.01	3.84	0.21	1.15	97.43
D305-15	4.69	47.52	3.79	35.62	1.41	0.57	0.02	0.33	0.02	0.23	b.d.	0.17	0.01	4.03	0.13	-0.33	98.21
N415-6	4.56	50.26	4.04	32.48	1.28	0.59	0.02	0.32	0.02	0.24	0.01	0.19	0.01	3.14	0.16	0.96	98.27
N415-11	4.84	49.61	4.09	32.02	1.20	0.60	0.02	0.33	0.02	0.27	0.01	0.22	0.01	3.70	0.16	1.13	98.23
N439-11	3.88	43.73	3.81	45.26	1.41	0.58	0.02	0.32	0.01	0.15	b.d.	0.20	0.01	2.06	0.07	-1.82	99.69
N439-66	5.40	49.32	4.62	30.82	1.11	0.57	0.02	0.33	0.04	0.26	0.01	0.34	0.01	3.39	0.21	1.67	98.12
N490-11	4.46	44.42	4.18	41.62	1.43	0.58	0.02	0.33	0.02	0.16	b.d.	0.18	0.01	2.65	0.09	-1.08	99.08
N490-36	4.23	47.22	3.76	37.75	1.40	0.54	0.01	0.31	0.03	0.18	0.01	0.21	0.01	2.54	0.14	0.13	98.47
N569-11	4.33	44.06	4.40	44.24	1.42	0.62	0.02	0.35	0.03	0.08	b.d.	0.19	0.01	1.93	0.11	-1.62	100.18
N569-49	8.04	38.83	4.91	37.08	1.20	0.57	0.02	0.36	0.02	0.20	b.d.	0.24	0.01	8.05	0.08	-1.24	98.37
N573-11	5.44	43.16	4.98	41.66	1.37	0.61	0.02	0.34	0.02	0.12	b.d.	0.19	0.01	2.94	0.09	-1.52	99.43
N573-45	5.55	44.41	5.24	39.26	1.30	0.59	0.01	0.34	0.03	0.10	b.d.	0.22	0.01	3.05	0.07	-1.00	99.19
N613-13	5.85	47.07	5.43	33.56	1.25	0.65	0.02	0.34	0.02	0.20	b.d.	0.28	0.01	3.49	0.13	0.56	98.86
N613-37	5.55	43.41	5.07	40.77	1.36	0.64	0.06	0.34	0.03	0.16	b.d.	0.19	0.01	3.21	0.08	-0.85	100.04
N639-12	4.95	50.17	4.17	32.36	1.16	0.58	0.01	0.31	0.02	0.18	0.01	0.33	0.01	2.84	0.12	1.29	98.53
N639-42	4.49	45.26	4.44	41.11	1.36	0.60	0.02	0.33	0.02	0.12	b.d.	0.23	0.01	2.13	0.11	-0.80	99.42
N672-15	5.21	43.94	4.85	40.25	1.34	0.60	0.02	0.35	0.02	0.15	0.00	0.22	0.01	2.88	0.09	-1.09	98.82
N672-41	5.10	46.55	4.63	37.71	1.32	0.60	0.02	0.33	0.02	0.23	0.01	0.28	0.01	2.69	0.05	-0.21	99.36

User information:
Major oxides (values reported as wt.% except for H2O- and LOI) are measured on fused disks prepared from ignited powders,

Major oxides (values reported as wt. % except for H_2O- and LOI) are measured on fused disks prepared from ignited powders, H_2O- represents the sample weight lost upon heating the sample powder at 110 °C overnight. If the powders submitted are moist, this value can be high.
LOI is "loss on ignition", and represents the weight change (positive if weight lost) upon heating the sample to 800 °C for 4 hours.
The lower limit of detection for major oxides is 0.01 wt. %.
"b.d." is an abbreviation of "below detection" meaning that the concentration of the element was too low to quanitfy (generally <0.01 wt. % for major elements)
ZrO_2 was measured on fused disks and calibrated using a variety of rock standards, including a peridotite doped with 5wt. % ZrO_2.

Appendix C – Selected XRD pattern of the study sample

X'Pert Graphics & Identity

Scan Parameters

Scan type	Measured scan
Start angle (^{0}2 Theta)	20.015
End angle (^{0}2 Theta)	74.975
Step size (^{0}2 Theta)	0.03
Time per step (s)	1

Diffractometer, configurations & settings

Measurement type	Absolute scan
Application offset: 2 Theta (^{0})	0
Scan axis	Gonio
Scan mode	Continuous
Control unit	PW3710
Goniometer	PW1050 (Coupled Omega)
Generator	PW1830/00
Generator tension (kV)	40
Generator current (mA)	25
X-ray tube	PW2273 or PW2773 Cu LFF
Detector	PW3011 (Miniprop.)
PHD lower level (%)	35
PHD upper level (%)	80

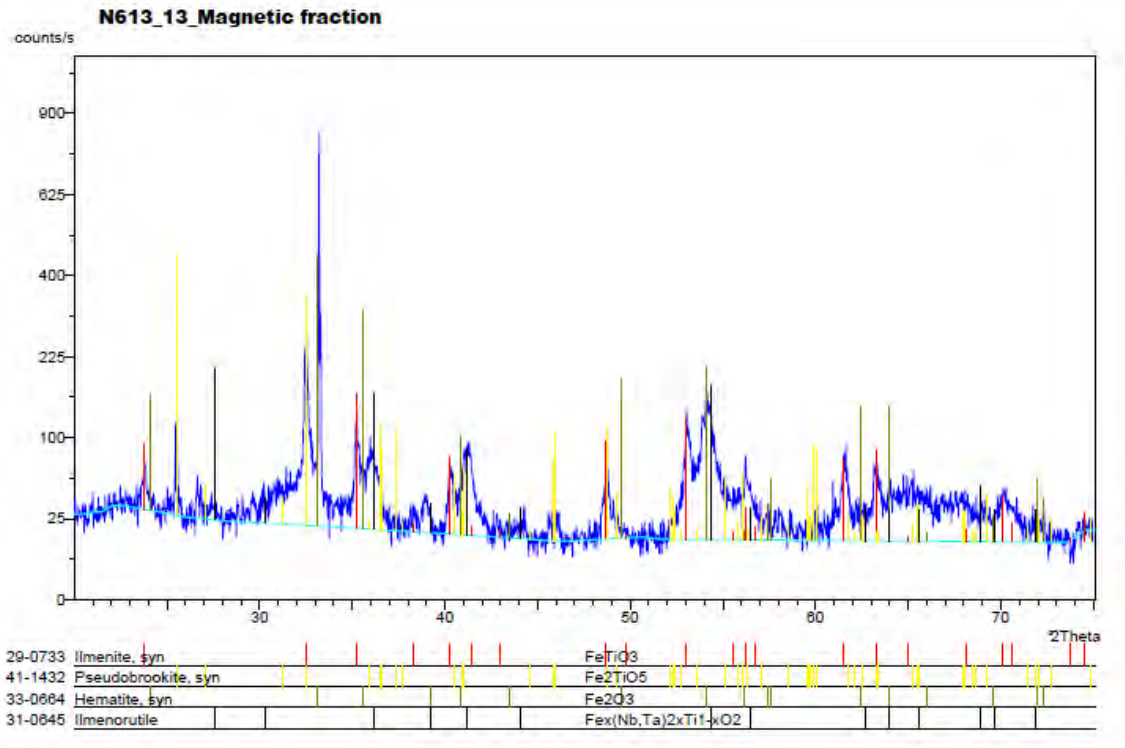

D141_6_Magnetic fraction

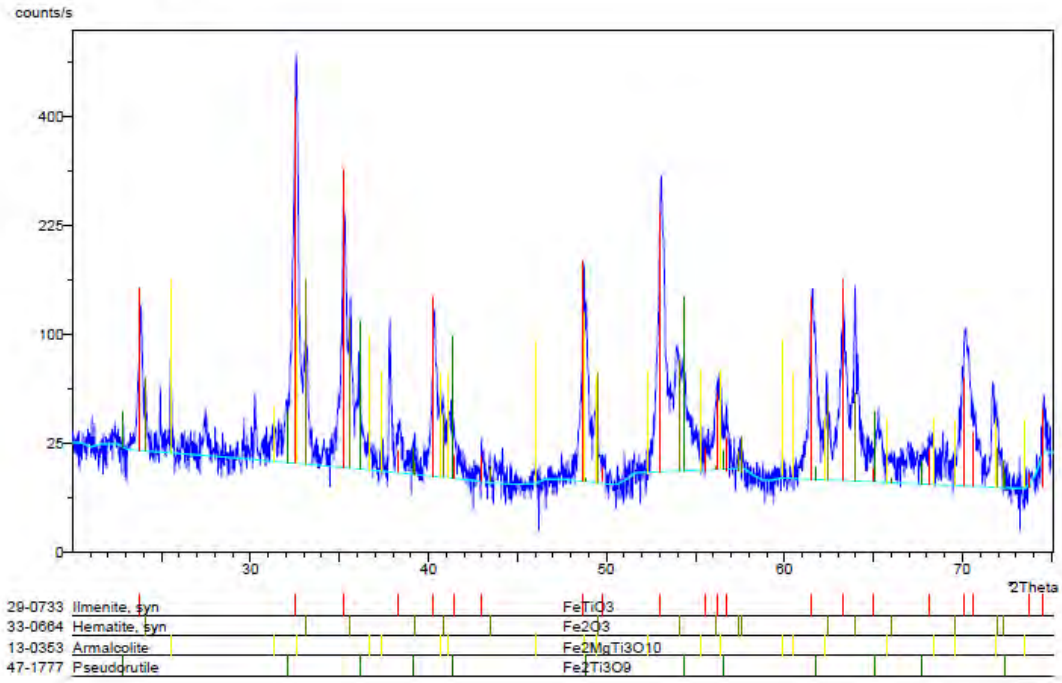

D177_10_Bulk sample

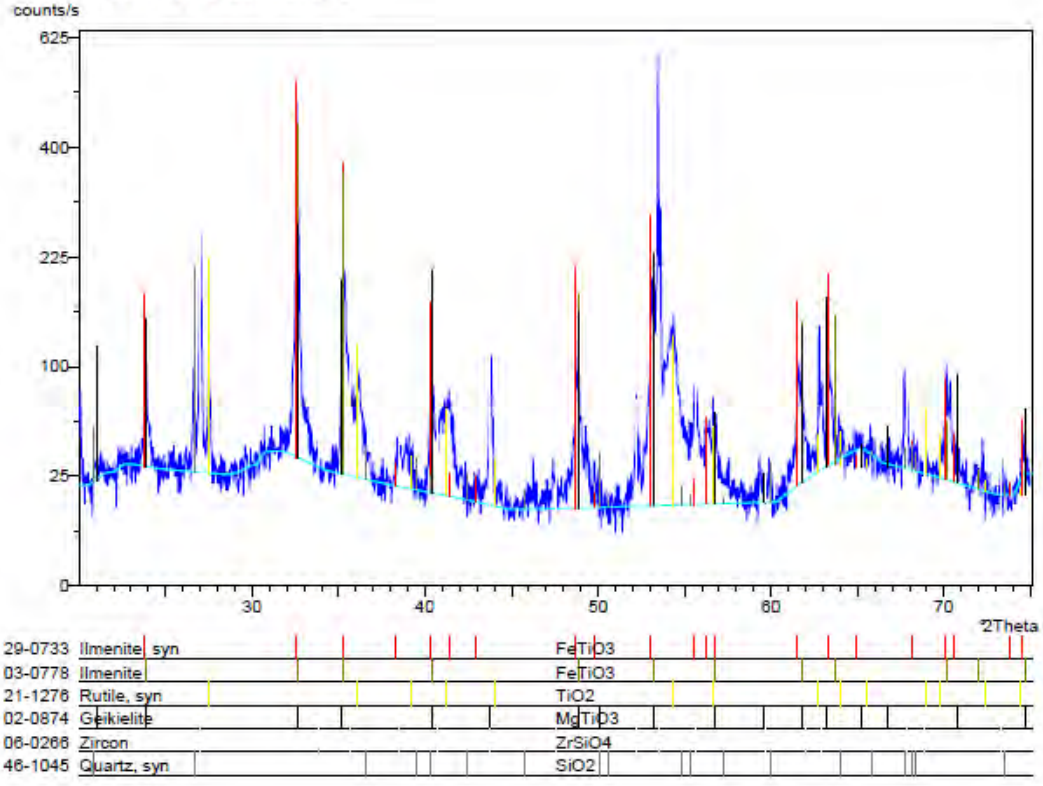

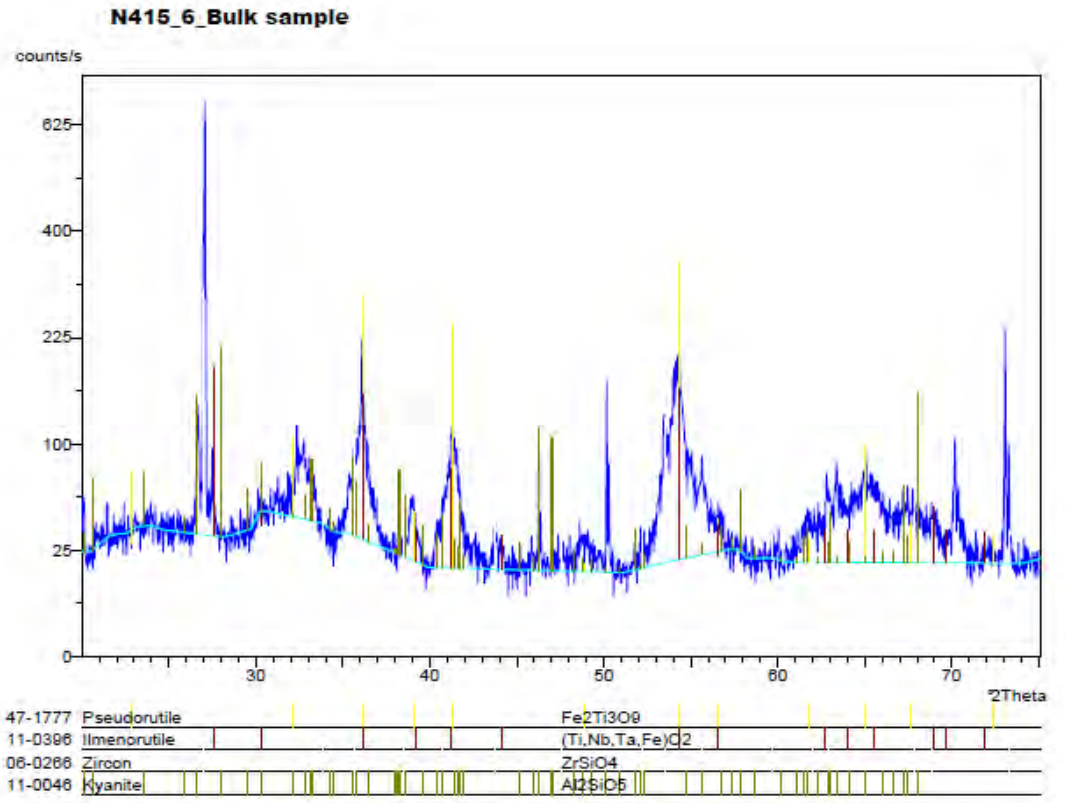
N415_6_Bulk sample
counts/s
625
400
225
100
25
0
30
40
50
60
70
°2Theta
47-1777 Pseudorutile Fe2Ti3O9
11-0396 Ilmenorutile (Ti,Nb,Ta,Fe)O2
06-0266 Zircon ZrSiO4
11-0046 Kyanite Al2SiO5

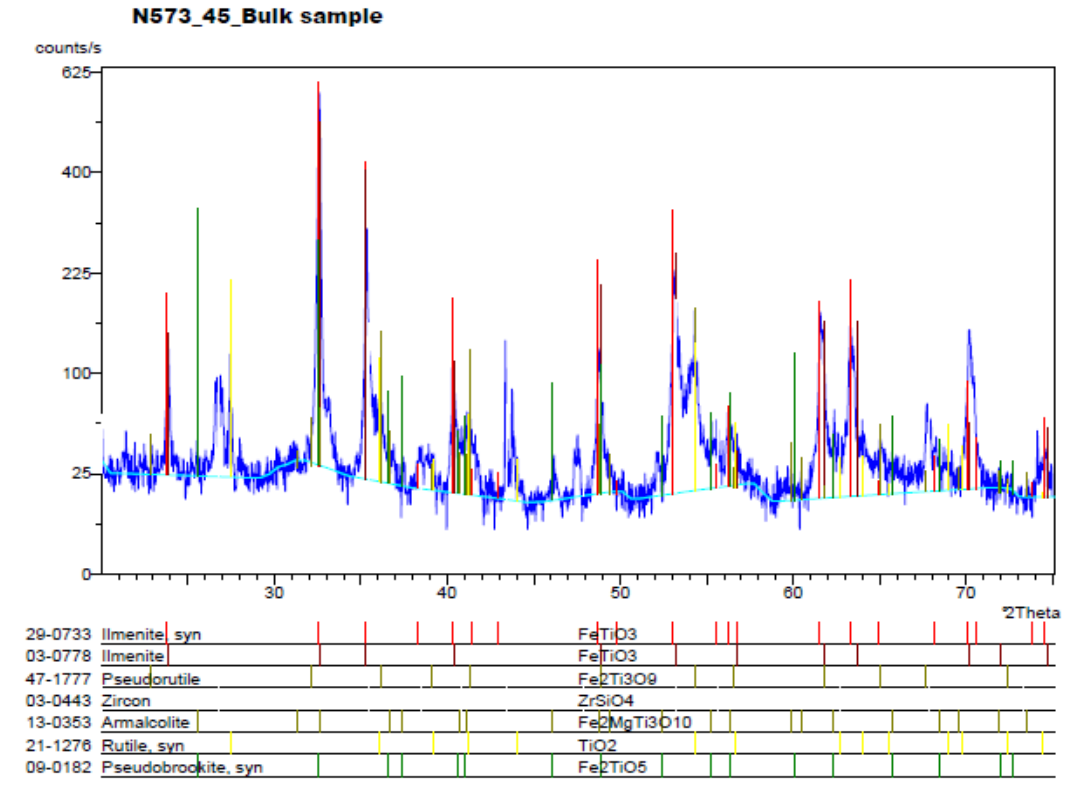
N573_45_Bulk sample
counts/s
625
400
225
100
25
0
30
40
50
60
70
°2Theta
29-0733 Ilmenite, syn FeTiO3
03-0778 Ilmenite FeTiO3
47-1777 Pseudorutile Fe2Ti3O9
03-0443 Zircon ZrSiO4
13-0353 Armalcolite Fe2MgTi3O10
21-1276 Rutile, syn TiO2
09-0182 Pseudobrookite, syn Fe2TiO5

Appendix D – Ilmenite grains single spot and transverse EMPA results.

Sample ID	NiO	Al2O3	TiO2	FeO	Cr2O3	MgO	MnO	Total
D130_35	0.01	0.03	52.43	45.69	0.01	0.22	0.81	99.19
D130_35	0.06	0.03	47.84	50.58	0.04	0.53	0.61	99.69
D141_07	-	0.25	42.58	39.34	0.03	0.20	14.22	96.63
D157_06	0.01	-	53.49	45.88	0.05	0.17	0.52	100.12
D157_32	-	0.15	55.98	35.33	0.10	0.16	3.79	95.51
D177_10	-	0.53	52.34	39.38	0.05	0.21	1.21	93.72
D177_10	0.01	0.13	55.86	33.95	-	0.04	4.02	94.01
D177_16	0.01	0.03	15.19	74.33	0.29	0.09	0.41	90.34
D201_21	0.04	0.31	55.64	31.45	0.27	0.01	5.48	93.21
D201_21	-	0.18	54.60	35.77	0.06	0.10	0.63	91.34
D303_18	0.03	0.10	55.66	35.12	-	0.11	2.82	93.84
D303_18	-	0.14	58.14	34.26	0.01	0.22	0.82	93.58
D303_18	-	0.19	56.42	35.07	0.30	0.16	1.62	93.76
D305_08	-	0.21	57.41	32.89	0.04	0.47	2.05	93.06
D305_15	0.01	0.01	51.90	39.14	0.02	0.32	7.48	98.88
N415_06	0.01	0.27	58.69	32.17	0.16	0.21	0.48	92.00
N415_11	0.01	1.52	56.70	29.19	0.10	0.85	2.72	91.10
N415_11	-	0.19	58.73	31.09	0.03	0.31	1.48	91.82
N439_66	-	-	49.25	44.65	-	0.05	1.34	95.29
N490_11	-	0.02	49.20	38.83	0.01	0.07	9.10	97.23
N490_36	-	0.02	89.43	0.25	0.02	0.01	0.06	89.78
N569_11	-	0.34	54.69	34.44	0.04	0.39	0.92	90.82
N569_49	-	0.09	51.62	38.76	-	0.09	1.51	92.07
N639_42	-	0.15	59.14	35.58	0.09	0.33	0.43	95.72
N639_42	-	0.00	50.97	50.65	0.03	0.25	1.19	103.09
N639_42	0.01	0.68	67.20	24.69	0.04	0.05	1.58	94.26
N672_15	-	0.41	52.08	35.97	-	1.08	0.40	89.94
N672_15	0.04	0.18	51.93	38.14	0.28	0.67	0.68	91.93
N672_15	-	0.41	52.08	35.97	-	1.08	0.40	89.94

No.	NiO	Al2O3	TiO2	FeO	Cr2O3	MgO	MnO	Total	Comment	BHID_Match
50	-	0.15	84.87	6.45	0.03	0.04	0.05	91.59	Mount-B_Pseudorutile3-spot1	
51	-	0.02	91.74	5.24	-	0.13	0.06	97.19	Mount-B_Pseudorutile3-spot2	
52	-	0.04	90.37	6.40	0.05	0.19	0.05	97.10	Mount-B_Pseudorutile3-spot3	D175_8
53	-	0.05	93.49	4.13	0.01	0.11	0.06	97.86	Mount-B_Pseudorutile3-spot4	
54	0.00	0.71	68.82	12.14	0.13	0.08	0.17	82.06	Mount-B_Pseudorutile3-spot5	
55	0.03	0.16	83.30	10.66	0.49	0.04	0.16	94.84	Mount-B_Pseudorutile20-spot1	
56	-	2.35	58.57	9.55	2.19	0.04	0.03	72.73	Mount-B_Pseudorutile20-spot2	
57	-	0.22	94.86	0.93	0.00	-	0.02	96.03	Mount-B_Pseudorutile20-spot3	D177_10
58	-	0.34	77.68	12.49	0.24	0.03	0.18	90.96	Mount-B_Pseudorutile20-spot4	
59	0.01	0.87	81.53	10.30	2.10	0.03	0.15	94.99	Mount-B_Pseudorutile20-spot5	
61	0.00	0.10	52.61	40.58	0.03	0.21	1.43	94.96	Mount_B_ilmenite23-spot1	
62	-	0.19	55.29	34.64	0.07	0.19	1.21	91.60	Mount_B_ilmenite23-spot2	
63	0.00	0.21	51.20	42.07	0.05	0.19	1.56	95.28	Mount_B_ilmenite23-spot3	D177_16
64	0.03	0.07	51.14	42.55	0.04	0.23	1.54	95.61	Mount_B_ilmenite23-spot4	
65	0.00	0.20	54.71	35.58	0.06	0.11	1.15	91.82	Mount_B_ilmenite23-spot5	
66	0.06	0.15	56.23	32.43	0.03	-	3.82	92.72	Mount_B_ilmenite24-spot1	
67	0.04	0.07	52.81	36.67	-	-	6.00	95.59	Mount_B_ilmenite24-spot2	
68	0.01	0.17	54.53	35.43	0.00	0.00	5.53	95.67	Mount_B_ilmenite24-spot3	
69	0.05	0.13	56.62	33.34	0.01	0.04	3.80	93.99	Mount_B_ilmenite24-spot4	D177_16
70	-	0.10	54.87	34.75	-	0.01	4.40	94.14	Mount_B_ilmenite24-spot5	
71	-	0.05	52.39	36.66	0.02	0.04	7.60	96.76	Mount_B_ilmenite24-spot6	
72	0.02	0.13	57.68	31.09	0.08	0.03	3.90	92.93	Mount_B_ilmenite24-spot7	
73	0.03	0.35	56.34	28.69	0.19	0.02	6.52	92.14	Mount_B_ilmenite34-spot1	
74	-	0.10	57.37	29.76	0.15	0.04	6.17	93.60	Mount_B_ilmenite34-spot2	
75	-	0.38	62.55	23.83	0.33	0.01	6.06	93.17	Mount_B_ilmenite34-spot3	
76	-	0.08	57.89	29.35	0.15	-	6.36	93.83	Mount_B_ilmenite34-spot4	
77	-	0.18	58.43	28.59	0.26	0.03	5.92	93.40	Mount_B_ilmenite34-spot5	
78	0.05	0.14	58.43	27.60	0.23	0.02	6.83	93.30	Mount_B_ilmenite34-spot6	D201_21
79	0.01	0.12	58.40	26.96	0.24	0.03	6.85	92.61	Mount_B_ilmenite34-spot7	
80	-	0.19	56.46	29.60	0.28	0.04	7.16	93.73	Mount_B_ilmenite34-spot8	
81	-	0.26	57.37	28.45	0.32	0.04	6.15	92.59	Mount_B_ilmenite34-spot9	
82	-	0.80	53.35	31.05	0.34	0.03	5.65	91.22	Mount_B_ilmenite34-spot10	
83	0.01	0.22	56.63	31.13	0.02	0.13	0.72	88.86	Mount_B_ilmenite35-spot1	
84	0.00	0.23	55.97	32.77	0.04	0.17	0.73	89.91	Mount_B_ilmenite35-spot2	
85	-	0.17	53.65	33.09	0.03	0.12	0.81	87.86	Mount_B_ilmenite35-spot3	
86	-	0.20	53.88	35.19	0.05	0.14	0.80	90.26	Mount_B_ilmenite35-spot4	D201_21
87	-	0.13	51.92	39.47	0.02	0.14	0.71	92.40	Mount_B_ilmenite35-spot5	
88	-	0.20	55.83	32.29	0.00	0.14	0.72	89.18	Mount_B_ilmenite35-spot6	
89	-	0.14	56.90	33.00	0.06	0.12	0.84	91.05	Mount_B_ilmenite35-spot7	
125	-	0.12	53.45	36.09	0.02	0.13	2.85	92.66	Mount_C_ilmenite10-spot1	
126	0.00	0.02	51.80	39.11	-	0.13	3.60	94.67	Mount_C_ilmenite10-spot2	
127	0.05	0.06	52.34	36.50	-	0.16	2.99	92.10	Mount_C_ilmenite10-spot3	
128	0.07	0.11	55.02	32.59	0.02	0.13	1.97	89.91	Mount_C_ilmenite10-spot4	D303_18
129	-	0.14	55.32	32.29	-	0.14	2.46	90.35	Mount_C_ilmenite10-spot5	
130	-	0.08	54.94	34.27	-	0.10	2.11	91.50	Mount_C_ilmenite10-spot6	
131	0.01	0.05	54.23	35.04	-	0.12	2.24	91.69	Mount_C_ilmenite10-spot7	
132	0.01	0.06	54.36	34.08	-	0.12	2.51	91.13	Mount_C_ilmenite10-spot8	
133	0.00	0.19	55.93	33.22	0.36	0.10	1.99	91.79	Mount_C_ilmenite12-spot1	
134	0.06	0.15	55.26	34.85	0.24	0.12	1.93	92.61	Mount_C_ilmenite12-spot2	
135	-	0.18	55.38	34.35	0.29	0.12	1.90	92.22	Mount_C_ilmenite12-spot3	
136	0.06	0.20	54.83	34.93	0.36	0.16	1.98	92.52	Mount_C_ilmenite12-spot4	D303_18
137	-	0.16	54.82	34.99	0.28	0.16	1.69	92.10	Mount_C_ilmenite12-spot5	
138	-	0.20	56.09	32.69	0.34	0.11	1.51	90.94	Mount_C_ilmenite12-spot6	
139	0.03	0.18	54.86	34.98	0.31	0.17	1.65	92.18	Mount_C_ilmenite12-spot7	
140	0.03	0.16	55.60	34.20	0.29	0.12	1.46	91.86	Mount_C_ilmenite12-spot8	

141	-	0.29	56.22	33.41	0.18	0.18	0.38	90.67	Mount_C_ilmenite28-spot1	N415_6
142	-	0.30	57.11	32.06	0.13	0.21	0.37	90.19	Mount_C_ilmenite28-spot2	
143	0.04	0.24	58.07	31.05	0.11	0.21	0.40	90.13	Mount_C_ilmenite28-spot3	
144	0.08	0.25	56.42	33.11	0.14	0.20	0.41	90.60	Mount_C_ilmenite28-spot4	
145	-	0.20	56.49	32.45	0.18	0.25	0.49	90.06	Mount_C_ilmenite28-spot5	
146	0.02	0.17	56.70	33.30	0.17	0.16	0.31	90.83	Mount_C_ilmenite28-spot6	
147	-	0.22	57.89	31.53	0.16	0.15	0.40	90.35	Mount_C_ilmenite28-spot7	
148	-	0.19	57.18	32.41	0.10	0.14	0.47	90.49	Mount_C_ilmenite28-spot8	
149	-	0.21	56.97	32.93	0.24	0.16	0.41	90.92	Mount_C_ilmenite28-spot9	
150	0.02	0.21	56.97	33.10	0.20	0.21	0.34	91.05	Mount_C_ilmenite28-spot10	
151	0.04	0.35	57.21	30.12	0.08	0.78	2.88	91.45	Mount_C_ilmenite35-spot1	N415_11
152	0.02	0.65	55.51	30.56	0.09	0.82	2.87	90.53	Mount_C_ilmenite35-spot2	
153	0.06	0.27	56.81	28.70	0.10	0.80	3.60	90.34	Mount_C_ilmenite35-spot3	
154	0.11	0.60	56.64	29.49	0.08	0.76	3.30	90.98	Mount_C_ilmenite35-spot4	
155	0.02	0.22	56.14	29.63	0.12	0.74	3.21	90.08	Mount_C_ilmenite35-spot5	
156	0.04	0.83	55.66	29.78	0.13	0.78	3.43	90.66	Mount_C_ilmenite35-spot6	
157	-	0.37	56.63	29.13	0.14	0.82	3.54	90.63	Mount_C_ilmenite35-spot7	
158	0.02	1.38	55.24	29.56	0.11	0.64	2.88	89.84	Mount_C_ilmenite35-spot8	
159	-	0.91	55.37	29.19	0.11	0.70	3.08	89.35	Mount_C_ilmenite35-spot9	
161	-	0.34	54.69	34.44	0.04	0.39	0.92	90.82	Mount_D_ilmenite4_spot1	N439_11
162	0.00	0.34	54.43	35.54	0.03	0.31	0.97	91.62	Mount_D_ilmenite4_spot2	
163	-	0.43	54.95	34.59	0.02	0.37	0.95	91.30	Mount_D_ilmenite4_spot3	
164	0.04	0.38	54.35	35.39	0.02	0.34	0.95	91.47	Mount_D_ilmenite4_spot4	
165	0.01	0.40	54.13	34.47	0.08	0.40	0.86	90.35	Mount_D_ilmenite4_spot5	
166	0.07	0.25	56.55	33.67	0.06	0.37	0.40	91.36	Mount_D_ilmenite4_spot6	
167	-	0.17	56.42	34.81	0.10	0.42	0.40	92.31	Mount_D_ilmenite5_spot1	N439_11
168	-	0.17	54.12	37.23	0.13	0.32	0.44	92.40	Mount_D_ilmenite5_spot2	
169	-	0.34	56.28	34.19	0.05	0.36	0.49	91.71	Mount_D_ilmenite5_spot3	
170	-	0.25	56.45	34.38	0.10	0.33	0.42	91.93	Mount_D_ilmenite5_spot4	
171	-	0.81	40.42	25.41	0.03	0.22	0.31	67.20	Mount_D_ilmenite5_spot5	
181	-	0.09	51.62	38.76	-	0.09	1.51	92.07	Mount_D_ilmenite12_spot1	N439_66
182	-	0.04	50.33	43.69	0.01	0.02	1.36	95.44	Mount_D_ilmenite12_spot2	
183	0.03	0.28	52.67	37.46	0.05	0.03	1.27	91.80	Mount_D_ilmenite12_spot3	
184	0.02	0.11	52.08	38.97	-	0.07	1.57	92.83	Mount_D_ilmenite12_spot4	
185	-	0.31	53.17	37.93	0.07	0.02	0.75	92.24	Mount_D_ilmenite12_spot5	
196	-	0.02	49.20	38.83	0.01	0.07	9.10	97.23	Mount_D_ilmenite23_spot1	N490_36
197	-	0.13	53.42	35.62	0.02	0.08	3.95	93.22	Mount_D_ilmenite23_spot2	
198	-	0.01	48.72	39.52	-	0.11	9.28	97.64	Mount_D_ilmenite23_spot3	
199	-	0.01	48.54	40.53	0.02	0.08	7.89	97.06	Mount_D_ilmenite23_spot4	
223	0.07	0.78	55.98	36.01	0.00	0.42	1.81	95.06	Mount_E_ilmenite8_spot1	N573_11
224	-	1.37	57.13	35.41	0.03	0.40	1.91	96.25	Mount_E_ilmenite8_spot2	
225	-	1.00	55.98	36.99	0.04	0.43	1.77	96.21	Mount_E_ilmenite8_spot3	
226	-	0.29	54.34	40.79	0.04	0.39	2.25	98.10	Mount_E_ilmenite8_spot4	
254	-	0.22	59.56	34.90	0.10	0.34	0.48	95.60	Mount_E_ilmenite39_spot1	N639_12
255	-	0.25	59.42	34.70	0.08	0.28	0.44	95.16	Mount_E_ilmenite39_spot2	
256	-	0.23	59.82	34.70	0.10	0.28	0.40	95.53	Mount_E_ilmenite39_spot3	
257	0.01	0.18	60.12	34.17	0.12	0.25	0.39	95.23	Mount_E_ilmenite39_spot4	
258	-	1.69	61.26	29.75	0.08	0.09	0.31	93.19	Mount_E_ilmenite39_spot5	
262	0.01	0.68	67.20	24.69	0.04	0.05	1.58	94.26	Mount_E_ilmenite45_spot1	N639_42
263	0.01	1.16	55.72	33.11	-	0.03	2.53	92.56	Mount_E_ilmenite45_spot2	
264	-	0.52	63.50	29.48	0.02	0.01	2.58	96.11	Mount_E_ilmenite45_spot3	
265	-	1.01	55.08	31.65	0.02	0.06	3.07	90.90	Mount_E_ilmenite45_spot4	

Appendix E – zircon U-Pb geochronology

					RATIOS							AGES [Ma]						Conc.
Sample	**Analysis**	**U [ppm][a]**	**Pb [ppm][a]**	**Th/U[a]**	**$^{207}Pb/^{235}U$[b]**	**2 s[d]**	**$^{206}Pb/^{238}U$[b]**	**2 s[d]**	**rho[c]**	**$^{207}Pb/^{206}Pb$[e]**	**2 s[d]**	**$^{207}Pb/^{235}U$**	**2 s**	**$^{206}Pb/^{238}U$**	**2 s**	**$^{207}Pb/^{206}Pb$**	**2 s**	%
SE#1-1a	SE1-1-1	604	108	0.38	1.878	0.060	0.1793	0.0038	0.67	0.0760	0.0018	1073	34	1063	23	1094	47	97
SE#1-1a	1	681	125	0.31	1.918	0.057	0.1843	0.0039	0.71	0.0755	0.0016	1087	32	1090	23	1081	42	101
SE#1-1a	2	1090	161	0.19	1.403	0.043	0.1475	0.0031	0.69	0.0690	0.0015	890	27	887	19	898	46	99
SE#1-1a	3	616	92	0.49	1.536	0.046	0.1490	0.0031	0.71	0.0748	0.0016	945	28	895	19	1063	42	84
SE#1-1a	4	1651	293	0.25	1.822	0.054	0.1775	0.0037	0.71	0.0744	0.0015	1053	31	1053	22	1053	42	100
SE#1-1a	5	941	116	0.38	1.259	0.038	0.1237	0.0026	0.70	0.0738	0.0016	828	25	752	16	1036	44	73
SE#1-1a	6	944	119	0.34	1.180	0.036	0.1262	0.0027	0.70	0.0678	0.0015	791	24	766	16	862	45	89
SE#1-1a	7	1029	167	0.34	1.618	0.048	0.1622	0.0034	0.71	0.0724	0.0015	977	29	969	20	996	42	97
SE#1-1a	8	313	29	0.39	0.848	0.027	0.0933	0.0020	0.68	0.0659	0.0015	623	20	575	12	804	48	71
SE#1-1a	9	184	22	0.12	1.104	0.035	0.1210	0.0026	0.67	0.0661	0.0016	755	24	737	16	810	49	91
SE#1-1a	10	751	73	0.35	1.059	0.032	0.0975	0.0021	0.70	0.0788	0.0017	733	22	599	13	1168	42	51
SE#1-1a	11	1198	124	0.29	0.976	0.030	0.1036	0.0022	0.70	0.0683	0.0015	691	21	636	13	878	45	72
SE#1-1a	12	1349	213	0.89	1.654	0.049	0.1577	0.0033	0.72	0.0761	0.0016	991	29	944	20	1097	41	86
SE#1-1a	13	832	109	0.68	1.349	0.041	0.1310	0.0028	0.70	0.0747	0.0016	867	26	793	17	1060	43	75
SE#1-1a	14	1018	153	0.04	1.471	0.044	0.1503	0.0032	0.70	0.0710	0.0015	919	28	903	19	957	44	94
SE#1-1a	15	339	45	0.06	1.430	0.045	0.1316	0.0028	0.68	0.0788	0.0018	901	28	797	17	1167	46	68
SE#1-1a	16	1727	174	0.61	1.224	0.043	0.1008	0.0022	0.62	0.0881	0.0025	812	29	619	14	1384	54	45
SE#1-1a	17	2062	206	0.20	0.982	0.029	0.0998	0.0021	0.71	0.0714	0.0015	695	21	613	13	968	43	63
SE#1-1a	18	837	111	0.25	1.286	0.039	0.1331	0.0028	0.70	0.0701	0.0015	840	25	806	17	931	44	87
SE#1-1a	19	1005	131	0.23	1.242	0.038	0.1306	0.0028	0.69	0.0690	0.0015	820	25	791	17	897	46	88
SE#1-1a	20	1581	263	0.17	1.687	0.052	0.1663	0.0035	0.69	0.0736	0.0016	1004	31	992	21	1029	45	96
SE#1-1a	21	1078	275	0.26	3.250	0.096	0.2554	0.0054	0.72	0.0923	0.0019	1469	43	1466	31	1473	39	100
SE#1-1a	22	1105	109	0.26	0.898	0.028	0.0987	0.0021	0.68	0.0661	0.0015	651	20	606	13	808	48	75
SE#1-1a	23	187	20	0.30	0.913	0.030	0.1072	0.0023	0.65	0.0618	0.0016	659	22	656	14	668	54	98
SE#1-1a	24	352	63	0.43	1.872	0.057	0.1801	0.0038	0.70	0.0754	0.0016	1071	33	1068	23	1079	44	99
SE#1-1a	25	2097	146	0.43	0.745	0.022	0.0695	0.0015	0.71	0.0778	0.0017	565	17	433	9	1141	42	38
SE#1-1a	26	512	77	0.59	1.619	0.066	0.1505	0.0034	0.56	0.0780	0.0026	978	40	904	20	1148	67	79
SE#1-1a	27	1676	280	0.44	1.681	0.050	0.1668	0.0036	0.71	0.0731	0.0015	1001	30	995	21	1016	43	98
SE#1-1a	28	1419	130	1.52	1.040	0.033	0.0918	0.0020	0.67	0.0821	0.0020	724	23	566	12	1248	47	45
SE#1-1a	29	409	69	0.66	1.854	0.064	0.1688	0.0037	0.64	0.0797	0.0021	1065	37	1005	22	1188	52	85
SE#1-1a	30	1945	382	0.27	2.112	0.063	0.1965	0.0042	0.72	0.0779	0.0016	1153	34	1156	25	1145	41	101
SE#1-1a	32	1042	180	0.14	1.782	0.055	0.1727	0.0037	0.69	0.0749	0.0017	1039	32	1027	22	1064	45	96
SE#1-1a	33	988	165	0.11	1.665	0.050	0.1667	0.0036	0.71	0.0724	0.0015	995	30	994	21	998	43	100
SE#1-1a	34	1563	135	0.15	1.092	0.040	0.0863	0.0019	0.61	0.0917	0.0026	749	27	534	12	1462	54	37
SE#1-1a	35	673	116	0.20	1.757	0.053	0.1724	0.0037	0.71	0.0739	0.0016	1030	31	1025	22	1039	43	99
SE#1-1a	36	364	62	0.25	1.795	0.055	0.1699	0.0037	0.70	0.0766	0.0017	1044	32	1012	22	1112	44	91
SE#1-1a	37	536	61	0.42	1.118	0.041	0.1130	0.0025	0.60	0.0718	0.0021	762	28	690	15	979	60	70
SE#1-1a	38	418	73	0.38	1.798	0.055	0.1749	0.0038	0.71	0.0745	0.0016	1045	32	1039	22	1056	43	98
SE#1-1a	39	993	137	0.33	1.359	0.042	0.1381	0.0030	0.70	0.0714	0.0016	872	27	834	18	969	45	86
SE#1-1a	40	1068	124	0.16	1.076	0.032	0.1157	0.0025	0.71	0.0675	0.0014	742	22	706	15	853	44	83
SE#1-1a	41	374	31	0.74	0.746	0.025	0.0843	0.0018	0.66	0.0642	0.0016	566	19	522	11	748	53	70
SE#1-1a	42	374	33	0.56	0.725	0.027	0.0870	0.0019	0.59	0.0605	0.0018	554	21	538	12	620	65	87
SE#1-1a	43	568	101	0.42	1.813	0.066	0.1774	0.0039	0.61	0.0741	0.0021	1050	38	1052	23	1045	58	101
SE#1-1a	44	1496	175	0.12	1.080	0.033	0.1167	0.0025	0.71	0.0672	0.0014	744	22	711	15	842	44	84
SE#1-1a	45	506	61	0.23	1.223	0.046	0.1207	0.0027	0.60	0.0735	0.0022	811	30	735	16	1028	61	71
SE#1-1a	46	4923	347	0.37	0.599	0.018	0.0706	0.0015	0.70	0.0616	0.0014	476	15	440	9	659	47	67

SE#1-1a	47	692	101	0.28		1.494	0.046	0.1461	0.0032	0.69	0.0742	0.0017		928	29	879	19	1046	45	84
SE#1-1a	48	1945	166	0.08		0.679	0.021	0.0852	0.0018	0.71	0.0578	0.0012		526	16	527	11	522	46	101
SE#1-1a	49	1228	192	0.24		1.542	0.049	0.1564	0.0034	0.69	0.0715	0.0016		947	30	937	20	971	47	96
SE#1-1a	50	1419	125	0.20		0.808	0.024	0.0881	0.0019	0.72	0.0665	0.0014		601	18	544	12	823	44	66
SE#1-1a	51	1202	96	0.97		0.871	0.027	0.0801	0.0017	0.69	0.0788	0.0018		636	20	497	11	1168	45	43
SE#1-1a	52	1534	141	0.36		0.811	0.025	0.0918	0.0020	0.71	0.0641	0.0014		603	18	566	12	744	46	76
SE#1-1a	53	1997	212	0.05		0.940	0.028	0.1060	0.0023	0.71	0.0643	0.0014		673	20	650	14	752	45	86
SE#1-1a	54	2206	232	0.14		1.063	0.032	0.1050	0.0023	0.72	0.0734	0.0015		735	22	644	14	1025	42	63
SE#1-1a	55	1874	179	0.05		0.910	0.027	0.0957	0.0021	0.72	0.0690	0.0014		657	20	589	13	899	43	66
SE#1-1a	56	174	30	0.31		1.742	0.055	0.1722	0.0038	0.69	0.0733	0.0017		1024	33	1024	22	1023	47	100
SE#1-1a	57	1777	172	0.16		0.937	0.031	0.0968	0.0021	0.67	0.0702	0.0017		671	22	596	13	933	50	64
SE#1-1a	58	1562	157	0.18		0.843	0.026	0.1006	0.0022	0.71	0.0608	0.0013		621	19	618	13	632	47	98
SE#1-1a	59	3200	280	0.12		0.702	0.021	0.0874	0.0019	0.72	0.0583	0.0012		540	16	540	12	540	46	100
SE#1-1a	60	2049	181	0.06		0.717	0.023	0.0884	0.0019	0.68	0.0588	0.0014		549	18	546	12	560	51	97
SE#1-1a	61	1555	153	0.32		0.933	0.028	0.0983	0.0021	0.72	0.0689	0.0015		669	20	604	13	895	44	68
SE#1-1a	62	1485	163	0.33		1.005	0.031	0.1096	0.0024	0.71	0.0665	0.0014		706	22	670	15	823	45	81
SE#1-1a	63	2958	272	0.15		0.742	0.023	0.0919	0.0020	0.72	0.0586	0.0012		563	17	567	12	551	46	103
SE#1-1a	64	1804	182	0.15		0.883	0.027	0.1011	0.0022	0.71	0.0634	0.0014		643	20	621	14	721	46	86
SE#1-1a	65	1273	171	0.36		1.301	0.040	0.1342	0.0029	0.71	0.0703	0.0015		846	26	812	18	938	44	87
SE#1-1a	66	2114	192	0.19		0.796	0.025	0.0907	0.0020	0.69	0.0637	0.0015		595	19	560	12	730	49	77
SE#1-1a	67	2062	213	0.35		0.996	0.031	0.1031	0.0022	0.71	0.0701	0.0015		702	22	633	14	931	45	68
SE#1-1a	68	1415	103	0.09		0.591	0.020	0.0726	0.0016	0.67	0.0591	0.0015		471	16	452	10	569	54	79
SE#1-1a	70	1019	160	0.18		1.545	0.047	0.1568	0.0034	0.72	0.0715	0.0015		948	29	939	20	971	43	97
SE#1-1a	71	1765	129	0.36		0.685	0.021	0.0730	0.0016	0.72	0.0681	0.0014		530	16	454	10	871	44	52
SE#1-1a	72	1021	146	0.04		1.438	0.045	0.1428	0.0031	0.69	0.0730	0.0017		905	29	860	19	1015	46	85
SE#1-1a	73	694	100	0.45		1.582	0.052	0.1447	0.0032	0.67	0.0793	0.0019		963	32	871	19	1179	48	74
SE#1-1a	74	706	122	0.11		1.760	0.054	0.1726	0.0038	0.72	0.0740	0.0016		1031	32	1026	22	1041	43	99
SE#1-1a	75	1086	178	0.40		1.657	0.051	0.1636	0.0036	0.72	0.0735	0.0016		992	30	977	21	1027	43	95
SE#1-1a	76	1054	180	0.32		1.720	0.052	0.1707	0.0037	0.72	0.0731	0.0015		1016	31	1016	22	1016	43	100
SE#1-1a	77	216	33	0.38		1.614	0.054	0.1533	0.0034	0.67	0.0764	0.0019		976	33	920	20	1104	50	83
SE#1-1a	78	1168	202	0.22		1.726	0.053	0.1733	0.0038	0.72	0.0722	0.0015		1018	31	1030	23	992	43	104
SE#1-1a	79	2338	199	0.10		0.675	0.021	0.0850	0.0019	0.72	0.0576	0.0012		524	16	526	12	515	47	102
SE#1-1a	80	2318	352	0.31		1.492	0.045	0.1521	0.0033	0.72	0.0712	0.0015		927	28	912	20	962	43	95
SE#1-1a	81	1536	155	0.12		0.907	0.028	0.1012	0.0022	0.72	0.0650	0.0014		655	20	621	14	774	45	80
SE#1-1a	82	1255	189	0.15		1.543	0.047	0.1506	0.0033	0.72	0.0743	0.0016		948	29	904	20	1050	43	86
SE#1-1a	83	135	13	0.77		0.759	0.031	0.0933	0.0021	0.56	0.0590	0.0020		574	23	575	13	569	73	101
SE#1-1a	84	153	18	0.23		1.073	0.036	0.1178	0.0026	0.65	0.0661	0.0017		740	25	718	16	810	54	89
SE#1-1a	85	224	39	0.26		1.798	0.059	0.1749	0.0039	0.68	0.0746	0.0018		1045	34	1039	23	1057	48	98
SE#1-1a	86	1024	127	0.43		1.241	0.038	0.1237	0.0027	0.72	0.0728	0.0016		819	25	752	17	1008	43	75
SE#1-1a	87	613	106	0.46		1.767	0.055	0.1737	0.0038	0.71	0.0738	0.0016		1033	32	1032	23	1036	44	100
SE#1-1a	88	1877	168	0.09		0.790	0.025	0.0895	0.0020	0.70	0.0640	0.0014		591	19	552	12	742	48	74
SE#1-1a	89	586	105	0.27		1.852	0.057	0.1789	0.0039	0.71	0.0751	0.0016		1064	33	1061	23	1070	43	99
SE#1-1a	90	1066	164	0.14		1.582	0.049	0.1542	0.0034	0.71	0.0744	0.0016		963	30	924	20	1053	44	88
SE#1-1a	91	858	157	0.27		1.914	0.059	0.1833	0.0040	0.71	0.0757	0.0016		1086	34	1085	24	1088	43	100
SE#1-1a	92	896	165	0.60		1.932	0.060	0.1844	0.0041	0.71	0.0760	0.0017		1092	34	1091	24	1096	44	100
SE#1-1a	93	727	71	0.83		1.004	0.032	0.0971	0.0022	0.70	0.0750	0.0017		706	22	597	13	1067	46	56
SE#1-1a	94	787	114	0.27		1.445	0.045	0.1444	0.0032	0.71	0.0726	0.0016		908	28	869	19	1002	44	87
SE#1-1a	95	1684	177	0.14		1.085	0.033	0.1053	0.0023	0.72	0.0747	0.0016		746	23	645	14	1061	43	61
SE#1-1a	96	950	152	0.92		1.614	0.051	0.1597	0.0035	0.70	0.0733	0.0017		975	31	955	21	1022	46	93
SE#1-1a	97	1408	242	0.02		1.730	0.054	0.1721	0.0038	0.71	0.0729	0.0016		1020	32	1024	23	1011	44	101
SE#1-1a	98	506	42	0.04		0.681	0.023	0.0828	0.0019	0.65	0.0597	0.0016		528	18	513	12	593	57	86

SE#1-1a	99	1233	108	0.21		0.737	0.024	0.0878	0.0020	0.68	0.0609	0.0015		561	19	543	12	634	52	86
SE#1-1a	100	1095	155	0.20		1.376	0.043	0.1416	0.0031	0.72	0.0705	0.0015		879	27	854	19	941	44	91
SE#1-1a	101	1948	229	0.26		1.114	0.034	0.1175	0.0026	0.72	0.0687	0.0015		760	23	716	16	891	44	80
SE#1-1a	102	274	60	2.25		2.575	0.093	0.2192	0.0050	0.63	0.0852	0.0024		1294	47	1278	29	1320	54	97
SE#1-1a	103	305	54	0.62		1.898	0.063	0.1768	0.0040	0.68	0.0778	0.0019		1080	36	1050	24	1143	49	92
SE#1-1a	104	779	96	0.90		1.269	0.042	0.1232	0.0028	0.68	0.0747	0.0018		832	27	749	17	1060	48	71
SE#1-1a	105	312	46	0.19		1.481	0.047	0.1480	0.0033	0.70	0.0726	0.0017		922	29	890	20	1002	46	89
SE#1-1a	106	168	17	0.30		0.819	0.029	0.0982	0.0022	0.65	0.0605	0.0016		608	21	604	14	622	57	97
SE#1-1a	107	3740	298	0.17		0.642	0.020	0.0798	0.0018	0.71	0.0584	0.0013		503	16	495	11	543	48	91
SE#1-1a	108	1630	138	0.08		0.678	0.023	0.0846	0.0019	0.67	0.0581	0.0015		525	18	524	12	532	55	98
SE#1-1a	109	105	14	0.18		1.316	0.046	0.1374	0.0031	0.65	0.0695	0.0018		853	30	830	19	913	55	91
SE#1-1a	110	1164	112	0.10		0.805	0.026	0.0958	0.0021	0.70	0.0609	0.0014		599	19	590	13	635	49	93
SE#1-1a	111	1774	313	0.10		1.800	0.056	0.1765	0.0039	0.72	0.0740	0.0016		1046	32	1048	23	1041	44	101
SE#1-1a	113	1875	144	0.17		0.634	0.020	0.0770	0.0017	0.70	0.0597	0.0014		499	16	478	11	593	50	81
SE#1-1a	114	2437	232	0.29		0.936	0.031	0.0951	0.0021	0.68	0.0713	0.0017		671	22	586	13	967	50	61
SE#1-1a	115	898	113	0.42		1.276	0.040	0.1261	0.0028	0.71	0.0734	0.0016		835	26	765	17	1025	45	75

						RATIOS								AGES [Ma]						Conc.
Sample	**Analysis**	**U [ppm][a]**	**Pb [ppm][a]**	**Th/U[a]**		**$^{207}Pb/^{235}U$[b]**	**2 s[d]**	**$^{206}Pb/^{238}U$[b]**	**2 s[d]**	**rho[c]**	**$^{207}Pb/^{206}Pb$[e]**	**2 s[d]**		**$^{207}Pb/^{235}U$**	**2 s**	**$^{206}Pb/^{238}U$**	**2 s**	**$^{207}Pb/^{206}Pb$**	**2 s**	%
SE#1-1b	SE1-1-1	78	12	0.40		1.590	0.057	0.1597	0.0036	0.63	0.0722	0.0020		966	35	955	22	992	57	96
SE#1-1b	116	187	27	0.19		1.452	0.047	0.1434	0.0032	0.69	0.0734	0.0017		911	29	864	19	1026	47	84
SE#1-1b	117	107	14	0.29		1.301	0.048	0.1298	0.0030	0.62	0.0727	0.0021		846	31	787	18	1006	59	78
SE#1-1b	118	152	26	0.42		1.740	0.063	0.1696	0.0039	0.63	0.0744	0.0021		1023	37	1010	23	1053	57	96
SE#1-1b	119	162	21	0.29		1.238	0.041	0.1309	0.0029	0.68	0.0686	0.0017		818	27	793	18	886	50	89
SE#1-1b	120	157	23	0.33		1.425	0.047	0.1466	0.0033	0.68	0.0705	0.0017		900	29	882	20	943	49	94
SE#1-1b	121	105	17	0.40		1.660	0.065	0.1590	0.0037	0.59	0.0757	0.0024		993	39	951	22	1088	63	87
SE#1-1b	122	226	32	0.23		1.446	0.046	0.1402	0.0031	0.70	0.0748	0.0017		908	29	846	19	1063	46	80
SE#1-1b	123	147	24	0.22		1.650	0.056	0.1667	0.0038	0.66	0.0718	0.0018		989	34	994	22	980	52	101
SE#1-1b	124	171	15	0.54		0.714	0.028	0.0886	0.0020	0.58	0.0584	0.0019		547	22	547	13	544	71	101
SE#1-1b	125	110	17	0.30		1.566	0.061	0.1516	0.0035	0.60	0.0749	0.0023		957	37	910	21	1066	63	85
SE#1-1b	126	233	24	0.37		0.866	0.029	0.1028	0.0023	0.67	0.0611	0.0015		634	21	631	14	643	53	98
SE#1-1b	127	135	14	0.30		0.850	0.043	0.1016	0.0025	0.48	0.0606	0.0027		624	31	624	15	626	95	100
SE#1-1b	128	114	15	0.44		1.189	0.041	0.1313	0.0030	0.66	0.0657	0.0017		795	27	795	18	796	54	100
SE#1-1b	129	253	26	0.10		0.876	0.031	0.1025	0.0023	0.63	0.0620	0.0017		639	23	629	14	674	59	93
SE#1-1b	130	106	11	0.25		0.831	0.030	0.0997	0.0023	0.62	0.0604	0.0017		614	22	613	14	619	61	99
SE#1-1b	131	66	11	0.52		1.746	0.063	0.1725	0.0039	0.64	0.0735	0.0020		1026	37	1026	23	1026	56	100
SE#1-1b	132	208	16	1.33		0.624	0.022	0.0793	0.0018	0.65	0.0570	0.0015		492	17	492	11	493	58	100
SE#1-1b	133	205	17	0.67		0.639	0.022	0.0809	0.0018	0.65	0.0573	0.0015		502	17	501	11	503	58	100
SE#1-1b	134	155	30	0.36		2.047	0.065	0.1920	0.0043	0.70	0.0773	0.0018		1131	36	1132	25	1129	45	100
SE#1-1b	135	157	31	0.34		2.077	0.066	0.1944	0.0044	0.70	0.0775	0.0018		1141	36	1145	26	1134	45	101
SE#1-1b	136	109	11	0.21		0.837	0.037	0.0995	0.0023	0.53	0.0610	0.0023		617	27	611	14	640	80	96
SE#1-1b	137	440	76	0.06		1.757	0.054	0.1725	0.0038	0.72	0.0739	0.0016		1030	32	1026	23	1038	43	99
SE#1-1b	138	137	27	0.52		2.108	0.073	0.1952	0.0044	0.66	0.0783	0.0020		1151	40	1149	26	1155	52	100
SE#1-1b	139	142	27	0.33		1.969	0.064	0.1869	0.0042	0.69	0.0764	0.0018		1105	36	1104	25	1106	47	100
SE#1-1b	140	112	19	0.45		1.731	0.058	0.1700	0.0038	0.68	0.0738	0.0018		1020	34	1012	23	1037	49	98

SE#1-1b	141	101	16	0.35		1.607	0.057	0.1619	0.0037	0.64	0.0720	0.0019		973	34	967	22	985	55	98
SE#1-1b	142	160	13	0.84		0.639	0.023	0.0808	0.0018	0.63	0.0574	0.0016		502	18	501	11	507	61	99
SE#1-1b	143	145	12	1.00		0.634	0.023	0.0805	0.0018	0.63	0.0571	0.0016		498	18	499	11	495	62	101
SE#1-1b	144	168	30	0.63		1.811	0.058	0.1760	0.0039	0.70	0.0746	0.0017		1050	34	1045	23	1059	46	99
SE#1-1b	145	315	39	0.86		1.104	0.035	0.1249	0.0028	0.71	0.0641	0.0014		755	24	759	17	745	47	102
SE#1-1b	146	100	12	0.44		1.070	0.039	0.1215	0.0028	0.63	0.0639	0.0018		739	27	739	17	738	60	100
SE#1-1b	147	98	17	0.39		1.791	0.060	0.1753	0.0040	0.67	0.0741	0.0018		1042	35	1041	24	1044	50	100
SE#1-1b	148	114	20	0.35		1.764	0.058	0.1740	0.0039	0.68	0.0735	0.0018		1032	34	1034	23	1029	49	101
SE#1-1b	149	327	30	0.62		0.732	0.024	0.0907	0.0020	0.69	0.0586	0.0014		558	18	560	13	551	52	102
SE#1-1b	150	161	16	0.57		0.831	0.037	0.0992	0.0023	0.53	0.0608	0.0023		614	27	610	14	632	81	96
SE#1-1b	151	71	12	0.83		1.759	0.062	0.1722	0.0039	0.65	0.0741	0.0020		1031	36	1024	23	1044	54	98
SE#1-1b	152	82	14	0.87		1.818	0.062	0.1765	0.0040	0.66	0.0747	0.0019		1052	36	1048	24	1062	52	99
SE#1-1b	153	64	11	0.42		1.738	0.061	0.1706	0.0039	0.64	0.0739	0.0020		1023	36	1015	23	1039	55	98
SE#1-1b	154	379	55	0.26		1.578	0.072	0.1455	0.0035	0.53	0.0787	0.0030		962	44	876	21	1164	76	75
SE#1-1b	155	258	44	0.47		1.855	0.060	0.1719	0.0039	0.69	0.0783	0.0018		1065	35	1023	23	1153	47	89
SE#1-1b	156	923	137	0.53		1.513	0.046	0.1483	0.0033	0.73	0.0740	0.0016		936	29	891	20	1041	43	86
SE#1-1b	157	160	21	0.76		1.216	0.041	0.1338	0.0030	0.68	0.0660	0.0016		808	27	809	18	805	51	101
SE#1-1b	158	98	10	0.37		0.820	0.033	0.0981	0.0023	0.57	0.0606	0.0020		608	25	603	14	626	72	96
SE#1-1b	159	269	27	0.14		0.830	0.031	0.0990	0.0023	0.61	0.0608	0.0018		614	23	609	14	632	64	96
SE#1-1b	160	74	9	0.14		1.153	0.055	0.1234	0.0030	0.51	0.0678	0.0028		778	37	750	18	861	85	87
SE#1-1b	161	14	1	0.37		0.710	0.054	0.0882	0.0024	0.36	0.0584	0.0041		545	41	545	15	545	155	100
SE#1-1b	162	225	42	0.33		1.937	0.062	0.1858	0.0042	0.70	0.0756	0.0017		1094	35	1099	25	1085	46	101
SE#1-1b	163	389	56	0.24		1.477	0.046	0.1441	0.0032	0.72	0.0743	0.0016		921	29	868	19	1050	44	83
SE#1-1b	164	94	13	0.53		1.368	0.083	0.1373	0.0036	0.43	0.0722	0.0040		875	53	829	22	993	111	84
SE#1-1b	165	103	18	0.49		1.723	0.058	0.1720	0.0039	0.68	0.0727	0.0018		1017	34	1023	23	1004	50	102
SE#1-1b	166	289	29	0.25		0.847	0.028	0.1012	0.0023	0.69	0.0607	0.0014		623	20	621	14	628	51	99
SE#1-1b	167	205	21	0.20		0.826	0.028	0.1001	0.0023	0.66	0.0599	0.0015		612	21	615	14	598	56	103
SE#1-1b	168	183	28	0.42		1.542	0.050	0.1520	0.0034	0.69	0.0736	0.0017		947	31	912	21	1030	47	89
SE#1-1b	169	139	17	0.41		1.117	0.038	0.1251	0.0028	0.66	0.0648	0.0017		761	26	760	17	767	54	99
SE#1-1b	170	160	20	0.33		1.157	0.043	0.1283	0.0029	0.61	0.0654	0.0019		780	29	778	18	787	62	99
SE#1-1b	171	252	45	0.73		1.854	0.058	0.1796	0.0040	0.71	0.0749	0.0017		1065	34	1065	24	1065	45	100
SE#1-1b	172	45	8	0.42		1.782	0.067	0.1756	0.0041	0.61	0.0736	0.0022		1039	39	1043	24	1031	60	101
SE#1-1b	173	130	23	0.38		1.797	0.059	0.1755	0.0040	0.69	0.0743	0.0018		1044	34	1042	24	1049	48	99
SE#1-1b	175	326	57	0.38		1.757	0.056	0.1733	0.0039	0.71	0.0735	0.0016		1030	33	1030	23	1029	45	100
SE#1-1b	176	160	19	0.45		1.104	0.037	0.1207	0.0027	0.67	0.0663	0.0016		755	25	735	17	816	52	90
SE#1-1b	177	96	16	0.54		1.717	0.061	0.1705	0.0039	0.65	0.0730	0.0020		1015	36	1015	23	1014	54	100
SE#1-1b	178	93	14	0.34		1.426	0.050	0.1461	0.0033	0.65	0.0708	0.0019		900	31	879	20	953	54	92
SE#1-1b	179	135	17	0.43		1.171	0.040	0.1232	0.0028	0.66	0.0689	0.0018		787	27	749	17	896	53	84
SE#1-1b	180	291	25	0.60		0.674	0.032	0.0845	0.0020	0.50	0.0578	0.0024		523	25	523	13	523	91	100
SE#1-1b	181	43	4	0.43		0.851	0.038	0.1010	0.0024	0.53	0.0611	0.0023		625	28	620	15	643	82	96
SE#1-1b	182	54	5	0.45		0.801	0.037	0.0968	0.0023	0.51	0.0600	0.0024		597	28	596	14	603	87	99
SE#1-1b	183	152	26	0.37		1.757	0.058	0.1716	0.0039	0.68	0.0743	0.0018		1030	34	1021	23	1049	49	97
SE#1-1b	184	204	35	0.29		1.768	0.057	0.1737	0.0039	0.70	0.0738	0.0017		1034	33	1032	23	1036	46	100
SE#1-1b	185	175	33	0.39		1.979	0.070	0.1861	0.0043	0.65	0.0771	0.0021		1108	39	1100	25	1124	54	98
SE#1-1b	186	291	50	0.53		1.773	0.056	0.1732	0.0039	0.71	0.0743	0.0017		1036	33	1030	23	1049	45	98
SE#1-1b	187	118	20	0.24		1.729	0.059	0.1712	0.0039	0.67	0.0732	0.0019		1019	35	1019	23	1020	51	100
SE#1-1b	188	123	23	0.32		1.999	0.067	0.1888	0.0043	0.68	0.0768	0.0019		1115	37	1115	25	1116	49	100
SE#1-1b	189	207	38	0.36		1.926	0.061	0.1852	0.0042	0.71	0.0754	0.0017		1090	35	1095	25	1080	45	101
SE#1-1b	190	205	26	0.83		1.208	0.040	0.1267	0.0029	0.69	0.0691	0.0016		804	26	769	17	903	49	85
SE#1-1b	191	186	34	1.07		1.886	0.061	0.1815	0.0041	0.70	0.0754	0.0018		1076	35	1075	24	1079	47	100
SE#1-1b	192	145	25	0.71		1.731	0.057	0.1724	0.0039	0.69	0.0728	0.0017		1020	34	1025	23	1009	48	102
SE#1-1b	193	293	30	0.05		0.878	0.031	0.1039	0.0024	0.65	0.0613	0.0016		640	22	637	14	648	57	98

SE#1-1b	194	35	6	0.36		1.730	0.072	0.1708	0.0040	0.57	0.0735	0.0025		1020	42	1016	24	1027	69	99
SE#1-1b	195	35	5	0.30		1.451	0.073	0.1482	0.0037	0.49	0.0710	0.0031		910	46	891	22	957	89	93
SE#1-1b	196	136	20	0.16		1.501	0.052	0.1489	0.0034	0.66	0.0732	0.0019		931	32	895	20	1018	53	88
SE#1-1b	197	150	22	0.14		1.465	0.049	0.1484	0.0034	0.68	0.0716	0.0017		916	30	892	20	975	50	92
SE#1-1b	198	97	17	0.47		1.834	0.063	0.1782	0.0041	0.67	0.0746	0.0019		1058	36	1057	24	1059	51	100
SE#1-1b	199	170	30	0.46		1.860	0.061	0.1794	0.0041	0.69	0.0752	0.0018		1067	35	1064	24	1074	48	99
SE#1-1b	200	85	9	0.48		0.831	0.037	0.1001	0.0024	0.53	0.0603	0.0023		614	27	615	15	613	82	100
SE#1-1b	201	75	7	0.37		0.723	0.031	0.0894	0.0021	0.54	0.0587	0.0021		552	24	552	13	555	80	99
SE#1-1b	202	81	8	0.26		0.785	0.031	0.0955	0.0022	0.59	0.0596	0.0019		588	23	588	14	589	68	100
SE#1-1b	203	132	12	0.38		0.736	0.027	0.0909	0.0021	0.62	0.0587	0.0017		560	21	561	13	555	62	101
SE#1-1b	204	38	7	0.38		1.719	0.072	0.1701	0.0040	0.56	0.0733	0.0025		1016	43	1013	24	1022	70	99
SE#1-1b	205	117	16	0.39		1.361	0.051	0.1381	0.0032	0.62	0.0715	0.0021		872	33	834	19	971	61	86
SE#1-1b	206	229	39	0.28		1.739	0.056	0.1719	0.0039	0.71	0.0734	0.0017		1023	33	1023	23	1024	46	100
SE#1-1b	208	213	39	0.94		1.923	0.062	0.1846	0.0042	0.70	0.0756	0.0017		1089	35	1092	25	1084	46	101
SE#1-1b	209	48	8	0.33		1.724	0.087	0.1704	0.0042	0.50	0.0734	0.0032		1017	51	1014	25	1024	88	99
SE#1-1b	210	158	27	0.40		1.713	0.057	0.1700	0.0038	0.68	0.0731	0.0018		1013	33	1012	23	1017	49	100
SE#1-1b	211	93	16	0.38		1.791	0.064	0.1736	0.0040	0.64	0.0748	0.0020		1042	37	1032	24	1063	55	97
SE#1-1b	212	158	30	0.40		2.018	0.067	0.1907	0.0043	0.69	0.0768	0.0018		1122	37	1125	25	1115	48	101
SE#1-1b	213	104	13	0.49		1.286	0.048	0.1276	0.0029	0.62	0.0731	0.0021		839	31	774	18	1017	59	76
SE#1-1b	214	82	13	0.36		1.559	0.054	0.1571	0.0036	0.65	0.0720	0.0019		954	33	941	21	985	54	95
SE#1-1b	215	150	26	0.33		1.810	0.060	0.1762	0.0040	0.69	0.0745	0.0018		1049	34	1046	24	1055	48	99
SE#1-1b	216	129	22	0.60		1.697	0.057	0.1687	0.0038	0.68	0.0730	0.0018		1008	34	1005	23	1013	50	99
SE#1-1b	217	38	7	0.39		1.742	0.067	0.1735	0.0040	0.60	0.0728	0.0022		1024	40	1031	24	1008	62	102
SE#1-1b	218	139	13	0.37		0.739	0.027	0.0914	0.0021	0.63	0.0587	0.0017		562	21	564	13	555	62	102
SE#1-1b	219	120	10	0.32		0.700	0.028	0.0870	0.0020	0.57	0.0584	0.0019		539	22	538	12	543	73	99
SE#1-1b	220	70	12	0.41		1.780	0.065	0.1745	0.0040	0.63	0.0740	0.0021		1038	38	1037	24	1041	58	100
SE#1-1b	221	86	14	0.37		1.687	0.064	0.1682	0.0039	0.61	0.0728	0.0022		1004	38	1002	23	1007	61	100
SE#1-1b	222	64	7	0.57		1.019	0.040	0.1170	0.0027	0.60	0.0632	0.0020		713	28	713	17	713	66	100
SE#1-1b	223	82	7	0.14		0.775	0.032	0.0903	0.0021	0.56	0.0622	0.0022		583	24	558	13	682	74	82
SE#1-1b	224	119	19	0.41		1.658	0.056	0.1625	0.0037	0.68	0.0740	0.0018		993	33	971	22	1042	50	93
SE#1-1b	225	142	25	0.35		1.780	0.059	0.1753	0.0040	0.68	0.0736	0.0018		1038	34	1041	24	1032	49	101
SE#1-1b	226	42	6	0.66		1.384	0.055	0.1441	0.0034	0.59	0.0696	0.0023		882	35	868	20	917	67	95
SE#1-1b	227	238	24	0.32		0.864	0.029	0.1020	0.0023	0.67	0.0615	0.0016		632	22	626	14	655	54	95
SE#1-1b	228	162	16	0.12		0.856	0.062	0.1004	0.0028	0.38	0.0619	0.0041		628	45	616	17	669	143	92

						RATIOS							AGES [Ma]						Conc.
Sample	**Analysis**	**U [ppm][a]**	**Pb [ppm][a]**	**Th/U[a]**		**$^{207}Pb/^{235}U$[b]**	**2 s[d]**	**$^{206}Pb/^{238}U$[b]**	**2 s[d]**	**rho[c]**	**$^{207}Pb/^{206}Pb$[e]**	**2 s[d]**	**$^{207}Pb/^{235}U$**	**2 s**	**$^{206}Pb/^{238}U$**	**2 s**	**$^{207}Pb/^{206}Pb$**	**2 s**	%
SE#1-1c	SE2-229-1	64	6	0.71		0.830	0.033	0.1003	0.0023	0.58	0.0600	0.0019	613	24	616	14	602	70	102
SE#1-1c	229	143	13	0.35		0.762	0.028	0.0932	0.0022	0.62	0.0593	0.0017	575	22	575	13	577	64	100
SE#1-1c	230	194	33	0.26		1.785	0.058	0.1720	0.0039	0.70	0.0753	0.0017	1040	34	1023	23	1076	46	95
SE#1-1c	231	171	22	0.52		1.160	0.039	0.1258	0.0029	0.68	0.0669	0.0016	782	26	764	17	834	50	92
SE#1-1c	232	83	14	0.38		1.775	0.061	0.1726	0.0040	0.67	0.0746	0.0019	1036	36	1026	24	1057	52	97
SE#1-1c	233	190	18	0.41		0.773	0.030	0.0944	0.0022	0.60	0.0594	0.0019	582	23	581	14	583	68	100
SE#1-1c	234	123	11	1.11		0.683	0.025	0.0854	0.0020	0.63	0.0580	0.0017	528	19	528	12	529	63	100
SE#1-1c	235	159	14	0.47		0.684	0.025	0.0854	0.0020	0.63	0.0581	0.0017	529	19	528	12	533	63	99

SE#1-1c	236	133	23	0.37	1.791	0.058	0.1753	0.0040	0.70	0.0741	0.0017	1042	34	1041	24	1044	47	100
SE#1-1c	237	221	37	0.42	1.752	0.056	0.1695	0.0038	0.70	0.0750	0.0017	1028	33	1009	23	1069	46	94
SE#1-1c	238	91	8	0.56	0.732	0.029	0.0903	0.0021	0.60	0.0588	0.0018	558	22	557	13	558	68	100
SE#1-1c	239	124	11	0.25	0.724	0.037	0.0903	0.0022	0.48	0.0581	0.0026	553	28	557	14	535	97	104
SE#1-1c	240	74	7	2.04	0.814	0.033	0.0982	0.0023	0.58	0.0601	0.0020	605	25	604	14	607	72	99
SE#1-1c	241	245	41	0.40	1.688	0.054	0.1684	0.0038	0.70	0.0727	0.0017	1004	32	1004	23	1005	46	100
SE#1-1c	242	155	15	0.24	0.777	0.028	0.0955	0.0022	0.63	0.0590	0.0017	584	21	588	14	567	61	104
SE#1-1c	243	211	20	0.15	0.768	0.027	0.0935	0.0021	0.64	0.0596	0.0016	579	21	576	13	588	59	98
SE#1-1c	244	224	20	0.18	0.724	0.025	0.0899	0.0021	0.68	0.0584	0.0015	553	19	555	13	544	55	102
SE#1-1c	245	214	19	0.16	0.720	0.025	0.0897	0.0020	0.67	0.0583	0.0015	551	19	554	13	540	56	103
SE#1-1c	246	122	21	0.33	1.752	0.058	0.1730	0.0040	0.69	0.0734	0.0018	1028	34	1029	24	1026	49	100
SE#1-1c	247	241	20	1.04	0.666	0.023	0.0831	0.0019	0.66	0.0582	0.0015	518	18	514	12	536	56	96
SE#1-1c	248	144	26	0.69	1.876	0.063	0.1809	0.0041	0.68	0.0752	0.0018	1073	36	1072	25	1074	49	100
SE#1-1c	249	336	61	0.55	1.872	0.059	0.1807	0.0041	0.72	0.0752	0.0016	1071	34	1071	24	1073	43	100
SE#1-1c	250	108	19	0.30	1.773	0.060	0.1754	0.0040	0.68	0.0733	0.0018	1036	35	1042	24	1023	50	102
SE#1-1c	251	257	27	0.20	0.910	0.030	0.1066	0.0024	0.68	0.0619	0.0015	657	22	653	15	671	52	97
SE#1-1c	252	462	82	0.27	1.838	0.057	0.1776	0.0040	0.73	0.0751	0.0016	1059	33	1054	24	1070	43	99
SE#1-1c	253	82	14	1.37	1.739	0.060	0.1712	0.0039	0.67	0.0737	0.0019	1023	35	1018	23	1034	52	99
SE#1-1c	254	65	11	1.16	1.791	0.069	0.1741	0.0041	0.61	0.0746	0.0023	1042	40	1035	24	1058	62	98
SE#1-1c	255	110	19	0.62	1.787	0.065	0.1746	0.0041	0.63	0.0742	0.0021	1041	38	1038	24	1047	57	99
SE#1-1c	256	22	2	0.31	0.801	0.051	0.0960	0.0025	0.42	0.0606	0.0035	598	38	591	16	624	124	95
SE#1-1c	257	23	2	0.33	0.792	0.046	0.0951	0.0024	0.44	0.0604	0.0031	592	34	586	15	618	112	95
SE#1-1c	258	103	10	0.13	0.814	0.031	0.0981	0.0023	0.61	0.0602	0.0018	605	23	603	14	611	65	99
SE#1-1c	259	1179	182	0.14	1.493	0.046	0.1547	0.0035	0.74	0.0700	0.0015	927	29	927	21	928	43	100
SE#1-1c	260	1537	147	0.05	0.784	0.024	0.0957	0.0022	0.73	0.0594	0.0012	588	18	589	13	581	45	101
SE#1-1c	261	7	1	0.18	0.926	0.077	0.0973	0.0029	0.36	0.0690	0.0053	665	55	598	18	900	160	66
SE#1-1c	262	54	5	0.52	0.705	0.031	0.0875	0.0021	0.54	0.0585	0.0022	542	24	541	13	548	82	99
SE#1-1c	263	40	4	0.42	0.701	0.044	0.0869	0.0023	0.42	0.0585	0.0033	539	34	537	14	547	124	98
SE#1-1c	264	111	10	0.28	0.760	0.029	0.0925	0.0022	0.61	0.0595	0.0018	574	22	571	13	587	66	97
SE#1-1c	265	146	14	0.64	0.759	0.028	0.0931	0.0022	0.63	0.0591	0.0017	573	21	574	13	571	63	101
SE#1-1c	266	98	17	0.41	1.691	0.058	0.1681	0.0039	0.67	0.0730	0.0018	1005	34	1002	23	1013	51	99
SE#1-1c	267	926	163	0.45	1.768	0.055	0.1756	0.0040	0.73	0.0730	0.0015	1034	32	1043	24	1014	43	103
SE#1-1c	268	159	16	0.32	0.828	0.030	0.1001	0.0023	0.64	0.0600	0.0017	612	22	615	14	602	60	102
SE#1-1c	269	80	10	0.70	1.171	0.050	0.1304	0.0031	0.56	0.0651	0.0023	787	33	790	19	779	74	101
SE#1-1c	270	86	12	0.28	1.403	0.050	0.1431	0.0033	0.65	0.0711	0.0019	890	31	862	20	960	55	90
SE#1-1c	271	162	13	0.66	0.622	0.022	0.0794	0.0018	0.64	0.0568	0.0016	491	18	493	11	484	61	102
SE#1-1c	272	291	23	0.84	0.637	0.021	0.0808	0.0018	0.68	0.0572	0.0014	500	17	501	11	498	54	100
SE#1-1c	273	138	12	0.64	0.685	0.025	0.0855	0.0020	0.63	0.0581	0.0017	530	19	529	12	533	63	99
SE#1-1c	274	57	5	0.81	0.775	0.035	0.0951	0.0023	0.52	0.0591	0.0023	583	27	585	14	572	85	102
SE#1-1c	275	62	6	0.78	0.813	0.033	0.0987	0.0023	0.58	0.0597	0.0020	604	24	607	14	593	71	102
SE#1-1c	276	63	6	0.75	0.793	0.032	0.0961	0.0023	0.58	0.0599	0.0020	593	24	591	14	599	72	99
SE#1-1c	277	114	15	0.49	1.150	0.040	0.1282	0.0030	0.66	0.0651	0.0017	777	27	778	18	776	56	100
SE#1-1c	278	93	9	0.69	0.748	0.028	0.0914	0.0021	0.61	0.0594	0.0018	567	21	564	13	582	65	97
SE#1-1c	280	196	34	0.58	1.794	0.058	0.1746	0.0040	0.70	0.0745	0.0017	1043	34	1037	24	1056	46	98
SE#1-1c	281	59	5	0.43	0.763	0.032	0.0907	0.0022	0.57	0.0610	0.0021	576	24	560	13	639	75	88
SE#1-1c	282	422	42	0.08	0.840	0.027	0.1004	0.0023	0.71	0.0607	0.0014	619	20	616	14	630	50	98
SE#1-1c	283	215	19	0.69	0.697	0.025	0.0868	0.0020	0.64	0.0583	0.0016	537	20	537	12	539	62	100
SE#1-1c	284	19	2	0.40	0.759	0.050	0.0934	0.0025	0.40	0.0590	0.0036	573	38	575	15	565	132	102
SE#1-1c	286	248	23	0.01	0.744	0.025	0.0910	0.0021	0.68	0.0593	0.0015	565	19	562	13	577	54	97
SE#1-1c	287	328	30	0.15	0.757	0.025	0.0925	0.0021	0.69	0.0594	0.0014	572	19	570	13	582	52	98
SE#1-1c	288	255	24	0.57	0.769	0.026	0.0941	0.0022	0.68	0.0593	0.0015	579	20	580	13	576	54	101
SE#1-1c	289	81	7	0.62	0.735	0.029	0.0876	0.0021	0.59	0.0608	0.0019	559	22	541	13	633	69	86
SE#1-1c	290	246	23	0.31	0.757	0.026	0.0926	0.0021	0.68	0.0593	0.0015	572	19	571	13	577	54	99
SE#1-1c	291	368	65	0.38	1.839	0.058	0.1775	0.0040	0.72	0.0752	0.0016	1059	33	1053	24	1073	44	98
SE#1-1c	292	141	14	0.29	0.824	0.029	0.0995	0.0023	0.65	0.0601	0.0016	610	22	611	14	607	58	101
SE#1-1c	293	32	3	0.43	0.670	0.037	0.0832	0.0021	0.46	0.0584	0.0029	520	29	515	13	543	107	95
SE#1-1c	294	83	7	0.69	0.710	0.029	0.0885	0.0021	0.58	0.0582	0.0019	545	22	547	13	535	72	102

SE#1-1c	295	85	8	0.22	0.728	0.035	0.0901	0.0022	0.51	0.0586	0.0024	555	26	556	14	552	89	101
SE#1-1c	296	121	11	0.69	0.727	0.027	0.0902	0.0021	0.63	0.0585	0.0017	555	21	556	13	547	64	102
SE#1-1c	297	21	2	0.58	0.958	0.051	0.1045	0.0026	0.48	0.0665	0.0031	682	36	640	16	822	97	78
SE#1-1c	298	909	158	0.27	1.749	0.055	0.1737	0.0040	0.73	0.0731	0.0016	1027	32	1032	24	1016	43	102
SE#1-1c	299	86	8	0.39	0.732	0.033	0.0903	0.0022	0.54	0.0588	0.0022	558	25	557	13	561	83	99
SE#1-1c	300	41	5	0.38	0.943	0.042	0.1096	0.0026	0.54	0.0624	0.0023	674	30	670	16	688	79	97
SE#1-1c	301	233	18	0.76	0.619	0.021	0.0790	0.0018	0.67	0.0568	0.0015	489	17	490	11	485	57	101
SE#1-1c	302	102	9	0.41	0.713	0.037	0.0861	0.0021	0.48	0.0601	0.0027	547	28	532	13	606	99	88
SE#1-1c	303	41	6	0.72	1.571	0.062	0.1544	0.0037	0.60	0.0738	0.0023	959	38	926	22	1036	64	89
SE#1-1c	304	33	3	0.32	0.805	0.042	0.0965	0.0024	0.48	0.0605	0.0028	599	32	594	15	622	100	96
SE#1-1c	305	32	3	0.33	0.804	0.044	0.0968	0.0024	0.46	0.0603	0.0029	599	33	595	15	614	105	97
SE#1-1c	306	228	22	0.57	0.770	0.026	0.0949	0.0022	0.68	0.0588	0.0015	580	20	584	13	561	54	104
SE#1-1c	307	25	4	0.50	1.539	0.068	0.1537	0.0037	0.55	0.0727	0.0027	946	42	921	22	1004	74	92
SE#1-1c	308	123	12	0.52	0.805	0.029	0.0974	0.0023	0.64	0.0600	0.0017	600	22	599	14	602	61	99
SE#1-1c	309	39	5	0.31	1.117	0.048	0.1221	0.0029	0.56	0.0664	0.0024	761	33	742	18	817	74	91
SE#1-1c	310	61	5	0.17	0.709	0.030	0.0882	0.0021	0.56	0.0583	0.0021	544	23	545	13	540	77	101
SE#1-1c	311	429	76	0.17	1.841	0.059	0.1781	0.0041	0.72	0.0750	0.0017	1060	34	1057	24	1068	44	99
SE#1-1c	312	20	2	0.21	0.764	0.045	0.0915	0.0024	0.44	0.0605	0.0032	576	34	565	15	623	115	91
SE#1-1c	313	770	72	0.10	0.762	0.025	0.0933	0.0021	0.71	0.0592	0.0014	575	19	575	13	574	50	100
SE#1-1c	314	37	3	0.15	0.782	0.037	0.0938	0.0023	0.52	0.0605	0.0024	587	28	578	14	620	87	93
SE#1-1c	315	102	9	0.27	0.697	0.034	0.0870	0.0021	0.51	0.0581	0.0024	537	26	537	13	535	91	100
SE#1-1c	316	94	16	0.61	1.713	0.059	0.1697	0.0039	0.67	0.0732	0.0019	1013	35	1011	23	1019	52	99
SE#1-1c	317	321	26	0.60	0.639	0.024	0.0808	0.0019	0.62	0.0573	0.0017	502	19	501	12	504	64	99
SE#1-1c	318	156	28	0.64	1.844	0.062	0.1783	0.0041	0.69	0.0750	0.0018	1061	36	1058	24	1069	49	99
SE#1-1c	319	268	22	1.18	0.651	0.022	0.0822	0.0019	0.67	0.0575	0.0015	509	17	509	12	510	56	100
SE#1-1c	320	64	5	0.42	0.679	0.029	0.0855	0.0020	0.55	0.0576	0.0021	526	23	529	13	514	79	103
SE#1-1c	321	238	24	0.05	0.839	0.028	0.1014	0.0023	0.68	0.0601	0.0015	619	21	622	14	605	53	103
SE#1-1c	322	44	4	0.27	0.741	0.034	0.0904	0.0022	0.53	0.0595	0.0023	563	26	558	14	586	85	95
SE#1-1c	323	80	7	0.51	0.747	0.030	0.0902	0.0021	0.59	0.0601	0.0019	567	23	557	13	607	70	92
SE#1-1c	324	235	22	0.43	0.757	0.026	0.0925	0.0021	0.68	0.0594	0.0015	572	19	570	13	580	54	98
SE#1-1c	325	122	12	0.31	0.825	0.030	0.0993	0.0023	0.64	0.0603	0.0017	611	22	611	14	613	61	100
SE#1-1c	326	263	27	0.20	0.850	0.029	0.1016	0.0023	0.68	0.0607	0.0015	625	21	623	14	630	53	99
SE#1-1c	327	80	8	0.41	0.829	0.033	0.0997	0.0024	0.60	0.0603	0.0019	613	24	613	15	614	68	100
SE#1-1c	328	75	13	0.36	1.753	0.095	0.1726	0.0045	0.48	0.0737	0.0035	1028	56	1026	27	1032	96	99
SE#1-1c	329	51	8	0.49	1.588	0.068	0.1558	0.0038	0.57	0.0739	0.0026	966	41	933	23	1040	72	90
SE#1-1c	331	38	4	0.54	0.816	0.039	0.0986	0.0024	0.51	0.0600	0.0025	606	29	606	15	604	89	100
SE#1-1c	332	359	29	0.66	0.644	0.022	0.0811	0.0019	0.69	0.0575	0.0014	505	17	503	12	512	53	98
SE#1-1c	333	89	7	0.38	0.674	0.028	0.0845	0.0020	0.57	0.0579	0.0020	523	22	523	12	525	74	100
SE#1-1c	334	47	4	0.48	0.728	0.033	0.0898	0.0022	0.53	0.0588	0.0023	555	25	554	13	559	84	99
SE#1-1c	335	158	23	0.45	1.539	0.065	0.1479	0.0036	0.57	0.0755	0.0026	946	40	889	22	1082	70	82
SE#1-1c	336	120	20	0.54	1.743	0.060	0.1711	0.0040	0.67	0.0739	0.0019	1024	35	1018	24	1038	51	98
SE#1-1c	337	39	3	0.56	0.720	0.035	0.0891	0.0022	0.51	0.0586	0.0024	551	26	550	13	552	90	100
SE#1-1c	338	55	5	0.46	0.733	0.038	0.0903	0.0023	0.48	0.0589	0.0027	558	29	557	14	564	100	99
SE#1-1c	340	362	31	0.20	0.707	0.024	0.0863	0.0020	0.69	0.0594	0.0014	543	18	533	12	583	53	91
SE#1-1c	341	83	15	0.48	1.873	0.065	0.1802	0.0042	0.67	0.0754	0.0020	1071	37	1068	25	1078	52	99
SE#1-1c	343	99	9	0.45	0.704	0.028	0.0880	0.0021	0.60	0.0580	0.0018	541	21	544	13	530	70	103
SE#1-1c	344	259	24	0.02	0.744	0.026	0.0920	0.0021	0.67	0.0586	0.0015	565	20	567	13	554	56	102
SE#1-1c	345	55	5	1.17	0.724	0.032	0.0905	0.0022	0.54	0.0581	0.0022	553	25	558	13	533	81	105

[a]U and Pb concentrations and Th/U ratios are calculated relative to GJ-1 reference zircon

[b]Corrected for background and within-run Pb/U fractionation and normalised to reference zircon GJ-1 (ID-TIMS values/measured value); $^{207}Pb/^{235}U$ calculated using $(^{207}Pb/^{206}Pb)/(^{238}U/^{206}Pb * 1/137.88)$

[c]Rho is the error correlation defined as the quotient of the propagated errors of the $^{206}Pb/^{238}U$ and the $^{207}/^{235}U$ ratio

[d]Quadratic addition of within-run errors (2 SD) and daily reproducibility of GJ-1 (2 SD)

[e]Corrected for mass-bias by normalising to GJ-1 reference zircon (~0.6 per atomic mass unit) and common Pb using the model Pb composition of Stacey & Kramers (1975)